



DEVELOPMENT OF AN AGGREGATION KERNEL FOR THE
ELECTROCOALESCENCE PROCESS

Ali Khajehesamedini

Tese de Doutorado apresentada ao Programa de Pós-graduação em Engenharia Química, COPPE, da Universidade Federal do Rio de Janeiro, como parte dos requisitos necessários à obtenção do título de Doutor em Engenharia Química.

Orientadores: José Carlos Costa da Silva Pinto
Frederico Wanderley Tavares
Marcio Nele de Souza

Rio de Janeiro
Agosto de 2019

DEVELOPMENT OF AN AGGREGATION KERNEL FOR THE
ELECTROCOALESCENCE PROCESS

Ali Khajehesamedini

TESE SUBMETIDA AO CORPO DOCENTE DO INSTITUTO ALBERTO LUIZ COIMBRA
DE PÓS-GRADUAÇÃO E PESQUISA DE ENGENHARIA (COPPE) DA
UNIVERSIDADE FEDERAL DO RIO DE JANEIRO COMO PARTE DOS REQUISITOS
NECESSÁRIOS PARA A OBTENÇÃO DO GRAU DE DOUTOR EM CIÊNCIAS EM
ENGENHARIA QUÍMICA.

Examinada por:

Prof. José Carlos Costa da Silva Pinto, D.Sc.

Prof. Frederico Wanderley Tavares, D.Sc.

Prof. Marcio Nele de Souza, D.Sc.

Prof. Argimiro Resende Secchi, D.Sc.

Prof. Papa Matar Ndiaye, D.Sc.

Prof. Fabio Pereira dos Santos, D.Sc.

Dra. Elizabeth Fonseca, D.Sc.

Prof. Eduardo Rocha de Almeida Lima, D.Sc.

RIO DE JANEIRO, RJ - BRASIL

AGOSTO DE 2019

Khajehesamedini, Ali

Development of an aggregation kernel for the electrocoalescence process/Ali Khajehesamedini. – Rio de Janeiro: UFRJ/COPPE, 2019.

XV, 148 p.: il.; 29,7 cm.

Orientadores: José Carlos Costa da Silva Pinto

Frederico Wanderley Tavares

Marcio Nele de Souza

Tese (doutorado) – UFRJ/ COPPE/ Programa de Engenharia Química, 2019.

Referências Bibliográficas: p. 137-148.

1. Fluidodinâmica Computacional. 2. Equação do Balanço Populacional. 3. Coalescência. 4. Captura. 5 Emulsão de A/O
I. Pinto, José Carlos Costa da Silva *et al.* II. Universidade Federal do Rio de Janeiro, COPPE, Programa de Engenharia Química. III. Título.

عقل کویدشش ہمت حدست و بیرون راه نیست

عشق کویدراہ ہمت و رفتہ ام من بارہا

*Reason says the world is limited in six directions there is no way out.
love says there is a way, and I have traveled it many times.*

Dedicated to my Mother, Father, and Sisters for their Unconditional Love & Support

ACKNOWLEDGMENTS

I would never have been able to finish my thesis alone. I owe my gratitude to all of the people who have made this journey possible; to the people whose names appear hereafter and to all those who are not mentioned in this acknowledgment.

First and foremost, I humbly offer my enduring gratitude to my Supervisors: Prof. José Carlos Costa da Silva Pinto (my Role Model), Prof. Marcio Nele de Souza (my Brazilian Father), and Prof. Frederico Wanderley Tavares whose expert guides and patient mentorship is exceptional and inspiring. I cannot thank them enough for giving me the privilege to work, learn, develop, and shape my career under their supervision.

My sincerest appreciation is to committee members for having accepted to assess my thesis and taking the time to read it through Prof. Argimiro Resende Secchi, Prof. Papa Matar Ndiaye, Prof. Fabio Pereira dos Santos, Dr. Elizabeth Fonseca, and Prof. Eduardo Rocha de Almeida Lima. It was a true honor for me to present my work to them. In addition, I am extremely grateful to Prof. Argimiro Resende Secchi (UFRJ), Prof. Paulo Laranjeiras Lage (UFRJ), Prof. Alberto Passalacqua (Iowa State University), Prof. Daniele Marchisio (Politecnico di Torino), Prof. Ville Alopaeus (Aalto University), Dr. Moshen Karimi (Chalmers University of Technology), Prof. Papa Matar Ndiaye (UFRJ), Prof. Fabio Pereira dos Santos (UFRJ), Dr. Hamid Tavassoli, and Prof. Payam Parvasi (Shiraz University of Technology) for their contributions in different stages of this work.

During my curriculum at UFRJ, I had the opportunity to meet wonderful people who have become inspiring friends. In particular, I would like to thank my colleagues Dr. Khalil Kashefi, Dr. Carlos Alberto Castor Jr, Dr. Troner Assenheimer de Souza, MSc. Débora Micheline Vaz de Miranda, and MSc. Barbara Esteves for their technical help that has enriched this work. Also, I extend my gratitude to my Labmates Dr. Thiago Marinho, Dr. Angela Duncke, Dr. Rafael Charin, Dr. Gizele Batalha, Dr. Alessandro Barros, Dr. Carla Napoli Barbato, Dr. Monique Lombardo, MSc. Siller Honse, MSc. Fernando Henrique, Msc. Andre Clemente de Farias, MSc. Isabella Fernandes, MSc. Máisa Pabis, Larissa Almeida, Thamyres Leocadio Vilela, Dr. Gustavo Alonso Barrientos, MSc. Natasha Kelber, Paula Barbosa for all their moral support and friendship during the course of this work.

I also would like to offer my gratitude to friends I made in the marvelous city of Rio de Janeiro. First but not least, I would like to thank Alice Liliane for her wonderful Friendship. Moreover, I am truly thankful to Dr. Farhad Zare & Dr. Sara Sayyadi for their unconditional hospitality. Additionally, I express my gratitude to Dr. Mojtaba Armandei, Dr. Mojtaba MoaliAmiri, Dr. Mahyar Fazeli, Dr. Mohsen Alaian, Dr. Mohammad Amini, Dr.

Masoud GhanbariKashani, MSc. Pauline Bourgeat, Dr. Felipe Gomide, and Daniel Rangel.

This research was funded by the premier four-year fellowship from the Federal University of Rio de Janeiro (CNPQ/CAPES), and financial support from Sinochem (China) and Statoil (Norway) companies. I would like to thank each and every one of these institutions for their significant contribution towards enriching this project.

My final and cordial gratitude and utmost respect are to my parents and my two wonderful sisters. They have been absolutely supportive and encouraging throughout my life and career. Words are just ineffable to express my indebtedness to them.

Resumo da Tese apresentada à COPPE/UFRJ como parte dos requisitos necessários para a obtenção do grau de Doutor em Ciências (D.Sc.)

DESENVOLVIMENTO DE UM KERNEL DE AGREGAÇÃO PARA O PROCESSO DE ELECTROCOALESCÊNCIA

Ali Khajehesamedini

Agosto/2019

Orientadores: José Carlos Costa da Silva Pinto

Frederico Wanderley Tavares

Marcio Nele de Souza

Programa: Engenharia Química

A água é normalmente coproduzida juntamente com o óleo em reservatórios de petróleo. Durante a produção de petróleo bruto, a mistura é submetida a intensa turbulência, proporcionando dispersão suficiente para a formação de emulsões água-em-óleo (A/O). A presença de emulsão A/O causa problemas práticos nos equipamentos industrial. A eletrocoalescência é aceita como o principal processo industrial para quebrar as emulsões A/O e separar as fases aquosa e oleosa. A aplicação de um campo elétrico alto às emulsões A/O polariza as gotas de água e aumenta a taxa da coalescência. A fim de melhorar o entendimento sobre os processos de dessalinização/ desidratação e selecionar os melhores parâmetros operacionais e estratégias de controle do processo, foram feitas tentativas para modelar este processo. Neste trabalho, o acoplamento de fluidinâmica computacional (CFD) e equação de balanço populacional (PBE) é usado como a ideia principal para conduzir a modelagem. Além disso, um novo conceito chamado “fase livre” é introduzido para modelar a criação da fase de água segregada (captura). Na primeira etapa do estudo, um modelo matemático baseado nas equações de balanço de massa, momento e populacional para as fases dispersa, oleosa e livre é desenvolvido para interpretar o processo de eletrocoalescência em batelada. Os parâmetros dos núcleos de agregação e captura são estimados usando os dados experimentais. Na segunda etapa do estudo, a planta piloto de eletrocoalescência contínua é simulada pela implementação dos núcleos derivados no software Ansys Fluent (R). Os resultados mostram um desempenho bom dos modelos em prever a separação das fases dentro dos vasos electrostáticos descontínuos e contínuos.

Abstract of Thesis presented to COPPE/UFRJ as a partial fulfillment of the requirements for the degree of Doctor of Science (D.Sc.)

DEVELOPMENT OF AN AGGREGATION KERNEL FOR THE
ELECTROCOALESCENCE PROCESS

Ali Khajehesamedini

August/2019

Advisors: José Carlos Costa da Silva Pinto

Frederico Wanderley Tavares

Marcio Nele de Souza

Department: Chemical Engineering

Water is normally coproduced along with oil in petroleum reservoirs. During the production of crude oil, the mixture is subjected to intense turbulence, providing sufficient dispersion for the formation of water-in-oil (W/O) emulsions. The presence of W/O emulsion causes practical problems in the industrial equipment. Electrocoalescence is accepted as the principal industrial process to break the W/O emulsions and separate the aqueous and oil phases. The application of a high electric field to the W/O emulsions polarizes the water droplets and enhances the rate of their coalescence. In order to improve the understanding of desalting/dehydration processes and to select the best operational parameters and control strategies of the process, attempts have been made to model this process. In this work, the coupling of computational fluid dynamics (CFD) and population balance equation (PBE) is used as the principal idea to conduct the modeling. Moreover, a new concept named “free phase” is introduced to model the creation of segregated water phase (capture). In the first stage of the study, a mathematical model based on population, mass and momentum balance equations for disperse, oil and free phase is developed to interpret the batch electrocoalescence process. The parameters of the aggregation and capture kernels are estimated using the experimental data. In the second stage of the study, the continuous electrocoalescence pilot plant is simulated by implementing the derived kernels in the Ansys Fluent (R) software. The results show a decent performance of the models in predicting the separation of the phases inside the batch and continuous electrostatic vessels.

Contents

| | |
|--|-----|
| List of Figures..... | xi |
| List of Tables..... | xiv |
| List of Symbols..... | xv |
| Chapter 1 - Introduction..... | 1 |
| 1.1. Description of a Typical Crude Oil Desalination Plant..... | 4 |
| 1.2. Principles of Electrostatic Desalination..... | 6 |
| 1.3. Electrostatic Technologies..... | 10 |
| 1.4. The Effect of Operating Conditions on Efficiency of Desalination Process..... | 13 |
| 1.4.1. Oil Properties..... | 13 |
| 1.4.2. Operating Temperature..... | 15 |
| 1.4.3. Electrostatic Voltages..... | 15 |
| 1.4.4. Electrostatic Frequency..... | 17 |
| 1.4.5. Type and Amount of Demulsifier..... | 18 |
| 1.4.6. Amount of Wash-Water..... | 18 |
| 1.5. Concluding Remarks..... | 19 |
| Nomenclature..... | 19 |
| Chapter 2 - Literature Review..... | 21 |
| 2.1. Interface Tracking..... | 22 |
| 2.2. Population Balance..... | 28 |
| 2.3. Overall Perspective of the Project (Problem, Importance, Objective, and Novelty) | 40 |
| Nomenclature..... | 42 |
| Chapter 3 – Methodology..... | 44 |
| 3.1. Description of Batch Experiments..... | 45 |
| 3.1.1. Basis of the Experiments..... | 46 |
| 3.1.2. Experimental Setup..... | 47 |
| 3.1.3. Experimental Procedure..... | 48 |
| 3.1.4. Experimental Conditions..... | 50 |
| 3.2. Mathematical Model for Batch Electrocoalescence Process..... | 52 |
| 3.2.1. Simplified Model for Experimental Analysis..... | 52 |
| 3.2.2. Coalescence and Capture Kernels..... | 57 |
| 3.2.3. Solution of the Mathematical Model..... | 58 |
| 3.2.4. Determination of the Initial DSD..... | 61 |
| 3.2.5. Estimation of Model Parameters..... | 62 |

| | |
|---|-----|
| 3.3. Description of Continuous Pilot Plant Experiments | 62 |
| 3.3.1. Pilot Plant..... | 63 |
| 3.3.2. Description of Pilot Plant Process | 63 |
| 3.3.3. Electrocoalescer Unit..... | 64 |
| 3.4. Mathematical model for Continuous Electrocoalescence Process..... | 67 |
| 3.4.1. Eulerian-QMOM Model of Ansys Fluent (R) software | 67 |
| 3.4.2. Simulation of the Continuous Electrostatic Vessel | 68 |
| Nomenclature..... | 74 |
| Chapter 4 - Results and Discussions..... | 77 |
| 4.1. Analysis of Batch Experiments and Model | 77 |
| 4.1.1. Analysis of the Stability of Emulsion..... | 77 |
| 4.1.2. Analysis of the Stability of Saline Emulsions..... | 79 |
| 4.1.3. Analysis of the Electrostatic and Sedimentation Experiments | 80 |
| 4.1.3.1. Effect of Electric field Intensity | 83 |
| 4.1.3.2. Effect of Initial Water Content | 83 |
| 4.1.3.3. Effect of Electrostatic Time | 84 |
| 4.1.4. Analysis of the Electrostatic and Turbiscan Experiments for saline emulsions | 84 |
| 4.1.5. Estimation of Batch Model Parameters | 87 |
| 4.1.6. Estimation of Batch Model Parameters for Saline Emulsions..... | 115 |
| 4.2. Evaluation of Continuous Pilot Plant Simulations..... | 117 |
| Nomenclature..... | 133 |
| Chapter 5 - Conclusions and Suggestions..... | 134 |
| 5.1. Conclusions..... | 134 |
| 5.2. Suggestions for Future Works | 135 |
| Bibliography..... | 137 |

List of Figures

| | |
|---|----|
| Figure 1-1: Mechanisms and factors influencing the coalescence efficiency of electrostatic separation of water-in-oil dispersions [4]..... | 2 |
| Figure 1-2: Schematic illustration of the crude oil desalting process [5] | 3 |
| Figure 1-3: Typical two-stage desalting process [5]..... | 5 |
| Figure 1-4: Electric forces between two conductive spheres [10]..... | 6 |
| Figure 1-5: Effective forces during droplet coalescence process [11]..... | 7 |
| Figure 1-6: Combined AC/DC Droplet Forces [6]..... | 10 |
| Figure 1-7: Conventional AC Dehydrator/Desalter [6] | 11 |
| Figure 1-8: Deep Field AC Dehydrator / Desalter [6] | 12 |
| Figure 1-9: Combined AC/DC Desalter [6] | 12 |
| Figure 1-10: Combined AC/DC Wiring [6] | 13 |
| Figure 1-11: Characteristic Oil / Water Density [17] | 14 |
| Figure 1-12: Threshold Voltage [17] | 16 |
| Figure 1-13: Applied Voltage vs. Oil Conductivity [17] | 17 |
| Figure 2-1: Different types of gas-liquid flow regime in a vertical pipe [95]..... | 35 |
| Figure 2-2: World conventional and unconventional liquid production (EIA, Drilling Info, Statistics Canada and Labyrinth Consulting Services, Inc.) | 41 |
| Figure 3-1: Schematic Diagram for the Methodology | 45 |
| Figure 3-2: Setup of the batch electrostatic system: (a) high voltage power source (b) electrodes and (c) batch vessel | 47 |
| Figure 3-3: Dimensions of the batch electrostatic vessel..... | 48 |
| Figure 3-4: Schematic sampling points of the (a) electrostatic vessel (b) Turbiscan's cuvette | 50 |
| Figure 3-5: Displacement of the vessel's height by removing the electrodes..... | 50 |
| Figure 3-6: Schematic of w/o emulsion combined with the sedimented water phase. ... | 52 |
| Figure 3-7: Schematic of the water phases present in the treater | 53 |
| Figure 3-8. Electrocoalescence pilot plant | 63 |
| Figure 3-9. Pilot Plant Process Flow Diagram | 64 |
| Figure 3-10. Electrocoalescer unit..... | 65 |
| Figure 3-11. Tempered borosilicate glass windows | 65 |
| Figure 3-12. Emulsion feeder | 66 |
| Figure 3-13. Electrodes of the electrostatic cell a) side view b) frontal view..... | 66 |

| | |
|--|-----|
| Figure 3-14: 3D geometry of the continuous electrostatic vessel | 69 |
| Figure 3-15: Axisymmetric dimensions of the continuous electrostatic vessel | 69 |
| Figure 3-16: 2D Axisymmetric mesh of the continuous electrostatic vessel..... | 70 |
| Figure 4-1: Turbiscan backscattering profile of the a) 15, b) 5 water% w/w model emulsions..... | 78 |
| Figure 4-2: Turbiscan backscattering profile of the a) 15, b) 5 water% w/w saline model emulsions..... | 80 |
| Figure 4-3: Microscopic images of the 1st experimental point: a) Initial sample, Turbiscan b-1) P1, c-1) P2, d-1) P3, Electrocoalescer b-2) P1, c-2) P2 d-2) P3 | 83 |
| Figure 4-4: Microscopic images of the 1st experimental point for saline emulsions: a) Initial sample, Turbiscan b-1) P1, c-1) P2, d-1) P3, Electrocoalescer b-2) P1, c-2) P2 d-2) P3 | 87 |
| Figure 4-5: 2D Profile of electric field inside the batch vessel ($V_0 = 6\text{kV}$)..... | 88 |
| Figure 4-6: 2D Profile of electric field inside the batch vessel for a) $V_0 = 4\text{kV}$ b) $V_0 = 8\text{kV}$ | 89 |
| Figure 4-7: Profile of BS&W for the central (fifth) experimental point at a) time = 105s, b) time = 210s, c) time = 315s, d) time = 420s..... | 95 |
| Figure 4-8: Profile of volume fraction of phases for the central (fifth) experimental point at a) time = 105s, b) time = 210s, c) time = 315s, d) time = 420s..... | 97 |
| Figure 4-9: Profile of velocity of phases for the central (fifth) experimental point at a) time = 105s, b) time = 210s, c) time = 315s, d) time = 420s | 100 |
| Figure 4-10: Profile of volume fraction of the droplets classes for the central (fifth) experimental point at a) time = 105s, b) time = 210s, c) time = 315s, d) time = 420s. | 102 |
| Figure 4-11: Profile of final diameter of the droplets classes for the central (fifth) experimental point at a) time = 105s, b) time = 210s, c) time = 315s, d) time = 420s. | 105 |
| Figure 4-12: Profile of d_{32} of the droplets classes for the central (fifth) experimental point at a) time = 105s, b) time = 210s, c) time = 315s, d) time = 420s..... | 107 |
| Figure 4-13: Profile of the final BS&W for the central point for pure aggregation, pure capture, and coalescence-capture cases | 109 |
| Figure 4-14: Profile of the final BS&W for the central point with initial $d_{\text{ave}} = 5.0023 \mu\text{m}$, $d_{\text{ave}} = 5.627 \mu\text{m}$, and $d_{\text{ave}} = 6.2517 \mu\text{m}$ | 110 |
| Figure 4-15: Profile of the final volume fraction of phases for the first experimental point | 111 |

| | |
|--|-----|
| Figure 4-16: Profile of the final volume fraction of the droplets classes for the first experimental point | 112 |
| Figure 4-17: Profile of the final diameter of the droplets classes for the first experimental point | 112 |
| Figure 4-18: Profile of the final volume fraction of phases for the third experimental point | 113 |
| Figure 4-19: Profile of the final volume fraction of the droplets classes for the third experimental point | 114 |
| Figure 4-20: Profile of the final diameter of the disperse phases for the third experimental point | 115 |
| Figure 4-21: Contour of DC electric field inside the vessel for $V_0=3\text{kV}$ (central experimental point in the work of Souza [169])..... | 118 |
| Figure 4-22: Examination of mesh convergence using the 3 rd simulation case (Timestep = 0.1s)..... | 120 |
| Figure 4-23: Contour of the d_{32} of the droplets for the 3 rd simulation case at a) time = 3.75min, b) time = 7.5min, c) time = 11.25min, d) time = 15min | 123 |
| Figure 4-24: Profile of area-weighted average of d_{32} of droplets for the 3 rd simulation case at the outlet of the vessel (Timestep = 0.1s)..... | 124 |
| Figure 4-25: Contour of free water volume fraction for the 3 rd simulation case at a) time = 3.75min, b) time = 7.5min, c) time = 11.25min, d) time = 15min | 127 |
| Figure 4-26: Contour of water volume fraction for the 3 rd simulation case at a) time = 3.75min, b) time = 7.5min, c) time = 11.25min, d) time = 15min | 130 |
| Figure 4-27: Profile of area-weighted average of water volume fraction for the 3 rd simulation case at the bottom of the vessel (Timestep = 0.1s)..... | 131 |
| Figure 4-28: Profile of area-weighted average of water volume fraction for the 3 rd simulation case at the outlet of the vessel (Timestep = 0.1s)..... | 132 |

List of Tables

| | |
|--|-----|
| Table 1-1: Typical desalination operating conditions according to the API degree of crude oil [9]..... | 4 |
| Table 2-1: Aggregation frequencies presented in the literature for water/oil coalescence. | 30 |
| Table 2-2: Selection of the multiphase model..... | 35 |
| Table 2-3: Settling velocities presented in the literature for water/oil coalescence. | 38 |
| Table 3-1: Characteristics of Exxsol D130 | 46 |
| Table 3-2: Experimental design..... | 51 |
| Table 3-3: Values of experimental variables..... | 51 |
| Table 3-4: Mesh properties used in the CFD-PBE simulations | 70 |
| Table 3-5: Settings of the CFD-PBE simulation in Ansys Fluent (R)..... | 72 |
| Table 3-6: List of user-defined functions (UDFs) | 74 |
| Table 4-1: Results of the electrostatic and Turbiscan tests | 81 |
| Table 4-2: Results of the electrostatic and Turbiscan tests for saline emulsions | 85 |
| Table 4-3: Values of estimates parameters | 90 |
| Table 4-4: Calculated and experimental values of BS&W | 92 |
| Table 4-5: Values of estimates parameters for saline emulsion | 116 |
| Table 4-6: Calculated and experimental values of BS&W for saline emulsion..... | 116 |
| Table 4-7: Cases of simulation | 119 |
| Table 4-8: Results of simulation cases..... | 120 |

List of Symbols

| | |
|-------|--|
| AC | Altering Current |
| CFD | Computational Fluid Dynamics |
| CQMOM | Conditional Quadrature Method of Moments |
| DC | Discrete Current |
| DQMOM | Direct Quadrature Method of Moments |
| DSD | Droplet Size Distribution |
| EQMOM | Extended Quadrature Method of Moments |
| PBE | Population Balance Equation |
| PBM | Population Balance Model |
| PDF | Particle Distribution Function |
| QMOM | Quadrature Method of Moments |

Chapter 1 - Introduction

Crude oil extracted from oil fields is always associated with some brine, forming a characteristic emulsion. The amount of water in crude oil depends on the distribution of phases within the reservoir, geographical location of an oil field (onshore or offshore), the lifespan of reservoir, extraction method and use of water for enhanced oil recovery. The water associated with crude oil contains minerals and salts that can cause many problems in refining processes [1].

Sodium chloride constitutes the main part of salts in crude oil. Calcium and magnesium chlorides are other salts present in crude oil. These salts are found in almost all waters co-produced with crude oil. Salts are rarely present in the organic phase of the crude oil, although they can be found in suspended and dissolved forms. In almost all cases, the salts, mostly chlorides, and sulfates are dissolved in suspended water droplets [2].

The amount of salt is usually linked to corrosion. When crude oil is distilled, chloride salts are decomposed to produce hydrochloric acid, which can cause strong corrosive effects. Other adverse effects are sedimentation and choking in exchangers, furnaces, pipes, and trays of the distillation column, as calcium and strontium carbonates and calcium and magnesium sulfates precipitate on heat exchange surfaces. Besides removing saltwater, another duty of desalination unit is to eliminate impurities such as sand, clay, iron oxide, iron sulfate and arsenic from crude oil, as some metals are present in organic compounds dissolved in water-in-oil (W/O) emulsion and can cause contamination and deactivation of catalysts used in refining processes [1].

Because of the many problems caused by the presence of salts, desalination is always performed in treating units up to 10-20 PTB¹ and in refineries up to 1-2 PTB, before sending the oil to the distillation unit. Basically, if the amount of minerals is higher than 10 PTB, then the crude oil must be desalinated. However, desalination is performed in many petroleum refineries even if the salt content is lower than this value, as salt deposits can cause fouling, corrosion in equipment and contamination of catalysts used in refining processes [3]. Electrocoalescence has been recognized as the most efficient technique to break W/O emulsion [4]. The most practical methods for demulsification and the mechanism and factors affecting the electrocoalescence process are shown in **Figure 1-1**.

¹ Pounds of salt per thousand barrels of crude oil

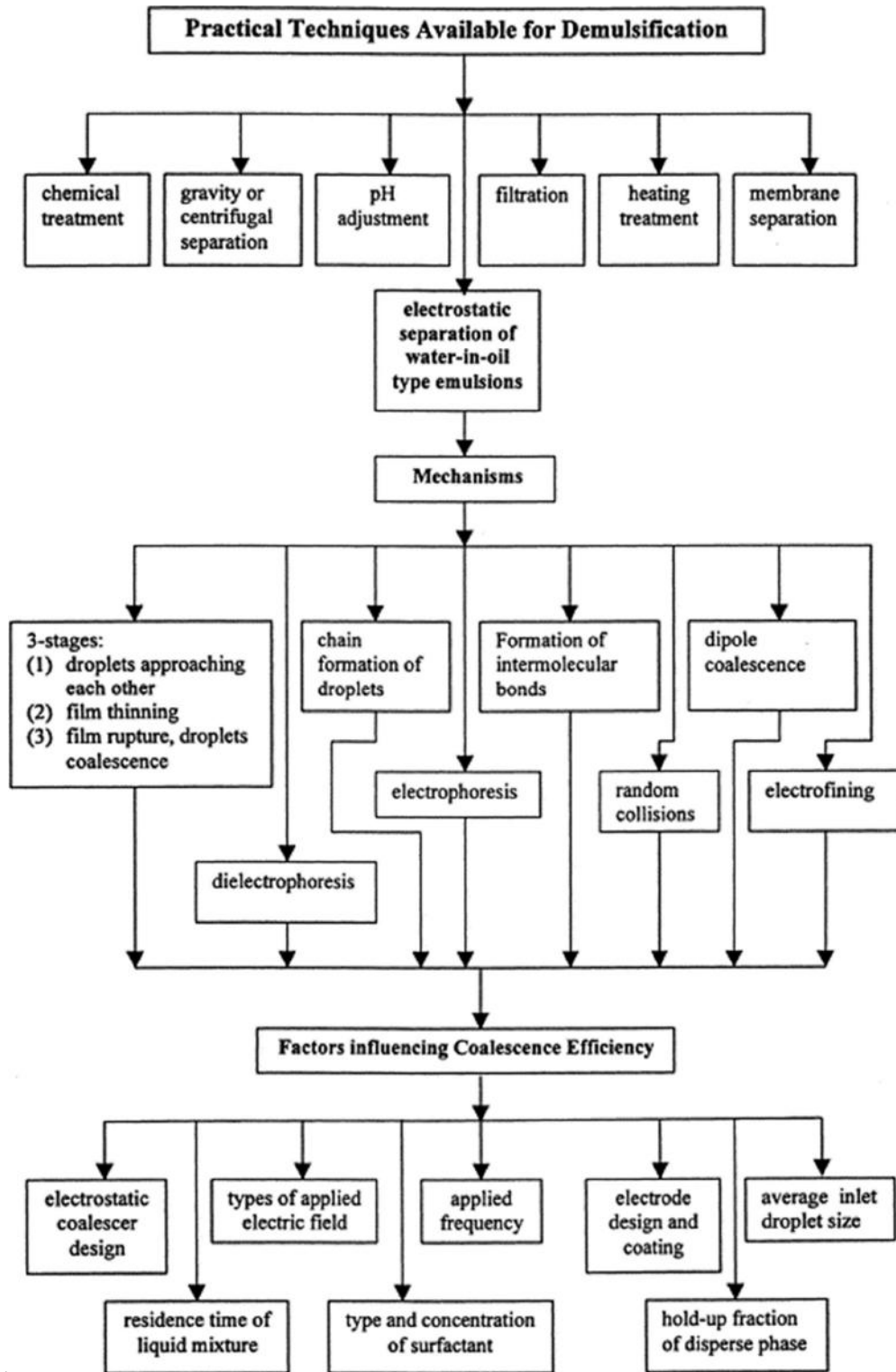


Figure 1-1: Mechanisms and factors influencing the coalescence efficiency of electrostatic separation of water-in-oil dispersions [4]

The basis of electrostatic desalination is the injection of washing water into crude oil in order to dissolve and dilute the minerals and the separation of water and oil in the desalter vessel by a strong electric field (Figure 1-2) [5]. Various factors, such as voltage and frequency of the electric field, density, and viscosity of the crude oil and the volume ratio of wash water, affect the efficiency of the desalination process. Besides, some materials can be deposited on water-oil interfaces such as asphaltene, resins, waxes, solid particles, clay or organic acids, and can act as emulsion stabilizers (emulsifiers). Therefore, the desalter must be able to break down these complex emulsions. As a consequence, the amount of desalination is dependent on the design of the desalter and on the operating conditions [6].

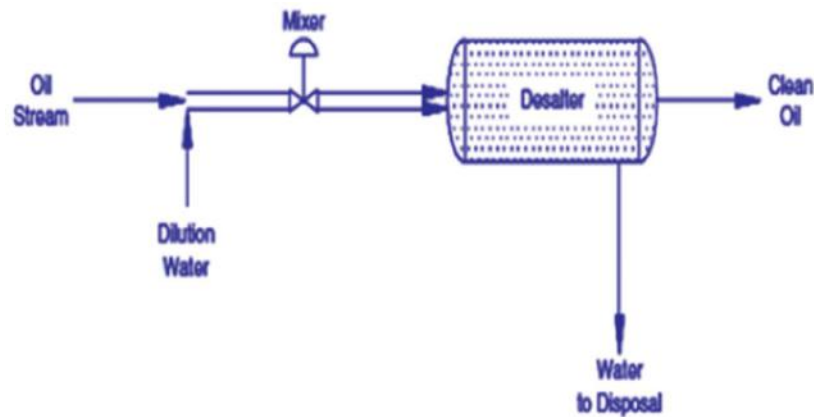


Figure 1-2: Schematic illustration of the crude oil desalting process [5]

In the desalting process, first, wash water is scattered out into crude oil in a special mixing valve that is able to form water droplets, reducing the salt concentration in the water. If wash water is not added, water droplets suspended in the crude oil will not have the chance to encounter and coalesce with each other. Then the W/O emulsion is directed into the desalination tank, where an electric field enhances the rate of separation of water and oil [7].

In the desalination tank, the W/O emulsion is placed under the effect of a high voltage electric field. The electric field breaks the oil layer around the water droplets, enhancing the rate of droplets coalescence and formation of larger water drops. Then larger drops fall down due to gravity (sedimentation), allowing for water/oil separation and removal of water and salts. Thus, gradually, the number of droplets reduces, also leading to an increase in the distance between the suspended droplets. This means that, no matter how

effectively desalination is conducted, there is a minimum limit below which water cannot be separated [8].

Several mechanisms have been proposed to explain the electrocoalescence process, although the most important is the three stages mechanism: (i) droplets approaching, (ii) film thinning/drainage and (iii) film rupture [4]. The use of the electric field on W/O emulsions initially causes polarization of conductive water droplets and strengthening of attraction forces among them. For droplets that are not too close, dipole-dipole forces are very small, so that this effect is negligible when the emulsion is in motion. For a pair of drops that are close to each other, the attraction forces can be strong and cause deformity of the surfaces, leading to coalescence. The main effective forces on moving droplets are gravity, buoyancy, drag, depletion and dipole forces [7].

1.1. Description of a Typical Crude Oil Desalination Plant

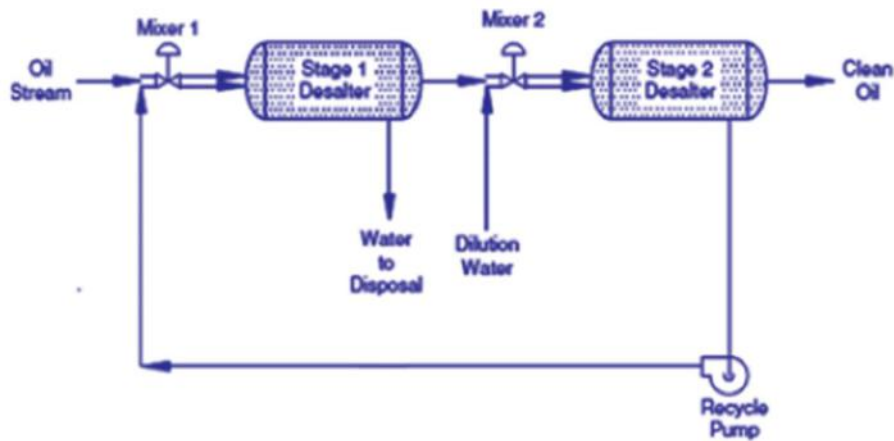
The desalting operation, depending on the characteristics of crude oil and the amount of allowed salt in output oil, is done by mixing crude oil with 3 to 10 percent of water (v/v %) at 60 to 150 °C. The ratio of water to oil and the operating temperature is a function of crude oil density. This mixture forms W/O emulsion that is separable by the electrostatic method. Heating is performed in order to decrease viscosity and surface tension, making the mixing of oil and wash-water easier. Heat reduces the viscosity of crude oil and produces an additional driving force for the collision of water droplets. In addition, lower viscosity speeds up the settling of water droplets within the desalter vessel. As shown in Table 1-1, the wash water content and the operating temperature depend on the density of the crude oil [9].

Table 1-1: Typical desalination operating conditions according to the API degree of crude oil [9]

| API degree | Water Content (v/v %) | Operating Temperature °C |
|---------------|-----------------------|--------------------------|
| 40 < API | 3 - 4 | 60 - 125 |
| 30 < API < 40 | 4 - 7 | 125 - 140 |
| API < 30 | 7 - 10 | 140 - 150 |

Salts are dissolved in the wash water and then water and oil are separated in the separator vessel. The separation is performed with the application of a high potential electric field, which accelerates the coalescence of water droplets. The electric potential difference

needed usually ranges from 18 to 24 kilovolts (kV). Alternating electric fields can be applied in the vicinities of the oil and water interfaces. This causes efficient separation of water droplets at lower temperatures, consequently leading to higher energy efficiencies. The desalinated crude oil and separated brine exit continuously from the upper and lower sides of the desalter vessel, respectively. Then a single-stage desalting unit requires a too high amount of wash water or dilution water, two-stage desalination systems, as shown in [Figure 1-3](#), can be used. In single-stage desalination units, the maximum efficiency of operation is close to 95%, while in two-stage units it can increase up to 99% [3].



[Figure 1-3](#): Typical two-stage desalting process [5]

In two-stage desalting units, water, and oil flow counter-currently through the desalters, as freshwater first enters the second stage and the effluent water goes to the first one, while crude oil is fed to the first stage and then goes to the second one. Before entering the first desalination vessel, crude oil is mixed in the first valve with the output wash water from the second stage, where solutes concentration is increased. The output oil from this stage, with partially reduced brine concentration, is mixed in the second valve with the dilution water, entering into the second stage of desalination to remove the residual saltwater. The output desalinated oil from the second stage, as the product, exits the upper side of the desalter; while the separated saltwater enters the first stage as the wash water. The waste produced from the second stage as the final effluent is directed to the treatment plants [5].

As the size of wash water droplets dispersed in crude oil decreases, the possibility of contact with the original saltwater droplets suspended in crude oil increases [1]. The

optimum pressure drop needed in the mixing valves to create the W/O emulsion must be determined empirically. Typically, the pressure drop ranges from 5 to 30psi [6].

Heavy crude oils with low API degrees create more stable emulsions, reducing the efficiency of desalination units. Moreover, crude oils with higher viscosities tend to create more stable emulsions, when compared to oils with lower viscosities. The emulsion of crude oils with high viscosities are usually very stable, making separation difficult, as the high viscosity hinders the movement of dispersed water droplets and consequently delays droplet coalescence. Besides, this type of crude oil contains higher amounts of emulsifiers, in comparison to lighter oils [6].

1.2. Principles of Electrostatic Desalination

If no force is exerted on drops of a liquid suspended in another liquid, droplets tend to be spherical. If a high voltage electric field is applied, the drops lose their characteristics spherical shape. Under the effect of the electric field, positive and negative charges are concentrated on different drop hemispheres, located in front of oppositely charged electrodes [10].

As shown in Figure 1-4, two adjacent polarized drops are subjected to the mutual electrical attraction. On the negative side of a drop, the positive side of another drop is located in the nearest distance. Therefore, there exists an attractive force between the two sides which tends to attract the drops to each other. If this force is sufficiently strong, the drops move and the outer layers of the drops (oil layer) is broken, allowing the droplets to coalesce and form a larger droplet.

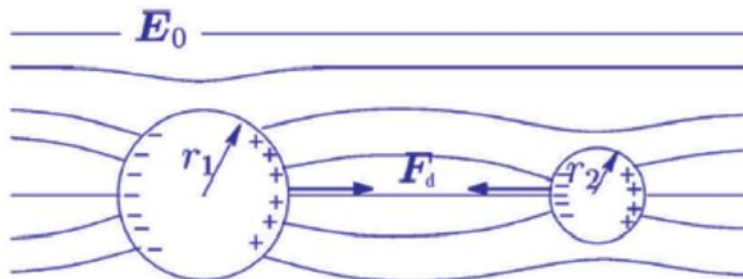


Figure 1-4: Electric forces between two conductive spheres [10]

A water droplet suspended between a pair of electrodes is acted upon by five forces, as indicated in Figure 1-5 [11]. Two of these five forces are the gravitational and hydraulic forces. Gravitational forces are related to the weight of the droplet and move the water droplet towards the bottom of the vessel. Drag forces imposed by the rising oil that flows through the water droplets tend to lift them towards the oil outlet.

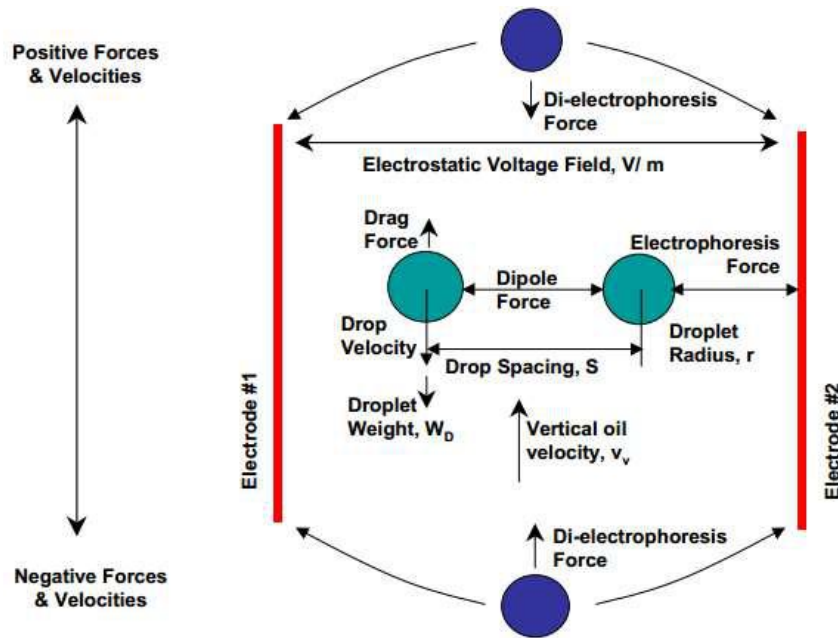


Figure 1-5: Effective forces during droplet coalescence process [11]

If the water droplet is larger than the Stokes droplet diameter, as calculated by the Equation (1-1), the weight is greater than the drag and the water droplet will be separated from the oil [6].

$$d_{Stokes} = \left(\frac{18\mu_c v_c}{g(\rho_d - \rho_c)} \right) \quad (1-1)$$

In order to maximize the desalting process performance, the electrostatic forces must be capable of promoting droplet coalescence to diameters greater than the Stokes diameter. The three electrostatic forces are the dipolar, electrophoretic and dielectrophoretic forces:

1) Dipole forces (F_{dip}) are established by the alignment of the polar water molecules in the droplet and are proportional to the electric field gradient, the water droplet diameter and the spacing between droplets, as shown in Equation (1-2) [12]:

$$\begin{aligned}
F_r &= -\frac{12\pi\beta^2\epsilon_c E^2 r_V^3 r_U^3}{s^4} (3K_1 \cos^2 \theta - 1) \\
F_\theta &= -\frac{12\pi\beta^2\epsilon_c r^2 E^2 r_V^3 r_U^3}{s^4} K_2 \sin(2\theta) \\
\beta &= \frac{\epsilon_d - \epsilon_c}{\epsilon_d + 2\epsilon_c}
\end{aligned} \tag{1-2}$$

Coefficients K_1 and K_2 can be expressed in the form:

$$\begin{aligned}
K_1 &= 1 + \frac{\beta r_V^3 s^5}{(s^2 - r_U^2)^4} + \frac{\beta r_U^3 s^5}{(s^2 - r_V^2)^4} + \frac{3\beta^2 r_V^3 r_U^3 (3s^2 - r_V^2 - r_U^2)}{(s^2 - r_V^2 - r_U^2)^4} \\
K_2 &= 1 + \frac{\beta r_V^3 s^3}{2(s^2 - r_U^2)^3} + \frac{\beta r_U^3 s^3}{2(s^2 - r_V^2)^3} + \frac{3\beta^2 r_V^3 r_U^3}{(s^2 - r_V^2 - r_U^2)^3}
\end{aligned} \tag{1-3}$$

This mathematical equation is called the Dipole-Induced-Dipole approximation (DID model). In this equation, s is the distance between the centers of droplets V and U, while r_V and r_U are the radiuses of the droplets, respectively. θ is the angle established between the direction of the electric field (E) and the axis that connects the centers of the droplets pair and finally ϵ_c and ϵ_d are the permittivities of oil and water. The radial force component (F_r) is attractive when the angle θ is lower than 54.78° [13,14] and repulsive when $55 < \theta < 125.38$. The tangential force component (F_θ) causes a torque that tends to align the axis that connects two centers of the drops with the applied electric field [14].

2) Electrophoretic forces are attractive and repulsive forces established in a uniform voltage field between charged droplets and the electrodes. They are proportional to the field strength, droplet diameter, and oil conductivity, as shown in Equation (1-4).

$$F_e = C\pi^3 \mu_c \epsilon_c r^2 E^2 e^{(-\sigma_c t / \epsilon_c)} \tag{1-4}$$

where C is a constant, while μ_c and σ_c are the viscosity and conductivity of the oil phase, respectively.

3) Di-electrophoretic forces are attractive forces established in a non-uniform field. These forces pull the droplet towards the highest voltage gradient and are proportional to the droplet diameter and the oil permittivity, as shown in Equation (1-5).

$$F_{diel} = 2\pi r^3 \varepsilon_c \left(\frac{\varepsilon_d^* - \varepsilon_c^*}{\varepsilon_d^* + 2\varepsilon_c^*} \right) \nabla E^2 \quad (1-5)$$

These three electrostatic forces are present in all desalters and can be manipulated to achieve enhanced coalescence and separation by altering the electrostatic voltage fields. As Equation (1-2) shows, the dipole force is dependent on the water droplet size and the spacing between them. Assuming that water droplets are uniformly sized and homogeneously distributed, it is easy to see that spacing is inversely proportional to the dispersed water volume, as shown in Equation (1-6). In this equation, s is the spacing between droplets and $BS\&W$ is the water content. Therefore, as the dispersed water is coalesced and separated from the oil, the spacing between droplets increases and the dipole forces decline rapidly. Equation (1-6) also shows that the spacing increases when the droplet radius increases. Therefore, the dipole force weakens rapidly as droplets are coalesced and separated from the oil.

$$s = r \left(\frac{1.333\pi}{BS\&W} \right)^{0.333} \quad (1-6)$$

As Equation (1-4) shows, the electrophoretic force is independent of the droplet spacing but is dependent on both the oil viscosity and conductivity. The electrophoretic force has a time constant that equals the ratio of the dielectric constant and conductivity of the oil. As Equation (1-4) shows, the electrophoretic force decays most rapidly in highly conductive oil. Therefore, the force can only be sustained by replenishing the droplet charge frequently.

As Equation (1-5) shows, the dielectrophoretic force is independent of the droplet spacing but is dependent on the change in field strength, which pulls the largest droplets into the highest field gradient. This force causes the accumulation of water in areas of the electrostatic field where its divergence is greatest.

Dipolar and di-electrophoretic forces are predominant in AC desalting processes. The drop-to-drop dipolar forces are greatest in the bottom of the desalter, where the water content is high and the droplets are closely spaced. The dielectrophoretic forces pull droplets to the rods used to construct the electrode arrays and thereby increase the droplet population and the dipolar forces. Since the electrical polarity on the AC electrodes reverses every few milliseconds, the electrophoretic force also reverses direction and exerts little influence on the coalescence process.

The uniform DC field established between the electrodes relies on the electrophoretic force to push and pull droplets in a horizontal plane between electrodes. Once a water droplet approaches one energized electrode, it is charged to the same polarity. Once the droplet is charged, the electrophoretic force then pushes the droplet towards the adjacent and oppositely charged electrode [15]. As the droplet approaches this electrode, the electrophoretic force pulls the droplet towards it until the droplet charge is reversed. Therefore, the electrophoretic forces provide a motive force to move the water droplet population in opposite directions between electrodes. The resulting collisions achieve efficient coalescence, large droplet sizes and rapid separation. These actions are shown schematically in Figure 1-6.

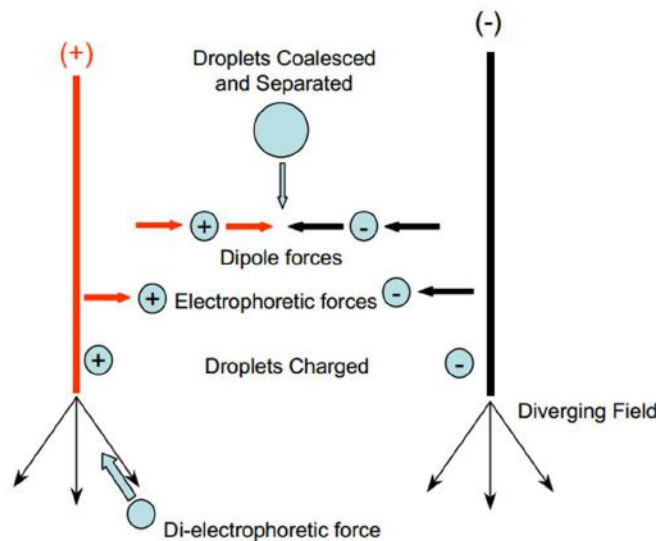


Figure 1-6: Combined AC/DC Droplet Forces [6]

1.3. Electrostatic Technologies

Dehydrator manufacturers rely on three fundamental types of electrostatic fields to enhance coalescence of the dispersed water droplets: (i) direct current (DC) fields, (ii) alternating current (AC) fields and (iii) combined AC/DC fields [6]. DC fields are highly efficient but can promote electrolytic corrosion. Therefore, they are not used in crude oil desalting applications, but only to dehydrate refined oils of low conductivity. On the other hand, AC fields are used by all manufacturers due to the tolerance to high water cuts and

to the non-electrolytic nature. Finally, combined AC/DC fields provide the high water tolerance of the AC field with the high efficiency of the DC field [16].

AC dehydrators range from electrostatic fields that utilize one AC transformer energizing a single, horizontal electrode suspended below a grounded (earth) electrode as shown in

Figure 1-7.

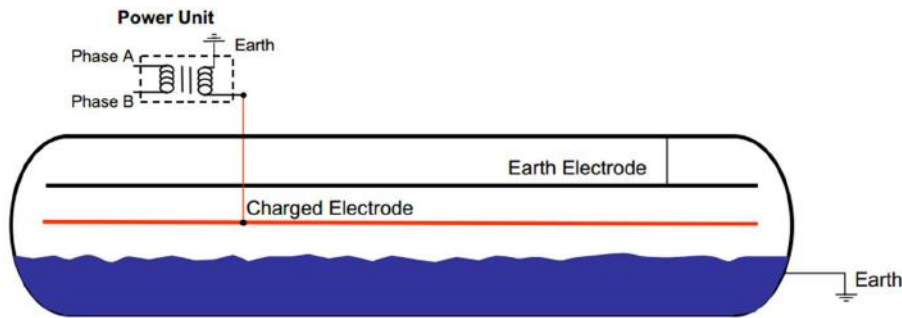


Figure 1-7: Conventional AC Dehydrator/Desalter [6]

A weak AC gradient is established between the energized electrode and the oil/water interface and a strong AC gradient is established between the energized and earth electrode. Wet oil entering the vessel just above the water interface is rapidly coalesced by the lower AC field and is then further coalesced and dehydrated by the upper field. Once the oil is above the earth electrode, additional electrostatic coalescence is impossible, since an electrostatic field cannot exist above it [6].

A more efficient AC desalter that utilize three AC transformers and three electrodes is shown in Figure 1-8. These are commonly referred to as Deep-field AC processes because they establish an AC field between the oil/water interface and the oil collector. The wet oil enters just above the interface where the low AC field promotes initial coalescence and separation. Higher AC field gradients are established between the three electrodes, where additional coalescence and separation achieve the desired performance [6].

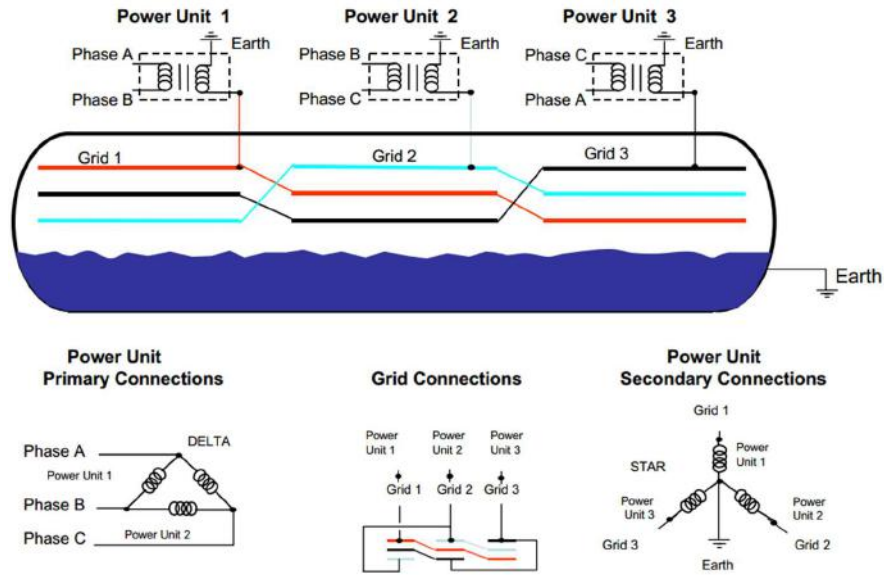


Figure 1-8: Deep Field AC Dehydrator / Desalter [6]

An aggressive electrostatic process utilizes a combination of AC and DC fields. These desalters consist of an array of vertical parallel electrodes generally positioned diametrically across the vessel, above the centerline, as shown in Figure 1-9. These desalters utilize from one to three transformers, containing a pair of reversed diodes to establish a DC field between adjacent electrodes, as shown in Figure 1-10. For a combination AC/DC desalter, an AC field is established between the bottom of the electrodes and the oil/water interface. Like the AC desalter, the lower AC field gradient promotes the initial droplet coalescence in the high water cut environment above the interface.

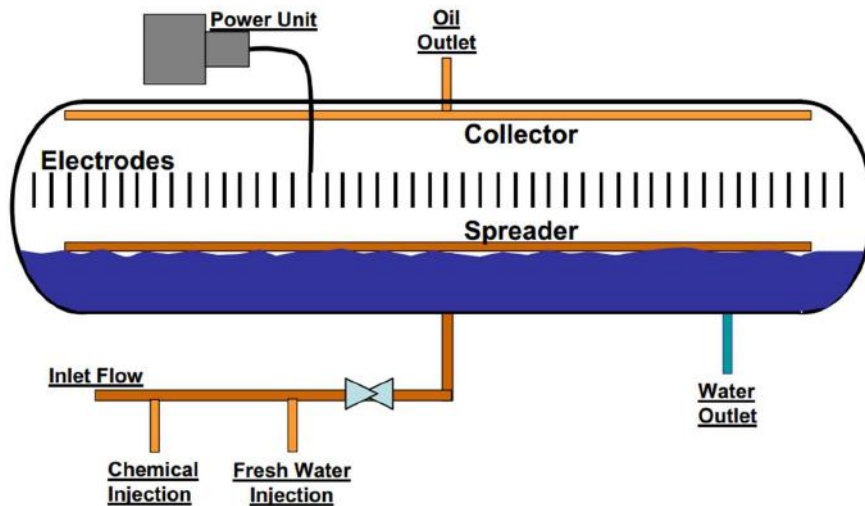


Figure 1-9: Combined AC/DC Desalter [6]

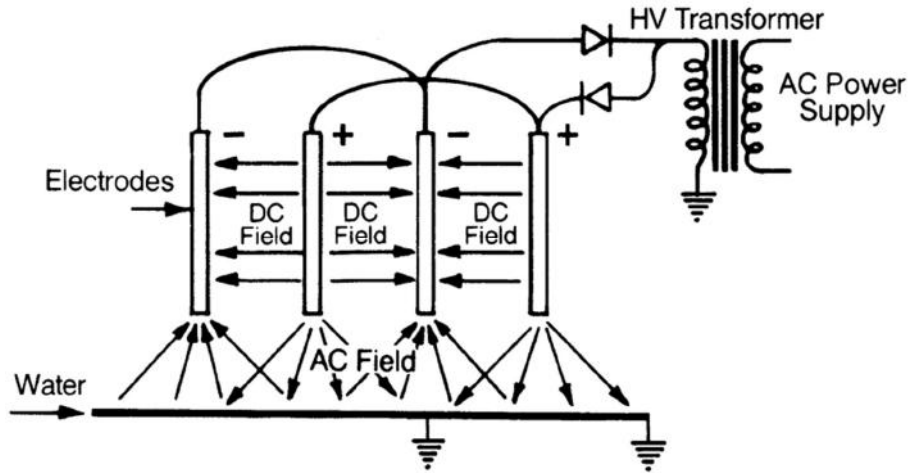


Figure 1-10: Combined AC/DC Wiring [6]

1.4. The Effect of Operating Conditions on Efficiency of Desalination Process

The efficiency of crude oil desalting process generally depends on many factors. The main factors affecting the efficiency of separation of water from crude oil are oil properties, operating temperature, electrostatic voltage, electrostatic frequency, type and amount of demulsifier, and amount of wash water [17].

1.4.1. Oil Properties

When determining the proper size of a desalter, the most important physical properties include the oil viscosity, oil density, and water density. When these properties are inserted into the Stokes law with the vertical oil velocity, as shown in Equation (1-1), the neutrally buoyant droplet (Stokes) diameter can be calculated. Larger water droplets present sufficient weight to overcome the viscous drag force and settle to the interface. Smaller droplets are lifted by the flowing oil to the desalter outlet [17].

Certain design parameters can be adjusted to achieve the desired outlet BS&W² and salt content. The oil velocity or flux is directly proportional to the desalter size and the oil flow rate. The oil viscosity is inversely proportional to the process temperature. Increasing the temperature will reduce the oil viscosity, permitting smaller water droplets to settle. However, increasing the temperature will also change the density difference and affect the droplet separation rate. As Figure 1-11 shows, the maximum density difference

² Basic sediment and water

is attained around 90 to 100 °C, decreasing if the process temperature is increased or decreased [17].

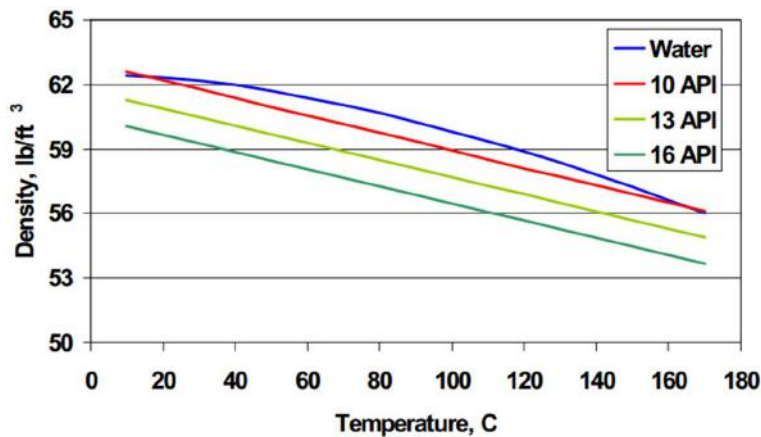


Figure 1-11: Characteristic Oil / Water Density [17]

A proper balance of the oil viscosity, density difference, and oil flow rate is essential to ensure proper performance of a desalter. While these design parameters are certainly the primary variables that influence the desalter behavior, two other parameters play key roles in the efficiency of the electrostatic process: the interfacial tension and the oil conductivity [17].

Interfacial tension ranges from 15 to 25 dynes/cm for typical oils. High interfacial tensions make difficult for droplets to coalesce, requiring higher coalescence forces to rupture the droplet interface. Low interfacial tension makes droplet coalescence easy but makes the coalesced droplets very unstable and easy to re-dispersed. Demulsifying chemicals and electrostatic fields lower the interfacial tension to promote coalescence. [18] Excessive electrostatic droplet charge or excessive chemical treatment can reduce the interfacial tension and promote droplet breakup and dispersion.

Oil conductivity ranges from 40 to 80 nS/m for typical crude oils. However, for blended oils, such as bitumen and SAGD (steam-assisted gravity drainage) oils, the conductivity of 250 nS/m has been measured. The oil conductivity is a result of excessive water in the electrode zone, polar organic and inorganic compounds and the presence of conductive solids in the oil. High oil conductivity adversely affects the electrostatic process in three ways. First, increasing oil conductivity results in the increase of resistive heating, which does not contribute to the electrostatic coalescence process. This may require the manufacturer to use a larger power unit in order to maintain the efficiency of

the electrostatic process. Second, high oil conductivity reduces the electrophoretic forces, which reduces droplet mobility in the combined AC/DC electrostatic desalter. Finally, the dielectrophoretic forces also decrease to further reduce the coalescence efficiency in both the AC and combined AC/DC processes.

Understanding the roles played by oil conductivity and interfacial tension makes possible to establish an electrostatic field that aggressively promotes droplet coalescence and achieves deeper dehydration [13].

1.4.2. Operating Temperature

In most cases, increasing temperature increases the efficiency of desalination [19]. At low temperatures, by increasing the temperature, the viscosity of crude oil decreases. As a result, the penetration and adsorption of demulsifier molecules onto the oil-water interface becomes easier [20]. Also, heat increases the capacity of crude oil to dissolve natural emulsifiers, such as wax and asphaltene. Heat also accelerates the Brownian motion of water droplets in crude oil. This factor increases the collision rate among droplets and their rate of coalescence. Consequently, the efficiency of separation of water from crude oil increases. However, if the temperature is too high, the difference between the densities of oil and water decreases. Therefore, based on the Stokes law, sedimentation of droplets becomes slower and the efficiency of separation decreases [19].

1.4.3. Electrostatic Voltages

Combined AC/DC fields utilize these electrostatic forces in order to manipulate the electrostatic voltage from the oil conductivity and interfacial tension. For clarity, the remainder of the text considers the combined AC/DC electrostatic field only.

In nearly all desalter applications, a single voltage level is applied to the electrodes to achieve a beneficial level of dehydration and desalting. However, as the force equations show, the smaller droplets require higher voltages to develop sufficient force to overcome the interfacial tension and promote coalescence. However, if the voltage is too high, the electrostatic forces may exceed the interfacial forces, resulting in droplet breakup and dispersion [17].

Two voltages define the limits of an efficient dehydration process. The first voltage can be thought of as a ‘threshold’ voltage. Figure 1-12 shows the results of a lab experiment

conducted with a combined AC/DC field. This experiment was used to determine the threshold voltage for a 20° API oil containing 10 (v/v %) of water flowing through a pilot treater. The applied voltage was increased slowly, starting at a low voltage and while measuring the secondary current. At 12.5 kV the secondary current increased sharply, suggesting that dispersed water was being electrically charged. Once the water was energized, the current began to decrease rapidly, indicating that water was coalescing. A second experiment was conducted with ‘dry’ oil. As Figure 1-12 shows, the secondary current failed to spike but continued to increase linearly with the voltage. The placement and slope of the ‘dry’ oil line are consistent with the oil conductivity.

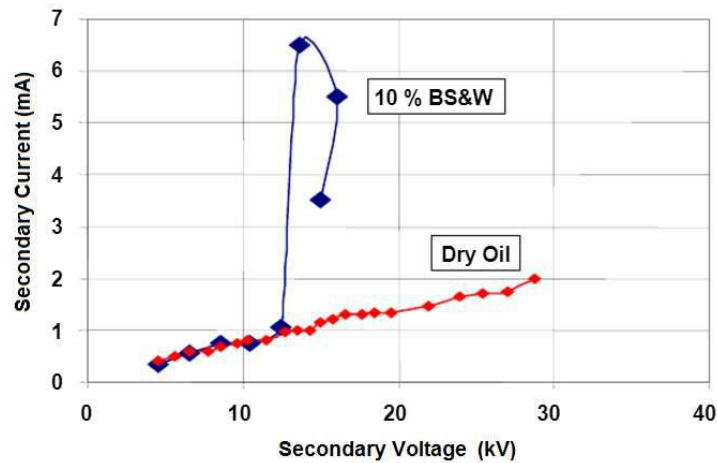


Figure 1-12: Threshold Voltage [17]

The experiment clearly indicates that operating below the threshold voltage fails to provide sufficient electrostatic energy to initiate coalescence. There is a process benefit in operating at a voltage, level near the threshold voltage because it maximizes the droplet diameters. However, it can be shown that operating at such a low voltage fails to reach the smallest water droplets required to achieve the effluent water and salt specifications [17].

For proper dehydration, the entrained water must be coalesced to a droplet diameter larger than the Stokes diameter, so that they can be separated from the rising oil. Coalescing the smallest water droplets requires an increased voltage, can be capable of developing significant electrostatic forces. However, increasing the voltage also increases the electrostatic forces on the larger droplets, which may cause them to fracture. Therefore, the applied voltage should not be increased above a level that fractures water droplets of the Stokes diameter. This voltage level can be considered the ‘critical’ process

voltage. Sustained operation above this ‘critical’ voltage results in a reduction of the water droplet diameter and a significant decline in dehydration performance [17].

1.4.4. Electrostatic Frequency

As there are two voltage limits that define the boundaries for efficient dehydration, there are also two limit frequencies for proper desalting. These two frequencies are dependent on the rate of droplet charge and discharge and the fundamental oscillation frequency of a water droplet of Stokes diameter. As **Figure 1-13** shows, when using 50 or 60 Hz power, the rate of voltage decay on the electrodes increases as the oil conductivity increases, which permits the charge on the water droplets to decrease. Furthermore, as the oil conductivity increases, the electrode voltage remains below the threshold level for a significant part of the voltage cycle. Therefore, to sustain the droplet charge and maintain the electrostatic forces for coalescence, the frequency of the applied voltage must be increased. For oil with a conductivity of 100 nS/m, the frequency must be near 1600 Hz. Operating above this ‘base’ frequency ensures the highest level of electrostatic forces [17].

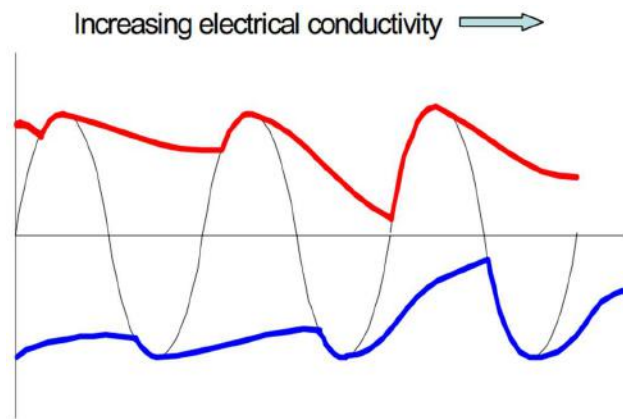


Figure 1-13: Applied Voltage vs. Oil Conductivity [17]

The fundamental oscillation frequency of a water droplet can be determined with a simple mass-spring analogy [21]. For a Stokes droplet diameter of 750 μm with an interfacial tension of 15 dynes/cm, the fundamental frequency is 20 Hz. Therefore, when operating with a 60 Hz power unit, the Stokes droplet oscillates at its third harmonic. The increased droplet oscillation amplitude may result in droplet shatter, due to increased electrostatic forces. However, by operating at a ‘modulation’ frequency below 20 Hz, the destruction

due to harmonic droplet oscillation can be avoided and maximum droplet growth can be promoted [22].

1.4.5. Type and Amount of Demulsifier

By increasing the concentration of demulsifier, the efficiency of desalination is increasable up to a maximum amount. Therefore, there always exists an optimum concentration of demulsifier, after which the efficiency decreases. Compared with natural emulsifiers present in crude oil (such as resin and asphaltene), demulsifiers present higher surface activity. Thus, even in relatively low concentrations, demulsifier can effectively replace the natural emulsifiers present in crude oil [17].

Among typical demulsifier molecules, ethylene oxide is a hydrophilic demulsifier and propylene oxide is a lipophilic demulsifier. Propylene oxide is initially at the interface between water and oil, while ethylene oxide is in the water phase. The strength of the layer formed by the mixture of demulsifier and the natural emulsifiers in crude oil is weaker than the layer formed by natural emulsifiers. Therefore, the presence of this layer increases the likelihood of coalescence of water droplets during the collision. By increasing the amount of demulsifier, the effect of displacement increases and the strength of the layer mixture decreases. However, when the concentration of demulsifier exceeds a certain amount, the molecules of demulsifier will be adsorbed to the water-oil interface and form a similar structure. This increases the strength of layers and consequently decreases the efficiency of desalination [17].

1.4.6. Amount of Wash-Water

By increasing the amount of wash water, while diluting the brine droplets, the transmission of salt to water phase increases and the efficiency of desalination increases. However, the positive effect of increasing wash water attains an optimum value [23]. After this optimum value, by increasing water, the efficiency of separation decreases. Adding wash-water increases the number of droplets in crude oil emulsion and decreases the distance between the droplets. As a result, the collision and coalescence of droplets increase. But since the efficiency of water separation is achievable up to a certain value, adding more water to the input crude oil finally causes the amount of water remaining in the crude oil to exceed from the allowed amount [17].

1.5. Concluding Remarks

In this chapter, a brief description of the electrocoalescence process was presented. The basic principles of electrostatic desalination were discussed. The electrostatic technologies were introduced and finally, the effect of operating conditions on the efficiency of the desalination process was presented.

Although the electrostatic desalination technology has been used for more than half of a century [4] a deeper phenomenological knowledge is needed to improve the understanding about the electrocoalescence process in order to design new desalting units, which are applicable to different kinds of crude oil. In this regard, experimental and theoretical works have been done in order to analyze the process from macroscopic and microscopic approaches.

In the preceding chapter, the literature available to study the electrocoalescence process from the modeling aspects is reviewed and the overall perspective of the project (problem, importance, objective, novelty, and viability) is declared.

Nomenclature

| | |
|--------------|---|
| C | constant |
| d_{Stokes} | Stokes droplet diameter (m) |
| E | electric field ($\text{kg}\cdot\text{m}^2\cdot\text{s}^{-3}\cdot\text{A}^{-1}\cdot\text{m}^{-1}$) |
| F_{dip} | Dipole force |
| F_e | Electrophoretic force (N) |
| F_{diel} | Di-Electrophoretic force (N) |
| r | droplet's radius |
| S | spacing between the center of two droplets |
| t | time |
| v_{v_c} | Vertical oil velocity ($\text{m}\cdot\text{s}^{-1}$) |
| W_d | weight of dispersed droplet (kg) |

Greek symbols

| | |
|---------------|--|
| \mathcal{E} | electrical permittivity ($\text{F}\cdot\text{m}^{-1}$) |
|---------------|--|

| | |
|-----------------|---|
| ε^* | complex permittivity = $\varepsilon - j\sigma/\omega$ (F. m ⁻¹) |
| σ | conductivity (S.m ⁻¹) |
| μ | viscosity (kg·m ⁻¹ ·s ⁻¹) |
| ρ | density (kg.m ⁻³) |
| γ | interfacial tension (N.M ⁻¹) |
| θ | angle between the electric field and the droplets center-line |
| ω | Frequency (Hz) |

Subscripts and superscripts

| | |
|----------|---------------------------------|
| <i>c</i> | continuous phase (oil) |
| <i>d</i> | droplet/dispersed phase (water) |

Abbreviations

| | |
|-------------------|--|
| <i>AC</i> | alternating current |
| <i>BS & W</i> | basic sediment and water (water content) |
| <i>DC</i> | discrete current |

Chapter 2 - Literature Review

In order to improve the understanding of desalting/dehydration processes and to select the best operational parameters and control strategies of the process, attempts have been made to model this process.

Al-Otaibi [24] used an artificial neural network to simulate and optimize the process. Considering five process parameters, including the concentration of demulsifying agents, heating, wash water, salt concentration and rate of mixing with wash water, the authors calculated the salinity and water cut efficiencies of the oil. Alves [25] developed a semi-empirical mathematical model to correlate the operational and free variables with the response variables. The authors calculated the constants of their model with the data collected from pilot plant tests for several crude oils. Other empirical and semi-empirical models have also been developed to predict the behavior of the desalination process [26–31].

Although empirical modeling has obtained some success in describing the dehydration of W/O emulsions by electrocoalescence, the development of a first-principles model is desirable. Two basic phenomenological approaches have been proposed for modeling of particle coalescence:

1. Interface tracking: Analysis of the interfacial phenomena between the layers that lead to coalescence.
2. Population balance: Extended idea of mass and energy balances to countable objects distributed in some property to describe how distributions evolve during coalescence.

Both interface tracking and population balance approaches for simulating the electrocoalescence have notably difficult problems. The difficulties arise from numerical complexities and model uncertainties that are often poorly understood or possibly misrepresented such as **(1)** droplets elongation; **(2)** occurrence of chain formation; **(3)** presence of natural emulsifiers (asphaltenes, resins, and organic acids/bases) in the crude oil; **(4)** interfacial coalescence between a droplet and its homophase; among others [32]. Besides, because of the complexity of electrostatic and hydrodynamic interactions among swarms of droplets dispersed in a fluid, a complete fundamental understanding and comprehensive prediction of the enhancement of coalescence of droplets by an electric field is lacking [33]. This fact makes the selection of appropriate correlations for the electrostatic droplet-droplet interaction forces in a non-uniform (or uniform) external

electric field, as well as the selection of the set of mechanical forces that must be considered, not an unequivocal procedure.

In the two following sections, interface tracking and population balance are discussed as the main ideas to model the electrocoalescence process.

2.1. Interface Tracking

The balance of forces that act on a droplet dispersed in oil and contribute to the conservation of linear momentum, as given by the Newton second law, can be categorized into:

- **Droplet-droplet forces:** film-thinning forces (van der Waals, electrostatic double-layer force, ionic correlation surface force, hydration repulsion), electric field induced forces (point-dipole approximation, dipole-dipole interaction);
- **Fluid-droplet forces:** drag force, Stokes drag law, buoyant force, lift forces, virtual mass force (added-mass force), history force (Basset force);
- **External field forces:** electromagnetic forces (gravity force, electrophoretic force, dielectrophoretic force).

Fluid-droplet forces influence the motion of droplets and are transferred from the fluid to the droplet through friction and pressure difference [34,35]. Buoyant and gravity forces may also be considered body forces as they act throughout the volume of a droplet.

As a general observation, lift forces, virtual mass force, and history force are not considered in most publications in the field of modeling of water/oil electrocoalescers. For example, it is known that all bodies accelerating in a fluid will be affected by added mass [36]. Since virtual mass force is dependent on the oil phase density, its effect can be neglected when dense bodies are falling in much less dense fluids.

Obviously, the set of simplification hypotheses to account for the forces through the Newton momentum equation can affect significantly the magnitude of calculated settling velocities. At low Reynolds number, the Hadamard-Rybcynski drag force [37] has sometimes been considered [34,38,39], but the quadratic drag force is mostly used [10,19,34,40,41]. Some authors have included the film-thinning force [10,34,42,43] as proposed by Davis et al. (1989) or considered the virtual mass force [10,42]. For a large droplet distance, there is no film-thinning force [43]. However, the strict use of a

correlation for dipole-induced force may eventually be invalid when the droplets get closer together than a certain critical distance that depends on droplet size [4].

A decision criterion to include film-thinning forces is the initial hypothesis on how the binary coalescence mechanism is supposed to happen:

- **The critical approach velocity mechanism [44]:** After droplets collision, there is immediate coalescence. The coalescence will occur immediately when the approach velocity exceeds a critical value at the instant of collision [45]. If the turbulent energy of the collision is greater than the total droplet surface Gibbs energy, so that the approach velocity of the colliding droplets at the collision instant exceeds a critical value, then they will coalesce [44]. This occurs if only van der Waals attraction takes place, or if electrostatic repulsion is very slight, owing to high ionic strength [46]. However, this mechanism is supposed to be unlikely between the two immiscible liquids [47]. If the energy input into the system is too great in a short period, dispersion will occur [47] before coalescence can take place [48].
- **The critical film thickness mechanism [49]:** After droplets' collision, a thin liquid film is trapped between them with a thickness of 0.01-0.001 mm [49]. As the thinning progresses, the interfacial area is reduced [4]. The film becomes unstable due to interfacial forces that play a relevant role when the thickness is lower than 100 nm [50]. At a critical thickness, the activation energy for the whole formation is a small multiple of $k_B T$, where k_B is the Boltzmann constant and T is temperature [51]. Mechanical or thermal disturbances will rupture the film, resulting in coalescence [52]. Possibly, van der Waals attraction exceeds repulsive interfacial forces (double-layer force, hydration, steric forces), resulting in coalescence after the film rupture happens [50].
- **Film drainage theory:** This deterministic approach predicts a single value for the coalescence time and cannot account for the stochastic nature of the droplets coalescence time [48]. As state above, a three-step process is involved: (1) droplets approach, (2) trapping and film drainage, and (3) destabilization of the film up to its rupture [53]. The film thinning is usually assumed to be the overall controlling step [4]. Hence, the coalescence time is attributed to the time required for the drainage of the thin trapped liquid film ($t_{\text{coalescence}} = t_{\text{drainage}}$).

The coalescence time is obtained by integrating the rate of film thinning $(dh/dt)^3$, which corresponds to relative approach velocity between two droplets V and U. Relative velocity can be determined by solving the Newton second law and then integrating film thinning rates from the initial time to collision time.

The coalescence of two droplets in an electric field is widely accepted to take place based on film drainage theory [54]. The application of an electric field polarizes an uncharged droplet so that an individual droplet can be regarded as a dipole. When aligned appropriately, the dipolar interaction of the neighboring droplets experiences an attractive force which moves them closer. An additional condition that can accelerate the droplet the approach is the non-uniformity of the electric field between the two droplets in a multi-droplet system. The presence of another droplet in the vicinity also disturbs the electric field experienced by a droplet. As a result, the electric field between two conducting droplets in a dielectric medium is always larger than the far-field, so that the induced dipole interactions become important.

As two droplets move towards each other, the medium fluid squeezes out from between the leading faces, resulting in the film thinning. A higher value of medium fluid viscosity results in a larger time to squeeze the interstitial film. When the film thickness is reduced to about 1000 Å, other surface forces influence the drainage: van der Waals attraction increases the drainage rate while double-layer repulsion decreases it. The film can become metastable when the film drainage, van der Waals attraction, and double-layer repulsion are balanced. An instability results when the attraction forces predominate via perturbations triggered by thermal fluctuations. In one of the first studies in electrocoalescence, Berg [55] found that for two anchored droplets, the coalescence rate was proportional to the magnitude of field (E_0) at low applied electric fields whereas, at the high fields, it was proportional to E_0^2 . In addition to the magnitude of the applied electric field, there are many other parameters which can determine the rate of coalescence. Such parameters include inter-droplet separation, size of the droplets, type of the applied field, shape distortion, physical and electrical properties, such as conductivity, permittivity, viscosity, and interfacial tension. The subsequent studies in electrocoalescence were focused on these parameters and their optimization, aimed towards making the process faster [56–58]. The immediate effect a droplet shows after

³ h is the distance between the surfaces of two droplets $h = s - r_V - r_U$

application of an electric field is shape-deformation, which depends upon the electrocapillary number:

$$Ca = \varepsilon_m r E_0^2 / \gamma \quad (2-1)$$

where r is the radius of the droplet, ε_m is permittivity of the medium and γ is the interfacial tension. Two closely placed droplets in an electric field exhibit deformation due to the applied field and the resulting Maxwell stress. Taylor factor ($E_0 \sqrt{2a\varepsilon_m / \gamma}$) for the stability of a droplet in an electric field [59], above which a droplet breaks, is 0.648; but it is lower for the droplets in a pair and depends on the inter-droplet separation [60,61]. The shape deformation can lead to mutual contact and coalescence, even if the droplets were initially held stationary [62,63].

The electrostatic force of the dipole-dipole interaction between two conducting droplets of uniform size surrounded by a dielectric medium and aligned with the applied electric field is given by Equation (2-2) [57,64].

$$F_{dip} = -24\pi\varepsilon_m r^6 E_0^2 / s^4 \quad (2-2)$$

where s is the center-to-center separation between two droplets. The expression for F_d is valid in the large separation limit and it indicates that the attractive force sharply increases with decreasing separation [60,62,65,66]. Therefore, for two droplets to attract and coalesce, they must be within an ambit which is determined by a combination of the magnitude of the applied field, droplet radius, and fluid properties. In an emulsion, the inter-droplet separation is determined by the volume fraction of the dispersed phase and droplet size [58].

The motion and interaction of two liquid droplets in an electric field are quite different from that of rigid particles on account of the drag, film-drainage and two-droplet interaction, being governed by different mechanisms [34]. Atten [65] theoretically investigated the critical conditions for the deformation and coalescence of two closely-held droplets (of equal and unequal sizes) in an electric field. It was found that the coalescence occurs when the deformed inner poles come closer than 45% of their initial separation upon application of an electric field. In another study, Atten [66] suggested that there exists a critical field of distortion for every separation for a pair of droplets in an electric field, given by Equation (2-3):

$$(d_0/r)_{crit} = 8(E_0\sqrt{\varepsilon_m r/\gamma})^{1.22} \quad (2-3)$$

Here, d_0 is the initial distance between inner poles beyond which coalescence cannot be observed. Similar studies reported the effect of distance between the facing poles (d), of anchored and freely suspended droplets, on the droplet shape and coalescence [62,63]. Brazier-Smith [67] numerically investigated the probability of the coalescence and possible shapes during the interaction of two droplets in an electric field. They concluded that, when the separation $d_0/r < 1.2$, droplets deform, readily attract and eventually coalesce. However, when $d_0/r > 1.2$, the inner surfaces deform, assume a conical shape with an angle equal to the static Taylor cone angle and finally give rise to the jets of fine droplets. Such a disintegration hampers the rate of electrocoalescence, as it introduces finer droplets in the emulsion.

Through the introduction of interfacial tension, the effect of natural emulsifiers (asphaltenes, salts) in crude oil can be investigated, since the interfacial tension correlates directly to surfactant concentration through the Langmuir equation [68].

It is known that an increase in the amount of surfactant almost always increases the coalescence time. Water droplets flowing through the viscous oil experience shear stresses that conduct surfactants towards zones with lower velocity gradients, where they accumulate. Local differences in concentrations induce reverse interfacial flows (called Marangoni flows) [62]. The presence of surfactants at the interface, accompanied by droplet elongation, causes an interfacial tension gradient that leads to Marangoni stresses. The interfacial stresses inhibit the generation of internal circulation [35]. The thinning rate is in turn affected by the capillary pressure and disjoining pressure. It can thus be retarded due to the Marangoni effect [52]. An increase in bulk viscosity of the surfactant solution will also decrease the thinning rate. Finally, surfactants decrease the interfacial tension and can lead to the formation of very tiny secondary droplets ($\sim 1 \mu\text{m}$) that are much more difficult to undergo sedimentation. As the interfacial tension decreases, the critical electric field (E_{crit}) decreases, which leads to the formation of unstable secondary droplets [69].

After droplet-droplet contact, the thin film separating two droplets attains a critical thickness and its subsequent rupture leads to the coalescence. The critical thickness of film rupture is given by Equation (2-4) [70].

$$h_{crit} = (Ar/8\pi\gamma)^{1/3} \quad (2-4)$$

where A is the Hamaker constant. The mechanism for the film rupture and subsequent merging of two droplets has been proposed in the literature. One of the hypotheses suggests that the film can break when the electric field across the film attains the dielectric breakdown strength of the medium phase [71–73]. This hypothesis was proved wrong by Priest et al. (2006) with their study of selective coalescence of the droplets in a microfluidic channel. Their analysis suggested that it is not the dielectric breakdown but the electric-field-induced dynamical instability of the oil-water interface that drives the coalescence. The mechanism proposed by Berg [55] stated that the coalescence involves continuous making, breaking, and rearrangement of the intermolecular bonds over the two interfaces in contact. They proposed two different mechanisms of droplet-droplet coalescence at low and high applied electric fields. At the low applied field, the rearrangement of bonds results in coalescence [55]. Rearrangement of bonds is proportional to the rate of reorientation of bonds, which in turn is proportional to $P_{dip}E_0$. Here, P_{dip} is the dipole moment of the bonds. When the applied electric field is high, simultaneous breakup and buildup of bonds lead to the coalescence. The condenser of droplet surfaces supplies energy ($=1/2C\Phi^2$) for the bond breakup, where C is the capacitance and Φ is the voltage at droplet surface [55]. There are other factors that determine whether droplets would coalesce on contact. Bird [74] showed that the oppositely charged droplets in an electric field attract each other, but whether they coalesce or retreat back is dependent on the cone angle they make on contact. Their analytically predicted critical cone angle and its experimentally observed value (30.8°) were close. Atten [14] proposed a mechanism for the droplet repulsion after contact which suggests that at a high C , coalescing droplets make a thin, thread-like bridge between them. After the contact, an abrupt exchange and redistribution of the electrical charge drive the droplets apart.

Although there are several modeling studies addressing different fundamental aspects of electrocoalescence of two water droplets dispersed in crude oil, there is still a huge gap between modeling and experimental studies. Modeling is still in its very primary steps to analyze the rupture of two droplets. In addition, the assumptions made for modeling of interface tracking are sometimes so controversial that overshadow the trustworthiness of the problem, when compared to the practical cases in the industry. Finally, to simulate the

practical electrocoalescence process, which is, in fact, the interaction of the whole population of droplets, interface tracking does not seem to be sufficient.

2.2. Population Balance

A convenient way of modeling particulate systems is the population balance equation (PBE), which has been used by chemical engineers to model a wide range of dispersed phase systems, such as liquid-liquid extraction, solid-liquid leaching, bioreactors, fluidized bed and dispersed phase reactors, and many more [75–81].

A general differential form of mono-variate PBE is presented in Equation (2-5) [82]. A PBE has external and internal dimensions. The external dimensions of a PBE are dimensions of the environment, which are the 3-D space (x,y,z or r,z,q or r,q,f) and time. The internal dimensions of a PBE are dimensions of the population such as diameter, volume, surface area, concentration, age, molecular weight, number of branches, etc.

$$-\nabla[u_d n] + \nabla[D_d \nabla n] - \frac{\partial}{\partial V}[Gn] + S = \frac{\partial n(v, z, t)}{\partial t} \quad (2-5)$$

In this equation, n is the droplet number density function which represents the average number of droplets per unit volume of droplet state space. In the representation of Equation (2-5), n is a function of v that characterizes the size of droplets, Z : the special position of the droplets, and t : time. The first two terms on the left-hand side of Equation (2-5) represent the convection and diffusion of the droplets. The third term on the left-hand side of the equation denotes the growth of the droplets and the source term: S is related to the aggregation, breakage, and nucleation of droplets. Based on the droplet-droplet phenomena occurring in a specific particulate system, the general PBE is modified to derive the formulation of a population balance model (PBM). In case of necessity, other governing equations should be coupled with the PBE to have realistic modeling of the problem.

In an industrial electrostatic desalter, the oil upward velocity is usually designed to be around 0.2 cm/sec [4]. Consequently, the flow is usually laminar and an average velocity can be considered for the oil. On the other hand, the distance between the electrodes depends on the crude oil type and the required electric field strength. This distance is usually considered to be in the order of 20 cm [4]. Therefore, the calculated Peclet number (Equation (2-6)) is quite higher than unity, and the droplet diffusion can be neglected.

$$Pe = \frac{u_{ch} L_{ch}}{D_d} \quad (2-6)$$

Growth and nucleation usually do not take place during electrocoalescence [4]. The droplet breakage is also not considered in this work as the electric field strength is assumed to be lower than the critical value given by Equation (2-7) [57] in order to prevent the breakage of droplets.

$$E_{crit} = 0.64\sqrt{\gamma/2\epsilon r} \quad (2-7)$$

If the electric strength exceeds this threshold, various droplet breakage mechanisms may occur [4]. Therefore, the resulting population balance equation for an industrial electrostatic desalter can be given by Equation (2-8).

$$\frac{\partial n(v, r, t)}{\partial t} + \nabla[u_d n] = \frac{1}{2} \int_0^v n(v-v', r, t)n(v', r, t)Q(v-v', v')dv' - \int_0^\infty n(v, r, t)n(v', r, t)Q(v, v')dv' \quad (2-8)$$

The two terms on the right-hand side of Equation (2-8) represent the rates of birth and death due to aggregation, respectively [82]. Here Q is the aggregation frequency and represents the probability per unit time of a pair of particles of specified states to aggregate. Alternatively, it represents the fraction of particle pairs of specified states aggregating per unit time.

The process of determining aggregation frequency is not so straightforward. Aggregation frequency is normally dependent on the mechanism of aggregation as well as some adjustable parameters, which should be determined using experimental data. Table 2-1 presents a number of aggregation frequencies (aggregation kernel) derived theoretically for the coalescence of water droplets dispersed in crude oil. They are all determined based on the mechanisms that predict the relative motion of the droplets.

Table 2-1: Aggregation frequencies presented in the literature for water/oil coalescence.

| AGGREGATION FREQUENCY(Aggregation Kernel) | REFERENCE |
|---|-----------|
| $Q = \pi (r_V + r_U)^2 u_V - u_U e_{VU}$ | [83] |
| $Q = \frac{16\pi \varepsilon_o E^2 (r_V r_U)^2}{3\sqrt{3} \mu_o (r_V + r_U)}$ | [57] |
| $Q = Q _{ROGERS \& DAVIS(1990)}, e_{VU} = 0.45 \left(\frac{2\lambda (\rho_W - \rho_o) g r_V}{3\varepsilon_o (1 + \lambda)^2 E^2} \right)^{-0.55}$ | [84]) |
| $Q = \pi (u_V^{(0)} - u_U^{(0)}) y_c^2, \lim_{r \rightarrow \infty} u_V - u_U = u_V^{(0)} - u_U^{(0)}, e_{VU} = 0.3\delta^{0.5} + \frac{1}{2}Bo\delta^6$ | [85]** |
| $\left\{ \begin{array}{l} \text{For } r_V + r_U < \varphi: \\ 4\pi \left(\int_0^{\varphi^*-1} \frac{\exp(U_{V,U}^{VW}/kT) \beta_{V,U}(y)}{(\varepsilon/\nu)^{0.5} (r_V + r_U)^4 (y+1)^4} dy + \int_{\varphi^*-1}^{\infty} \frac{\exp(U_{V,U}^{VW}/kT) \beta_{V,U}(y)}{\alpha \varepsilon^{1/3} (r_V + r_U)^{10/3} (y+1)^{10/3}} dy \right) \\ \text{For } r_V + r_U > \varphi: \\ 4\pi \left(\int_0^{\infty} \frac{\exp(U_{V,U}^{VW}/kT) \beta_{V,U}(y)}{\alpha \varepsilon^{1/3} (r_V + r_U)^{10/3} (y+1)^{10/3}} dy \right)^{-1}, \varphi^* = \varphi (r_V + r_U)^{-1} \end{array} \right.$ | [86] |
| $\left\{ \begin{array}{l} Q = \exp\left(-\frac{t_d}{t_V}\right) e_{VU}, e_{VU} = \left(\frac{8\pi}{3}\right)^{\frac{1}{3}}, u_V - u_U = d_{eq} \dot{\gamma}, \Theta_{\max} = \frac{2h_0^2 \rho_o \sigma}{We_0 \mu_w^2 d_{eq}} \\ Q = \frac{\Theta_{\max}}{\pi} \left(1 - \frac{k_{cl,2}^2 (We - We_0)^2}{\Theta_{\max}^2}\right)^{\frac{1}{2}} e_{VU}, e_{VU} = \left(\frac{2\pi}{3}\right)^{\frac{1}{2}}, u_V - u_U = (\varepsilon d_{eq})^{\frac{1}{3}} \end{array} \right.$ | [87] |
| $Q = Q _{ROGERS \& DAVIS(1990)}, e_{VU} = \frac{y_c^2}{(r_V + r_U)^2}$ $v_{VU}^{(0)} = \left\{ 2 \left(\frac{\mu_W}{\mu_o} + 1 \right) \rho_W - \rho_o r_V^2 \left[1 - \left(\frac{r_V}{r_U} \right)^2 \right] g \right\} \left[3 \left(3 \frac{\mu_W}{\mu_o} + 2 \right) \mu_o \right]^{-1}$ | [88] |
| $Q = Q _{ROGERS \& DAVIS(1990)}, e_{VU} = (A_1 E + A_2) (x_{W,t=0})^{(B_1 E + B_2)}$ $v_{VU}^{(0)} = (u_V^\circ - u_U^\circ) \left[\frac{\overline{hh}}{s^2} L(h) + \left(I - \frac{\overline{hh}}{s^2} \right) M(h) \right] - \frac{D_{ij}^\circ}{kT} \left[\frac{\overline{hh}}{s^2} G(h) + \left(I - \frac{\overline{hh}}{s^2} \right) H(h) \right] \nabla \psi_{VU}$ | [39] |
| $Q = \left(\frac{2k_B T}{3\mu_o} (r_V + r_U) \left(\frac{1}{r_V} + \frac{1}{r_U} \right) + \begin{cases} 0.163 \sqrt{\frac{\xi}{u_z}} (r_V + r_U)^3, & (r_V + r_U) < 2\varphi \\ 0.272 \pi \xi^{1/3} (r_V + r_U)^3, & (r_V + r_U) \geq 2\varphi \end{cases} \right) e_{VU}$ | [89]* |

* Kernel combines Brownian and turbulent flow.

** Empirical correlation under the absence of electric field.

The Brownian kernel was adopted jointly with a kernel for turbulent motion by Mitre [89]. It is applicable to monodisperse systems in an open domain. Some coalescence processes are supposed to occur due to Brownian motion, but this effect is not significant when compared to electrocoalescence [4]. Roger's equation [83] refers to the Smoluchowski model [90]. It assumes that there are no hydrodynamic interactions between the particles. Hydrodynamically interacting spheres have a reduced collision rate when compared to one predicted by this equation (even if van der Waals forces are included) since small particles tend to follow streamlines around larger particles. In contrast, deformable drops present enhanced rates of coalescence and collision rates can be greater than predicted [85].

In Table 2-1, kernels exhibit very different formulations, but those used by Zhang et al. [84], Lo & Rao [87], Meidanshahi et al. [91] and Parvasi et al. [39] obey Rogers & Davis's [83] framework. They differ in how the coalescence efficiency (e_{VU}) and the relative settling velocity ($u_V - u_U$) are calculated. $u_{VU}^{(0)}$ is the relative velocity in function of μ_w/μ_o ratio. e_{VU} function is determined by the integration over the drop surface at infinity, enclosing all possible drop trajectories which result in coalescence [85]. $e_{VU} = 1$ when drops move on straight paths without interacting with each other. Once aerodynamic forces that cause the drops to move around one another and van de Waals forces that pull them together are taken, $e_{VU} \neq 1$ [83]. $e_{VU} > 1$ is found for large drops (radius $\gg 30 \mu\text{m}$) that fall with moderate or high Reynolds due to wake capture [83].

Meidanshahi et al. [91] modeled a pilot plant of electrostatic desalting drum based on the population balance equation at steady-state condition. They calculated the droplet size distribution at the outlet of the drum considering an arbitrary inlet size distribution for water droplets. In their work and other similar articles [92,93], the droplets' velocity (Equation (2-9)) is considered as the differences between the continuous phase and Stokes [36] velocities. When Stokes settling velocity of a droplet is larger than the continuous phase velocity, it can fall and settle; otherwise, it moves upward with the continuous phase due to the dominant drag force imposed by the continuous crude oil phase.

$$u_d = u_c - \frac{(\rho_d - \rho_c)gr^2}{18\mu_c} \quad (2-9)$$

In fact, they considered that all drops move with the continuous phase velocity unless they are affected by settling. Although this assumption seems practical, we believe that it is not necessarily true. In this case, computational fluid dynamics can be used to calculate the velocity of multiphase flow.

Fluid dynamics is the study of fluid under motion. Fluid flow is governed by a set of equations satisfying conservation of mass, momentum, and energy. Computational fluid dynamics (CFD) is the science of predicting fluid flow, heat transfer, mass transfer, chemical reactions, and related phenomena by solving the mathematical equations which govern these processes using numerical methods (i.e., on a computer).

For many years CFD was only being used to study the fluid dynamics of single-phase flow. But in recent years it is extended to analyze the fluid dynamics of multiphase flow. Multiphase flow is the simultaneous flow of a mixture of phases such as gases (like bubbles) in a liquid, or liquid (like droplets) in gases and similar such flows. Multiphase flows are found in many industrial applications like chemical reactors and process flow industry. Therefore, the knowledge of multiphase flow physics is extremely important in order to carry out any experimental or simulation study in this area [94].

Two basic specifications have been proposed for analyzing multiphase flows [95]:

Eulerian specification: Focuses on specific locations in the space through which the fluid flows as time passes.

Lagrangian specification: Follows an individual fluid parcel as it moves through space and time.

Based on these two specifications, there are three main approaches for modeling of multiphase flows [95]:

Eulerian-Lagrangian Model: The continuous phase is modeled using the Eulerian framework and the equation of motion is solved for the dispersed phase (Lagrangian framework). The dispersed phase can exchange momentum, mass, and energy with the fluid phase. Since the particle or droplet trajectories are computed for each particle or for a bundle of particles that are assumed to follow the same trajectory, the approach is limited to systems with a low volume fraction of dispersed phase. Here, the volume displacement due to the dispersed phase motion is ignored. The continuity and momentum equations for the Eulerian-Lagrangian approach are:

$$\frac{\partial(a_c \rho_c)}{\partial t} + \nabla \cdot (a_c \rho_c u_c) = S_c \quad (2-10)$$

$$\frac{\partial(a_c \rho_c u_c)}{\partial t} + \nabla \cdot (a_c \rho_c u_c u_c) = -a_c \nabla p - \nabla \cdot (a_c \tau_c) + a_c \rho_c g + S_{c,m} \quad (2-11)$$

The trajectories of the dispersed phase are calculated using the equation of motion. Here, Newton's second law is used for force balance of single dispersed particle:

$$m_p \frac{du_p}{dt} = F_p + F_D + F_{VM} + F_L + F_B + F_G \quad (2-12)$$

In Equation (2-12), F_p is the pressure force, F_D is the drag force, F_{VM} is the virtual mass force, F_L is the lift force, F_B is the buoyancy force, and F_G is the gravitational force.

Eulerian-Eulerian Model: Within the Eulerian approach, the dispersed phase is also treated as a continuum and the Eulerian equation is solved for all of the phases. The model is derived by ensemble averaging or volume averaging. Coupling between phases is represented by various interphase transport models. This approach is suitable for high dispersed phase volume loading (>10%). The continuity and momentum equations for phase k with volume fraction of a_k are:

$$\sum_k a_k = 1 \quad (2-13)$$

$$\frac{\partial(a_k \rho_k)}{\partial t} + \nabla \cdot (a_k \rho_k U_k) = \sum_{p=1, p \neq k}^n S_{pk} \quad (2-14)$$

$$\frac{\partial(a_k \rho_k U_k)}{\partial t} + \nabla \cdot (a_k \rho_k U_k U_k) = -a_k \nabla p - \nabla \cdot (a_k T_k) + a_k \rho_k g + F_l + F_d + F_{VM} + F_g \quad (2-15)$$

Volume of Fluid Model: This approach utilizes the Eulerian framework for all phases. It is designed for immiscible fluids where the position of the interface between the fluids is of interest. In the Volume of Fluid (VOF) model, a single set of momentum equations is shared by the fluids, and the volume fraction of each of the fluids in each computational cell is tracked throughout the domain. This model is especially suitable for stratified and separated flows where a distinct interface is present between phases. Therefore, it is not

applicable to a system with many small drops or bubbles. The continuity and momentum equations for the volume of fluid model are:

$$\sum_k a_k = 1 \quad (2-16)$$

$$\frac{\partial(\rho)}{\partial t} + \nabla \cdot (\rho u) = \sum_k S_k \quad (2-17)$$

$$\frac{\partial(a_k)}{\partial t} + (u_k \cdot \nabla) a_k = S a_k \quad (2-18)$$

$$\frac{\partial(\rho u)}{\partial t} + \nabla \cdot (\rho u u) = -\nabla P + \nabla \cdot [\mu(\nabla u + \nabla u^T)] + \rho g + F \quad (2-19)$$

In order to select the proper multiphase model, first, the flow regime should be distinguished. Flow regime is a geometrical pattern or distribution of flow which is usually recognized by visual inspection. The different types of flow regimes are [95]:

Bubbly flow: dispersed gaseous or fluid bubbles in a continuous fluid

Droplet flow: dispersed fluid droplets in a continuous media

Stratified flow: immiscible fluids separated by an interface

Slug flow: large sized bubbles in a continuous fluid

Particle-laden flow: discrete solid particles in a continuous gas

Fluidized bed: consists of a vertical cylinder containing particles where gas is introduced through a distributor

Slurry flow: transport of particles in liquids

Three phase flows: gas-liquid-solid reactors

The different types of gas-liquid flow regime in a vertical pipe is shows in [Figure 2-1](#) [95].

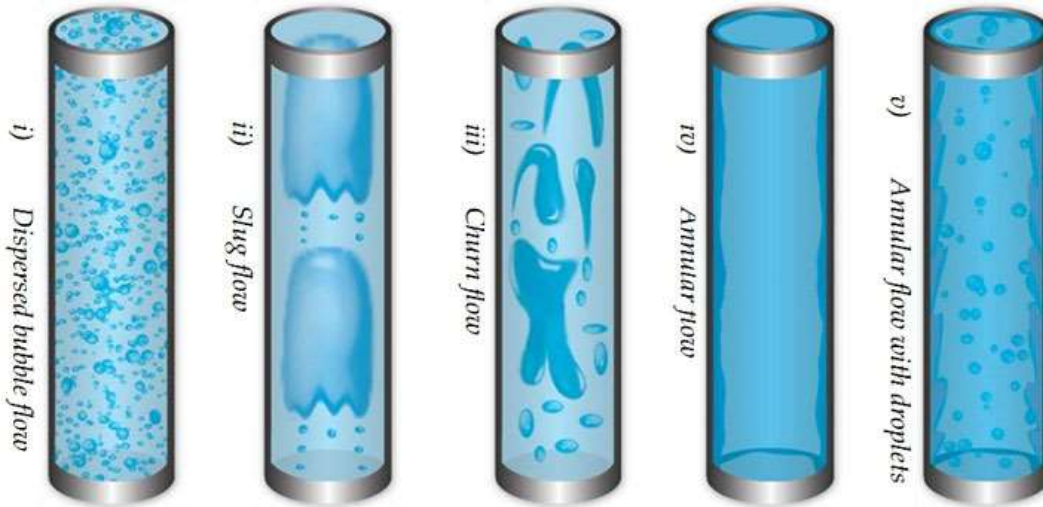


Figure 2-1: Different types of gas-liquid flow regime in a vertical pipe [95]

A general recipe on how to select the proper multiphase model is proposed in Table 2-2 [96].

Table 2-2: Selection of the multiphase model

| Type of Flow | Eulerian-Eulerian Model | Volume of Fluid Model | Eulerian-Lagrangian Model |
|--|-------------------------|-----------------------|---------------------------|
| Bubbly, droplet, and particle-laden flows volume fractions are less than or equal to 10% | | | ✓ |
| Bubbly, droplet, and particle-laden flows in which the phases mix and/or dispersed-phase volume fractions exceed 10% | ✓ | | |
| Slug flows | | ✓ | |
| Stratified/free-surface flows | | ✓ | |
| Pneumatic transport homogeneous flow | ✓ | | |
| Pneumatic transport granular flow | ✓ | | |
| Fluidized Beds | ✓ | | |
| Slurry flows and hydro-transport | ✓ | | |
| Sedimentation | ✓ | | |

The process of crude oil desalination by electrocoalescence is a typical example of a polydisperse multiphase flow. Polydisperse multiphase flows are of great importance not only in the case of emulsion flow but also in several other types of equipment found in chemical engineering, as in extraction columns, cyclones, hydrocyclones, bubble columns and multiphase stirred tank reactors to cite just a few [82,97]. This kind of flow

is characterized by one or more phases that are dispersed, like bubbles, droplets or particles, in a continuous medium [98–100]. Despite a large number of works published in the literature over the last decades [101–105], polydispersed multiphase flows are still subject of intense research and due to their inherent complexity, its modeling is not so consolidated as that for single-phase flows. In this perspective, the use of computational fluid dynamics (CFD) to solve an Eulerian-Eulerian multi-fluid model coupled with a PBM has shown to constitute an efficient tool to simulate polydisperse multiphase flow [97,106–114]. The accuracy of this approach heavily relies on the adequacy of the employed particle-particle interactions models, which are not generally applicable and have adjusted parameters that usually depend on the characteristics of the multiphase system [45,115,116]. The development of models to represent the particle-particle interactions, like breakage and coalescence, in polydisperse multiphase flows is a subject of intense research. Several models were proposed in the literature to take into account different multiphase systems as well as to improve the agreement between the simulation results and experimental data. Despite that, there is still a lack of models that are sufficiently generic and useful to be applied to actual processes found in the industry.

A great query around polydisperse multiphase flow simulation is to choose the method for solving the population balance equation (PBE). Several mathematical methods have been offered to solve the PBE. Some of the main mathematical techniques to solve PBE are: Monte Carlo stochastic methods [117,118], weighted residuals methods (WRM) [119–122] methods of classes (MoC) [123,124], sectional methods (SM) [125–127], and methods of moments (MoM) [110,112,128–131]. However, there is no method that is accurate, efficient and robust at the same time for the general solution of the PBE. Based on the mathematical and physical characteristics of the PBE and its initial and boundary conditions, the proper solution technique can be chosen. Here a general recipe is proposed (Ramkrishna, 2000):

- If the analytical method works
 - Similarity solution (Ramkrishna, 2000)
 - Laplace transform (Ramkrishna, 2000):
- If it is crucial to get distribution detail right, and it is a 1-D problem, and it is a stand-alone model
 - Sectional Methods
 - Monte Carlo
 - Weighted residuals methods

- Methods of classes
 - If an approximate distribution will do, or if the moments are sufficient, or if the distribution is multivariate, or if the model will be embedded in a larger model
 - Moments

Due to their easy application, reasonable accuracy, and computational cost, the moment methods are preferable to couple the population balance with CFD codes [97,107,112,113,132]. These methods solve for a selected set of lower-order moments of the particle distribution function (PDF). A drawback of the standard moment method is that the obtained system of equations is unclosed [133]. This problem was contoured by the quadrature-based moment methods (QBMM) which uses an N-point Gaussian quadrature approximation closure whose weight function is the PDF [128]. The so-called Gauss-Christoffel quadrature is calculated from the moments of the PDF, leading to a straightforward discretization of the internal coordinate domain and making this method quite amenable to be implemented in the existing CFD codes [108,134,135]. The QBMMs most widely used are the Quadrature method of moment (QMoM) [128], Direct Quadrature method of moment (DQMoM) [129], Conditional Quadrature Method of Moments (CQMOM) [136,137], and Extended Quadrature Method of Moments (EQMOM) [138].

The other phenomena happening simultaneously with coalescence in electrocoalescence of crude oil is the creation/segregation of the free water phase. Most modeling approaches are based on more fundamental coalescence research work [53] rather than on the sedimentation step. The higher density of water droplets compared to oil density drives sedimentation. Table 2-3 presents a number of settling velocities derived theoretically for the coalescence of water droplets dispersed in crude oil. When a spherical solid settles in the oil phase under creeping flow regime specified strictly by the gravity, buoyant and drag forces, the Stokes law determines the settling velocity. However, Stokes settling velocity [36] is only valid for a single solid sphere, away from any wall, when the non-slip boundary condition is applicable [4].

Table 2-3: Settling velocities presented in the literature for water/oil coalescence.

| SETTLING VELOCITIES | REFERENCE |
|---|-----------|
| <p>Stokes Velocity</p> $v_z = \frac{2(\rho_w - \rho_o)gr_V^2}{9\mu_o} \begin{cases} \text{Re} < 0.1 \\ \text{solid spheres} \end{cases}$ | [36] |
| <p>Hadamard-Rybczynki Velocity</p> $v_z = \left[\frac{2(\rho_w - \rho_o)gr_V^2}{9\mu_o} \right] \left(\frac{\mu_w + \mu_o}{\mu_w + \frac{2}{3}\mu_o} \right) \begin{cases} \text{Re} < 0.1 \\ \text{liquid spheres} \end{cases}$ | [37] |
| <p>Richardson-Zaki Velocity</p> $v_z = \left[\frac{2(\rho_w - \rho_o)gr_V^2}{9\mu_o} \right] (1 - v_{f,w})^\alpha \quad \therefore 2.3 < \alpha < 5$ | [139] |

According to Frising [53], Stokes law is not appropriate at high concentration and counterbalance two systematic errors: **(1)** the overestimation of the settling velocity of drops hindered to settle by the neighboring droplets, **(2)** the underestimation of the growing mean drop diameter, since this law is only valid for rigid spheres. Eow [4] pointed out the need for Stokes settling velocity modification, in order to account for a particle near a wall, multiple particle settling (especially if not monodisperse) and circulation of the internal phase, if the particle is a liquid. In the case of fluid particles and in the absence of surface-active components, internal circulation inside the particle will reduce the drag force [140]. Hadamard-Rybczynski settling velocity address this issue by multiplying a non-empirical viscosity correction term to Stokes velocity (Table 2-3). Despite that, the non-slip boundary condition may still be applicable if surfactant renders the interface immobile [4].

The Hadamard-Rybczynski settling velocity will approach the Stokes settling velocity as the viscosity ratio diminishes ($\mu_w/\mu_o \rightarrow 0$). Hadamard-Rybczynski Theory predicts a settling velocity up to 50% greater than the Stokes equation [38] at no asymptotic conditions. It is consistent with the fact that, unlike spheres, a higher velocity of the droplets rising in the pure liquid is expected due to the mobility of the liquid/liquid interface, which reduces the drag force exerted on the droplets [141]. Hadamard-Rybczynski formula agrees with empirical terminal velocities obtained for drops free of emulsifiers when exposed to the electric field [68]. When the presence of surfactant is

accounted for, Stokes formula for rigid bodies shows good results [68], whereas drops were found experimentally to move significantly slower than predicted by the Hadamard-Rybczynski equation. This fact has been attributed to the existence of stagnant caps at the trailing end of the droplet, where the surface velocity vanishes [38]. According to Mhatre [142], depending on the adsorption and desorption rate of the surfactant molecules, at very low and very high concentrations a drop obeys the Hadamard–Rybczynski model. However, Stokes law gives better estimates for drag force at intermediate concentrations.

Unlike Stokes and Hadamard-Rybczynski equations, Richardson-Zaki equation is an empirical approach for settling velocities. It was fitted with the primary subject of including the volume fraction of the dispersed phase (v_d). The water content is one of the most important variables for the stability of petroleum emulsions. Settling velocities go down as the water content increases. High settling velocities have been found at low water contents, even when very small droplets were present [140].

Hypothetically, water sedimentation from oil phase may occur by **(1)** aggregation, followed by sedimentation; **(2)** aggregation, followed by coalescence, and then sedimentation; **(3)** coalescence, followed by sedimentation. Sedimentation happens to certain drop size, not discussed by any modeling approach cited here. In particular, Meidanshahi [143] assumed it to be equal to or larger than 20 μm . Gravitational sedimentation is normally limited to particles of relatively large size, because the rate of sedimentation for small particles is too low to give a practical analysis time, and because Brownian motion of small particles becomes too large to allow for effective settling. Very small particles ($< 0.1 \mu\text{m}$) never settle by gravity, unless they are extremely dense (Scott et al., 2005). Sedimentation under the influence of an electric field extends the amount of removed water, as many of the small droplets will coalesce to form a bigger drop size. However, considering a certain size as the sedimentation limit similar to what has been done in the work of Meidanshahi [143], makes the model strict and not applicable to all kinds of crude oil. This is one of the issues that was addressed in this work.

2.3. Overall Perspective of the Project (Problem, Importance, Objective, and Novelty)

Problem

Despite the attempts made to model the electrocoalescence of crude oil, deeper knowledge is needed for designing new desalting units, which are applicable to different kinds of crude oil. The models developed to simulate the process are still not widely valid. The population balance equation seems to be a good idea for modeling the coalescence of water drops. However, the aggregation kernels proposed in the literature for the electrocoalescence are not enough robust for different kinds of crude oil. Moreover, the fluid dynamics of dispersed phase coupled with the coalescence of drops are still yet not sufficiently discussed. Besides, the simultaneous sedimentation of water droplets in the oil phase with coalescence is still not sufficiently studied. It seems that a better criterion is needed to consider the practical case of sedimentation.

Importance

Figure 2-2 shows the world conventional and unconventional liquid production. The figure depicts the continuous decrease of conventional and increase of unconventional oil production. In fact, as the extraction from oil fields increases, the saline content of oil fields also increases, which leads to the production of crude oils with lower qualities. This matter highlights the increasing importance and necessity of crude oil desalination process knowledge.

Objective

The objective of this work was to develop and implement a phenomenological model to describe the crude oil desalting operation using electrostatic fields, based on experiments conducted in the laboratory and pilot plant. The CFD-PBE coupling was used as the principal idea to conduct the modeling. CFD analyzes the fluid dynamics of continuous and dispersed phases and PBE evaluates the evolution of water droplets due to electrocoalescence. In addition, a proper criterion was introduced to model the creation/segregation of the free water phase.

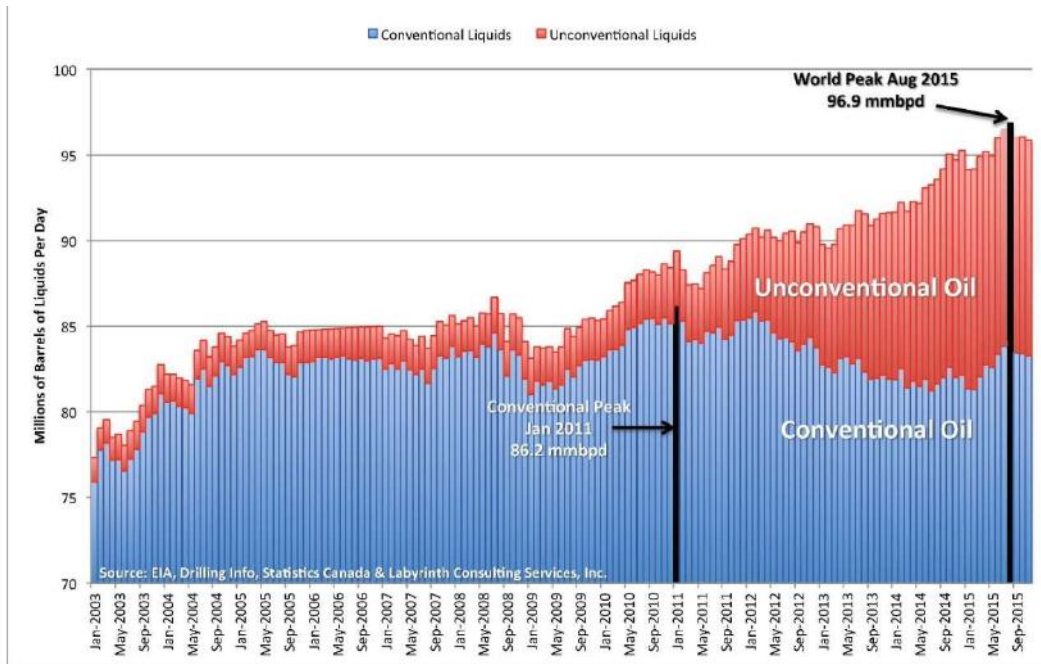


Figure 2-2: World conventional and unconventional liquid production (EIA, Drilling Info, Statistics Canada and Labyrinth Consulting Services, Inc.)

Novelty

As mentioned in the literature review, some works used PBE to simulate the electrocoalescence of water droplets in crude oil. The fluid dynamics models considered in these works to describe the flow of the dispersed phase are still very simple. Other works considered the dispersed phase as a continuous phase, in order to solve the problem with two-phase flow simulations. These approaches do not seem appropriate to depict the process. Therefore, the CFD-PBE coupling was used for the first time to simulate the electrocoalescence desalination process. A wide range of model emulsions was used in experiments to develop a relatively general predictive model. Finally, a new criterion was introduced to model the creation/segregation of the free water phase.

Nomenclature

| | |
|-----------|---|
| a_k | volume fraction of k^{th} phase |
| A | Hamaker constant |
| C | capacitance at the droplet surface |
| Ca | electrocapillary number |
| d_0 | initial distance between the inner poles (m) |
| D_d | diffusion coefficient of the dispersed phase ($\text{m}^2 \cdot \text{s}^{-1}$) |
| e_{VU} | coalescence efficiency of V and U droplets |
| E | electric field ($\text{kg} \cdot \text{m}^2 \cdot \text{s}^{-3} \cdot \text{A}^{-1} \cdot \text{m}^{-1}$) |
| F_B | buoyancy force (N) |
| F_D | drag force (N) |
| F_{dip} | dipole force (N) |
| F_g | gravitational force (N) |
| F_L | lift force (N) |
| F_p | pressure force (N) |
| F_{VM} | virtual mass force (N) |
| g | gravitational acceleration ($\text{m} \cdot \text{s}^{-2}$) |
| G | droplet growth |
| h | distance between the surfaces of two droplets (thickness) |
| L | length (m) |
| K_B | Boltzmann constant |
| m_p | mass of particle (kg) |
| n | number density of droplets per volume of emulsion ($1 \cdot \text{m}^{-3} \text{ m}^{-3}$) |
| r | droplet radius (m) |
| Re | Reynolds number |
| P | pressure ($\text{N} \cdot \text{m}^{-2}$) |
| Pe | Peclet number |
| P_{dip} | dipole moment of the bonds |

| | |
|----------|--|
| S | spacing between the center of two droplets (m) |
| S | source term in population balance equation |
| t | time (t) |
| T | temperature (K) |
| V | volume (m ³) |
| v | characteristics of the size of droplets |
| v_f | volume fraction |
| u | velocity (m/s) |
| u_{vU} | relative velocity between V and U droplets |
| Z | special position (m) |

Greek symbols

| | |
|--------------|---|
| ϵ_m | permittivity of medium (F. m ⁻¹) |
| μ | viscosity (kg·m ⁻¹ ·s ⁻¹) |
| ρ | density (kg·m ⁻³) |
| μ | viscosity (kg·m ⁻¹ ·s ⁻¹) |
| γ | interfacial tension (N·M ⁻¹) |
| $Q(v, v')$ | coalescence kernel between v and v' droplets |
| τ | viscous stress tensor |
| Φ | voltage at the droplet surface |
| λ | ratio of the radius of the small drop to that of the large drop |

Subscripts and superscripts

| | |
|--------|-------------------------------------|
| C | continuous phase |
| ch | characteristics of electrocoalescer |
| $crit$ | critical |
| d | droplet phase (water) |
| O | oil phase (continuous phase) |
| W | water phase (dispersed phase) |

Chapter 3 – Methodology

During the process of oil production, the mixture of water and oil is subjected to large shear rates, generating W/O emulsions [144–147] with large salt contents. Electrostatic demulsification of W/O emulsions is largely applied in the oil industry to desalt crude oil prior to its refining [3,47,148]. Droplet sizes and salt concentration are key variables in defining the separation efficiency [144–147].

The emulsion flow is a polydisperse multiphase flow that can be simulated by coupling a population balance model [82] with computational fluid dynamics [108,112,129,134]. The accuracy of this approach heavily relies on the adequacy of the employed breakage and coalescence models, which are not generally applicable and have adjusted parameters that usually depend on the characteristics of the multiphase system [45,115,116]. The parameters of the breakage and coalescence models are determined using available experimental data.

The CFD-PBE coupling builds the principal structure of this work. The schematic diagram of the methodology that was proceeded in this work is depicted in [Figure 3-1](#). As explained in [Section 2.2](#), the only interdroplet phenomenon that is considered to happen in electrocoalescence is aggregation. In this study, the coalescence of water droplets was shown through the PBE and the creation/segregation of free phase was displayed by the capture term. Moreover, the Navier-Stokes equation was solved to predict the motion of the phases (e.g. sedimentation). The polydisperse Eulerian-Eulerian model [95] was chosen for the fluid dynamics of the problem. The model considers the motion of multiple dispersed phases and one continuous phase. Besides the quadrature method of moments (QMOM) [134] was used to solve the PBE.

The aggregation and capture kernels have parameters that should be estimated using experimental data. In this work, the results of batch electrocoalescence experiments for aqueous and saline W/O emulsions were used to estimate the parameters. The reason is the less complicated nature of the batch electrocoalescence compared to the continuous process. The idea is to increase the precision and facility of parameter estimation. A mono-variate PBM based on mass/momentum balance equations for oil, dispersed and free water phases was developed to predict the behavior of batch electrocoalescence process. The details of batch experiments and PBM are presented in [Sections 3.1 and 3.2](#), respectively.

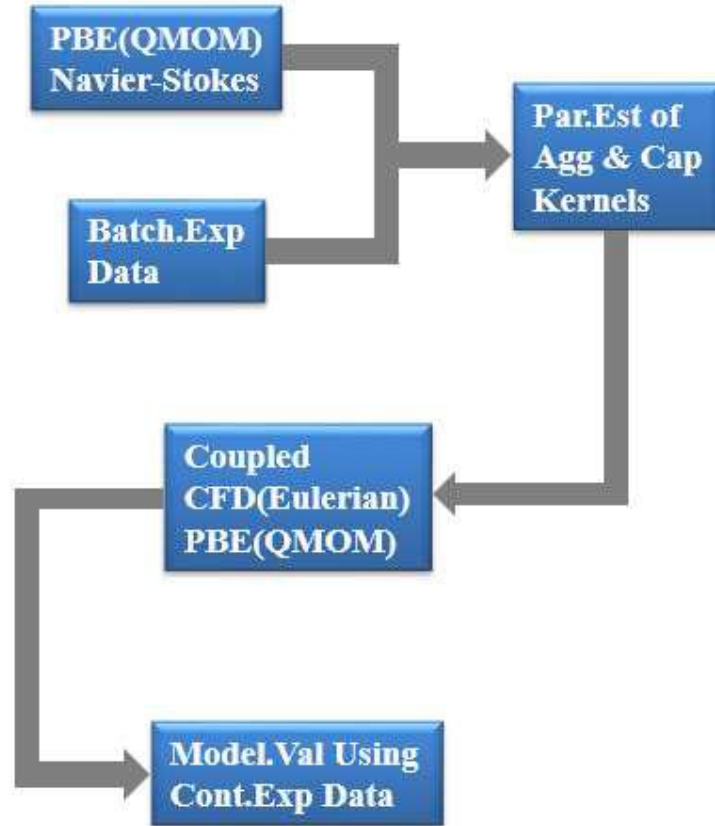


Figure 3-1: Schematic Diagram for the Methodology

After estimating the parameters, the aggregation and capture kernels were used to develop the CFD-PBE simulations. In this work, the Ansys Fluent (R) software [96] was used to perform the simulations. Moreover, the Ansys Fluent's (R) user-defined function (UDF) options were used to implement the PBM. The results of CFD-PBE model were validated using experimental data from a continuous electrostatic pilot plant. The details of continuous pilot plant experiments and PBM are presented in [Sections 3.3 and 3.4](#), respectively. A more detailed description of these steps is presented in the following sections.

3.1. Description of Batch Experiments

In this section, the details of batch experiments are explained. It should mention that the experiments were performed with the collaboration of MSc. Débora Micheline Vaz de Miranda (deboramichelline@gmail.com / dmiranda@peq.coppe.ufrj.br).

3.1.1. Basis of the Experiments

The objective of the experiments was to study the influence of the electric field on the demulsification of model water-in-crude-oil emulsion. The advantage of using model emulsion is that it makes possible to have precise knowledge about the ingredients of the emulsion. However, the synthesized W/O emulsion should have a good representation of water-in-crude oil emulsion.

In this work, the Exxsol D130 (ExxonMobil) was used to perform the experiments. Exxsol D130 is a petroleum-based low odor hydrocarbon solvent. The desirable qualities of Exxsol D130 are the low aroma, low toxicity levels and narrow boiling point (Exxsol D130 MSDS, PureChems). The characteristics of the Exxsol D130 are presented in [Table 3-1](#).

Table 3-1: Characteristics of Exxsol D130

| | |
|---|-------|
| Density (g.cm ⁻³) 25°C (SVM 3000 Viscometer, Anton Paar) | 0.825 |
| Kinematic viscosity (mm ² /s) 25°C (SVM 3000 Viscometer, Anton Paar) | 7.81 |
| Dynamic viscosity (mPa.s) 25°C (SVM 3000 Viscometer, Anton Paar) | 6.45 |
| Interfacial tension (mN/m) (Tensiometer DSA100, Kruss) | 42.54 |
| Conductivity (nS/m) (CG 2000 conductometer, Gehaka) | - |
| Total acidity index (mgKOH/g) (Potentiometric titrator, Metrohm) | 0.219 |
| Refraction index (Abbemat 3X00 Refractometer, Anton Paar) | 1.45 |

To prepare the W/O emulsion, the desired mass percent of deionized (pH=6.5) water/saline was mixed with the Exxsol D130. Besides, to represent the natural materials of crude oil (e.x. asphaltenes and resins) in the W/O emulsion, chemical emulsifier was added to the respective phases. In this work, the hydrophilic AOT (Sigma-Aldrich) and lipophilic Span 80 (Sigma-Aldrich) emulsifiers were used to generate the emulsion.

To examine whether the synthesized W/O emulsion has a proper representation of water-in-crude oil emulsion, the stability and droplet size distribution (DSD) of the samples were analyzed [149]. The stability of the model emulsion was evaluated by observing the separation between the phases reported by Turbiscan equipment (TURBISCAN LAB™ Expert). To perform the stability analysis, the emulsion was poured into a 30mL cylindrical glass cuvette. Turbiscan emits an infrared beam ($\lambda = 880$ nm) over the height of the cuvette. The equipment has two synchronized optical scanners

which measure the transmitted and reflected lights from different elevations of the emulsion. The apparatus presents the percentage of transmitted/reflected lights versus the height of the emulsion over time. In this study, since the W/O emulsion was opaque and did not have any transmission, only the reflected light was evaluated (backscattering).

The DSD of the W/O emulsion was measured by analyzing the images obtained from the Axiovert MRc40 MAT inverted optical microscope (Carl Zeiss). Samples were ejected from the model emulsion and put on lame to capture microscopic images. Five photos were captured from each microscope slide to consider the dispersion effects in the emulsion. The ImageJ analyzer (National Institutes of Health) was used to determine the DSD of the emulsion. The preparation of the emulsion, the stability/DSD analysis, and execution of the experiments were performed at room temperature (25 °C).

3.1.2. Experimental Setup

The experiments were performed in a batch electrostatic system. The main components of the experimental setup: a high voltage power source, batch vessel, and two electrodes are shown in [Figure 3-2](#). The Trek PD06035 power amplifier (Tecnoclade Systems) generates controlled voltage waveforms. The capacity of the amplifier is limited to the AC voltage of ± 30 kV, the electrical current of ± 40 mA, and power of 600 W.



[Figure 3-2](#): Setup of the batch electrostatic system: (a) high voltage power source (b) electrodes and (c) batch vessel

The electrostatic vessel is a jacketed glass vial which is connected to a thermostatic bath to control its temperature. The square shape electrodes are made of stainless steel. The

length of the electrodes is 2.5 cm and the distance between them is 2.8 cm. One of the electrodes is connected to the amplification system while the other one is ground. There is also a small ground electrode at the bottom of the vessel to zero the electrical voltage of the emulsion. The exact dimensions of the batch vessel and electrodes are shown in **Figure 3-3**. A computer program based on the LabVIEW programming language (National Instruments) was used to set the desired voltage, frequency, waveform of the applied electric field between the electrodes.

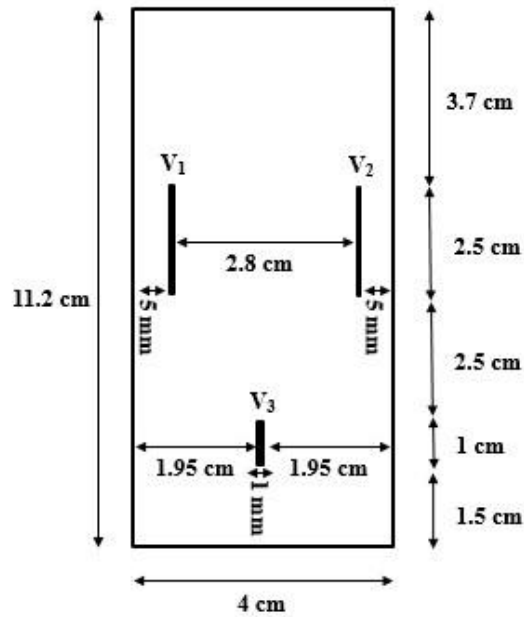


Figure 3-3: Dimensions of the batch electrostatic vessel

3.1.3. Experimental Procedure

The procedure to prepare the samples of W/O emulsion and execute the experiments was as follows:

1. The 0.2% w/w of AOT and 0.3% w/w of span 80 surfactants were pre-added to the aqueous and oil phases, respectively;

For the preparation of saline emulsion, the 3.5% w/w of Sodium Chloride: NaCl salt (Vetec Química Fina LTDA) was added to the aqueous phase prior to step 1.

2. The desired mass of the aqueous solution (0.2% AOT) was heated to 29 °C, and then gradually poured into the oil phase;

Regarding to this step of the experiment, it should consider that the emulsion which is

prepared by pouring the oil phase to the aqueous solution could be more stable [150].

3. The mixture was homogenized under vigorous stirring of an Ultra-Turrax dispersing system (Polytron PT3100, Biovera) for 5 minutes with the rotational speed of 7000rpm;

4. The initial DSD of the emulsion was determined by analyzing the microscopic images of the emulsion using the ImageJ software (National Institutes of Health);

5. A 30 mL of the emulsion was poured into the cylindrical glass cuvette to perform the stability analysis in the Turbiscan;

6. A 180 mL of the emulsion was poured into the electrostatic vessel, allowing the electrostatic treatment to begin;

7. The treated emulsions were analyzed to study the effect of electric field on the breakage of the W/O emulsions.

To study the effect of electric field on the W/O emulsions, samples were taken from three different elevations of the electrostatic vessel as schematically shown in [Figure 3-4-a](#) (P₁, P₂, P₃). Similarly, to examine the stability of the emulsions, samples were taken from three different elevations of the Turbiscan's cuvette as schematically shown in [Figure 3-4-b](#) (P₁, P₂, P₃). To compare the efficiency of electrocoalescence, the selection of sampling points (P₁, P₂, P₃) on the Electrostatic vessel and Turbiscan's cuvette were proportional. The water content and DSD of the ejected samples were analyzed to investigate the coalescence and sedimentation of water droplets under the effect of the electric field. The water content of the samples was measured by the volumetric titration Karl Fischer (KF Titrando 836, Metrohm). Also, the DSD of the samples was determined by analyzing the microscopic images as explained in [Section 3.1.1](#).

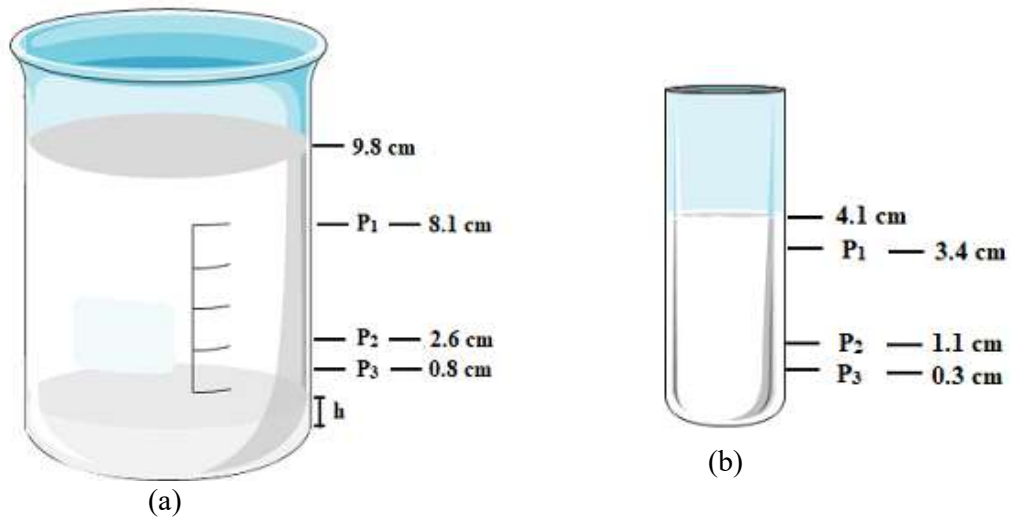


Figure 3-4: Schematic sampling points of the (a) electrostatic vessel (b) Turbiscan's cuvette

It should be mentioned that to take samples from the treated emulsion, the electrodes were removed. This causes a small decrease in the height of the emulsion in the vessel which is schematically shown in Figure 3-5.

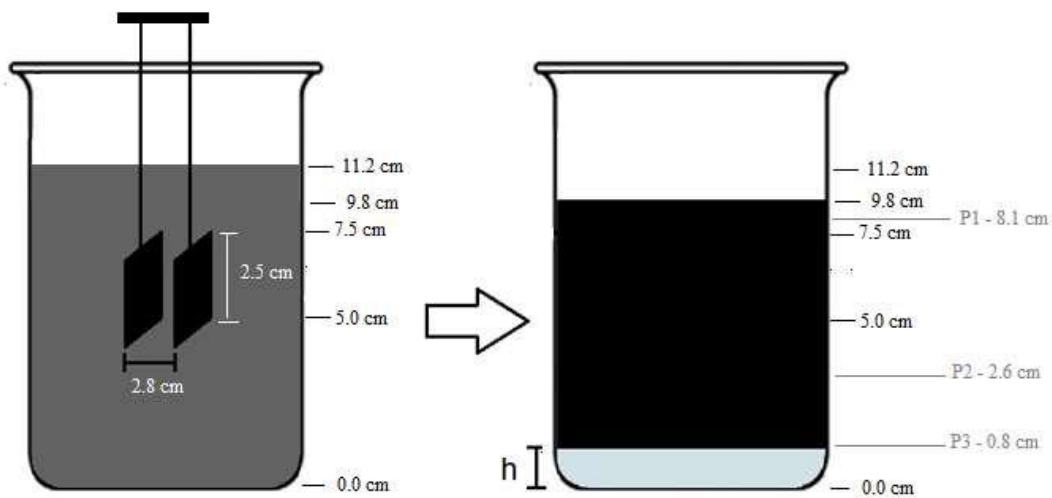


Figure 3-5: Displacement of the vessel's height by removing the electrodes

3.1.4. Experimental Conditions

The objective of the experiments was to evaluate the influence of the following variables on the demulsification of the W/O emulsion:

- a) Initial water content
- b) Electrical potential
- c) Electrostatic time

Therefore, W/O emulsions with different initial water contents were prepared and put under the effect of different electrostatic intensities for different residence times. The half-factorial experimental design based on two levels with a triplicate at the central point was used to perform the experiment. Table 3-2 shows the matrix of experimental design in terms of the normalized variables (-1, 0, 1). The values of the respective experimental variables are presented in Table 3-3.

Table 3-2: Experimental design

| Run | Initial Water Content (%) | Electrical Potential (kV) | Time (min) |
|-----|---------------------------|---------------------------|------------|
| 1 | 1 | 1 | 1 |
| 7 | 1 | 1 | -1 |
| 6 | 1 | -1 | 1 |
| 9 | 1 | -1 | -1 |
| 2 | -1 | -1 | -1 |
| 10 | -1 | 1 | -1 |
| 3 | -1 | 1 | 1 |
| 4 | -1 | -1 | 1 |
| 5 | 0 | 0 | 0 |
| 8 | 0 | 0 | 0 |
| 11 | 0 | 0 | 0 |

Table 3-3: Values of experimental variables

| Input variable | Lower value (-1) | Central value (0) | Upper value (+1) |
|---------------------------|------------------|-------------------|------------------|
| Initial Water Content (%) | 5 | 10 | 15 |
| Electrical potential (kV) | 4 | 6 | 8 |
| Time (min) | 4 | 7 | 10 |

3.2. Mathematical Model for Batch Electrocoalescence Process

3.2.1. Simplified Model for Experimental Analysis

A dynamic population balance model was developed to analyze the coalescence of water droplets in the batch electrocoalescence process. In the electrostatic vessel, the coalescence of droplets is so dominant that they form a free phase. To address the creation of the free water phase, a source term called “capture” was added to the balance equations. PBE, in general, is proposed for dilute systems and it is valid as long as the droplets are available. Therefore, we believe that in systems in which the coalescence is so dominant that a new free phase is created, a new term should be considered in the PBE to address this phenomenon. To our knowledge, this is the first work where the “free phase” idea has been used to model the electrocoalescence process. The schematic of a W/O emulsion combined with free water phase is shown in [Figure 3-6](#).

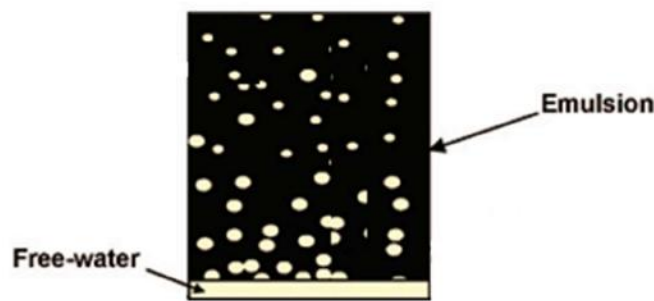


[Figure 3-6](#): Schematic of w/o emulsion combined with the sedimented water phase.

During the experiments, samples were taken from three different points of the vessel ([Figure 3-4](#)) to examine the uniformity of the emulsion in the treaters. Based on the findings of the experiments, the profiles of size distribution and water content were not uniform inside the emulsion. Therefore, the convection term was maintained in the balance equations to address the axial gradients of the variables. Moreover, it was considered that the free water phase is created gradually along the height of the treaters. To consider the movement of the phases, the mass and momentum balance equations of oil, disperse and free-water phases were coupled to the PBE. The schematic of the aqueous phases available in the treaters (water droplets and free-water) is shown in [Figure 3-7](#). In this work, the radial gradients were neglected and a one-dimensional model was used to represent the batch process. However, it should mention that because of the

vertical electrodes, the water phases tend to move horizontally toward the direction of the electric field. This can be utilized as an idea to improve the model in the future works.

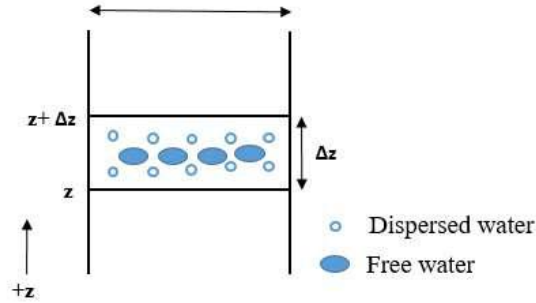


Figure 3-7: Schematic of the water phases present in the treater

To model this system, three phases denoted as I, II, and III were considered to be present in the treater. Phase I comprises the oil phase, while phases II and III include the dispersed droplets and free water, respectively. The PBE along with mass and momentum balance equations for oil, disperse and free water phases were solved simultaneously to predict the behavior of the batch electrocoalescence process. Mass and momentum balance equations of the phases were written for the sectional element shown in **Figure 3-7** to determine the governing equations of the entire system. In the following sections, the conservation equations for each of the three phases are explained separately.

- Mass balance equation for the oil phase:

$$\frac{\partial \phi^I}{\partial t} + \frac{\partial}{\partial z}(u^I \phi^I) = 0 \quad (3-1)$$

- Momentum balance (Navier-Stokes) equation for the oil phase:

$$\begin{aligned} \frac{\partial \phi^I u^I}{\partial t} + u^I \frac{\partial}{\partial z}(\phi^I u^I) + \frac{\phi^I}{\rho_o} \left(\frac{\partial P}{\partial z} \right) + \phi^I g \\ + \frac{C_D^{III} \phi^{III} \phi^I}{\rho_o} (u^I - u^{III}) + \sum_{d=1}^M \frac{C_{D_d} \phi_d \phi^I}{\rho_o} (u^I - u_d) = 0 \end{aligned} \quad (3-2)$$

In these two equations, ϕ^I and u^I are the volume fraction and rising velocity of the oil phase, respectively. The last two terms on the left-hand side of **Equation (3-2)** represents

the drag force which is due to the relative motion of oil to the aqueous phases. In the similar studies presented to simulate the movement of water-in-oil emulsion [151], the model proposed by Shiller was used to calculate the drag coefficient [96,152].

$$C_{D_0} = \frac{18f_{drag}\mu_{sys}}{d^2} \quad (3-3)$$

This model caters for dilute systems where the volume fraction of disperse phases is low [153]. The model is obtained from simple analysis, where the forces are exerted on single elements of disperse phase. However, when the volume fraction of droplets increases, these forces are influenced by the vicinity of other disperse phases. Therefore, in this work, the pre-factor correlation employed by Marschall [154] and reactingEulerFoam OpenFOAM solver (OpenCFD Ltd., 2013) for laminar flow based on the study of Richardson [139] was used to determine the drag coefficient:

$$C_D = \frac{1}{(1-\varphi_w)^{4.65}} C_{D_0} \quad (3-4)$$

where φ_w the is the summation of volume fraction of water phases:

$$\varphi_w = \sum_{d=1}^M \varphi_d + \varphi^{III} \quad (3-5)$$

The μ_{sys} in Equation (3-3) is the viscosity of the system which was calculated by

$$\mu_{sys} = \left(\sum_{d=1}^M \varphi_d + \varphi^I \right) \mu_o (1 + 2.5\varphi_e + 14.1\varphi_e^2) + \mu_w \varphi^{III} \quad (3-6)$$

where the volume fraction of disperse phases (φ_e) in the emulsion (oil+water droplets) is

$$\varphi_e = \frac{\sum_{d=1}^M \varphi_d}{\sum_{d=1}^M \varphi_d + \varphi^I} \quad (3-7)$$

The first term on the right-hand side of Equation (3-6) represents the viscosity of emulsion [155] and the second term characterizes the free phase. Moreover, d in Equation (3-3) is the representative diameter of disperse or free phases. In this study, it was considered that the representative diameter of free phase is proportional to the cubic root of its volume fraction:

$$d_f = d_{max}^{III} (\varphi^{III})^{1/3} \quad (3-8)$$

where d_{max}^{III} is the maximum diameter of the free water phase. In this work, the value of 500μ was used for the d_{max}^{III} . The value is basically a numerical parameter which had the best performance to model the system. Here, it was considered that the total volume of free phase is equal to the sum of the volume of equisized big droplets which compose the phase. Therefore, the representative diameter of free phase would be the cubic root of the volume fraction of free phase. In the formulation of the equations, the positive and negative directions of velocity are upwards and downwards, respectively. Since in this work, the descending and rising velocities of phases were slow ($<1e-3(m/s)$), the $(\frac{\partial P}{\partial z})$ term in the Navier-Stokes equation was considered as the static pressure drop in each sectional element (dz):

$$\frac{\partial P}{\partial z} = -g(\varphi^I \rho_O + (\varphi^{III} + \sum_{d=1}^M \varphi_d) \rho_W) \quad (3-9)$$

- Mass balance equation for the disperse water droplets (PBE):

$$\begin{aligned} \frac{\partial n}{\partial t} + \frac{\partial}{\partial z}(u_d n) + K_{cap} \varphi^{III} n - \frac{1}{2} \int_0^v n(v-v', z, t) n(v', z, t) Q(v-v', v') dv' \\ + \int_0^\infty n(v, z, t) n(v', z, t) Q(v, v') dv' = 0 \end{aligned} \quad (3-10)$$

The capture term in Equation (3-10): $K_{cap} \varphi^{III} n$ denotes the creation of free water phase.

The capture coefficient: K_{cap} is a parameter of the model and should be estimated. In this work, due to the mathematical form of the capture term (contact model), it was not possible to consider a zero value for the initial volume fraction of the free phase. Therefore, it was assumed that 0.01 of the initial water volume% is composed of the free phase. The last two terms on the left-hand side of the equation represent the birth and death aggregations of the droplets, respectively [156]. Equations (3-10) is a set of partial differential equations which should be solved for all of the classes of droplets (d). It's worth to mention that based on our calculations, in this work, the diffusion of droplets was not significant in comparison to the other terms of Equation (3-10).

- **Momentum balance (Navier-Stokes) equation for the disperse water droplets:**

$$\begin{aligned} \frac{\partial \varphi_d u_d}{\partial t} + u_d \frac{\partial}{\partial z} (\varphi_d u_d) + \frac{\varphi_d}{\rho_w} \left(\frac{\partial P}{\partial z} \right) + n g + \frac{C_{D_d} \varphi_d \varphi^I}{\rho_w} (u_d - u^I) \\ + K_{cap} \varphi^{III} \varphi_d u_d = 0 \end{aligned} \quad (3-11)$$

The last term on the left-hand side of Equation (3-11) represents the momentum transfer from the disperse phases to the free-water phase.

In this work, similar to the work of Favero[151], our initial intention was to develop a bi-variate population balance model to represent the distribution of mass of salt in the droplets. However, in the electrocoalescence process, the salt is well mixed in the droplets. Therefore, the distribution of mass salt is dependent on the size of the droplets and cannot be considered as another internal variable of the PBM.

- **Mass balance equation for the free water phase:**

$$\frac{\partial \varphi^{III}}{\partial t} + \frac{\partial}{\partial z} (u^{III} \varphi^{III}) - \sum_{d=1}^M K_{cap} \varphi^{III} \varphi_d = 0 \quad (3-12)$$

In this equation, φ^{III} and u^{III} are the volume fraction and descending velocity of the free water phase, respectively. The last term on the left-hand side of the equation represents the creation of the free water phase due to segregation of the droplets from the disperse phase.

- **Momentum balance (Navier-Stokes) equation for the free water phase:**

$$\begin{aligned} \frac{\partial \varphi^{III} u^{III}}{\partial t} + u^{III} \frac{\partial}{\partial z} (\varphi^{III} u^{III}) + \frac{\varphi^{III}}{\rho_w} \left(\frac{\partial P}{\partial z} \right) + \varphi^{III} g + \frac{C_{D_D} \varphi^{III} \varphi^I}{\rho_w} (u^{III} - u^I) \\ - \sum_{d=1}^M K_{cap} \varphi^{III} \varphi_d u_d = 0 \end{aligned} \quad (3-13)$$

The last term on the left-hand side of the equation represents the momentum transfer from the classes of droplets (d) to the free-water phase.

3.2.2. Coalescence and Capture Kernels

In this work, the model proposed by Zhang [84] was used to calculate the aggregation frequency of the two droplets “*i*” and “*j*” coalescing together:

$$Q(d_i, d_j) = K_{agg} \pi (d_i + d_j)^2 u_{ij}^{(0)} e_{ij} \quad (3-14)$$

In this equation, $u_{ij}^{(0)}$ is the relative velocity of two widely separated droplets approaching together [37,157]:

$$u_{ij}^{(0)} = \frac{2(\hat{\mu}+1)|\rho_w - \rho_o|d_i^2(1-\lambda^2)g}{3(3\hat{\mu}+2)\mu_o} \quad (3-15)$$

Moreover, e_{ij} is the collision efficiency which represents the influences of the electric field, hydrodynamic interactions between the phases, and Van der Waals forces on the coalescence of the droplets [84]:

$$e_{ij} = 0.45 \left(\frac{2\lambda|\rho_w - \rho_o|(1-\lambda)gd_i}{3\epsilon(1+\lambda)^2 E_0^2} \right)^{-0.55} \quad (3-16)$$

and K_{agg} is a parameter of the aggregation kernel which is dependent on the characteristics of the particulate system and should be estimated.

In this study, based on the primary results of the electrostatic and Turbiscan tests, it was considered that the gravitational coalescence is negligible compared to the electrocoalescence. In this work, the ComSol Multiphysics software (COMSOL Inc) was used to determine the profile of a steady-state electric field (DC) inside the batch electrostatic vessel. The ComSol simulations were conducted for the two-dimensional geometry of **Figure 3-3**. It's worth to mention that based on the electric field's equation ($E = -\nabla \phi$) [158], the profile of the DC electric field inside the vessel is independent on the local volume fraction of the water/oil. Moreover, it should mention that in this work the power source (**Figure 3-2**) was able to maintain the voltage at the desired values (**Table 3-3**). In the electrostatic vessel, the free phase is initially mainly created in the space between the electrodes where the electric field is stronger and then, it descends and captures other water droplets. Therefore, it was expected that the capture coefficient would have different values in different elevations of the vessel. In this work, the following empirical equation was considered/proposed to calculate the capture

coefficient:

$$K_{cap} = (K_{cap_0} + K_{cap_E} E_0)(\varphi^{III})^{-1/3} d_d^2 \quad (3-17)$$

In this equation, E_0 is the electric field and K_{cap_0} , K_{cap_E} are two parameters of the model which should be estimated using the experimental data. The $(\varphi^{III})^{-1/3}$ term represents the area per volume of the free water droplets and the d_d^2 is proportional to the area of the disperse droplets. Based on the formulation of the capture coefficient, we believe that the capture phenomenon in the electrocoalescence is based on shock rather than diffusion. The mathematical form of Equation (3-17) suggests that the bigger droplets have a higher chance to be captured by the free phase.

3.2.3. Solution of the Mathematical Model

In the previous section, the governing equations of the particulate system were derived. The set of integrodifferential Equations (3-1), (3-2), (3-10), (3-11), and (3-13) should be solved to determine the profiles of DSD and water content inside the batch electrostatic vessel. In this work, our initial intention was to use the method of classes [159] to resolve the integral form of Equation (3-10) and solve the PBE. The idea was taken from the work of Mitre [89] which was performed to model the breakage/coalescence for the flow of W/O emulsion through a valve-like element. In their study, they considered that the 100 classes of droplets move with the continuous phase velocity. However, one of the main characteristics of batch electrocoalescence is the countercurrent movement of the phases which demands the solving of Navier-stokes equation. Therefore, in this work, due to the high computational cost of the mass-momentum balance equations for an adequate number of classes (e.x. 50), it was not possible to employ the method of classes [159]. Moreover, the mathematical form of Navier-Stokes equation for disperse droplets (Equation (3-11)) requires non-zero initial number density values which complicate the utilization of fixed mesh PBE solution methods. Therefore, we decided to use moment-based methods because of their computational efficiency [160].

In this study, our second intention to solve the PBE was to employ the direct quadrature method of moments (DQMOM) [129]. However, our simulations showed that the method diverges as the volume fraction of one of the disperse droplets reaches to zero. This is due to the characteristics of transport equations of DQMOM as it diverges when

one of the disperse phases vanishes. This issue is addressed in the 4th and 7th chapter of Marchisio's book [161]. Therefore, we employed the quadrature method of moments (QMOM) (D L Marchisio and Fox 2005) to solve the PBE. The main difference between the QMOM and DQMOM is that the QMOM considers a single velocity for all classes of droplets while DQMOM considers different velocities for different classes of droplets [160,162]. In the QMOM approach, the number density function is thought of a summation of Dirac delta functions:

$$f(\xi; z, t) = \sum_{d=1}^M w_d(z, t) \delta(\xi - \xi_d(z, t)) \quad (3-18)$$

where the subscript d node represents the M disperse phases characterized by weight $w_d(z, t)$ and property $\xi_d(z, t)$. In this study, similar to the Ansys Fluent (R) software's add-on for PBE [96], it was considered that the droplets are represented by four classes ($M = 4$) of disperse phases. Here the diameter of the class of droplets (d_d) was considered as the internal property of the PBE. To apply the QMOM, the PBE (Equation (3-10)) must be rewritten in terms of moments of number density function which can be approximated using the quadrature [160]:

$$m_k(t) = \int_0^\infty f(d; z, t) d^k \approx \sum_{d=1}^M w_d d_d^k \quad (3-19)$$

By substituting Equation (3-18) in Equation (3-10) and applying the moment transforms, the following closed set of transport equations can be obtained [160]:

$$\begin{aligned} \frac{\partial m_k}{\partial t} + \frac{\partial}{\partial z} (u^H m_k) + K_{cap} \varphi^{III} m_k - \frac{I}{2} \sum_{\alpha=1}^M \sum_{\gamma=1}^M (\langle d \rangle_\alpha^3 + \langle d \rangle_\gamma^3)^{k/3} Q_{\alpha\gamma} w_\alpha w_\gamma \\ + \sum_{\alpha=1}^M \sum_{\gamma=1}^M \langle d \rangle_\alpha^k Q_{\alpha\gamma} w_\alpha w_\gamma = 0 \end{aligned} \quad (3-20)$$

Equation (3-20) should be solved for the first $2M$ moments (m_k) ($k = 0, \dots, 2M - 1$). In each step of integration, the weights (w_d) and abscissas (d_d) are determined by inverting the moments. In this work, the ζ_k -Wheeler algorithm [163] was used for the moment inversion. In this procedure, first, the number of realizable moments is determined by calculating the values of ζ_k :

$$\zeta_k = \frac{H_{k+1}H_{k-2}}{H_k H_{k-1}} \quad k = 0, 1, \dots, 2M - 2 \quad (3-21)$$

where H_k are the Hankel determinants [164]

$$H_{2k} = \begin{vmatrix} M_0 & \cdots & M_k \\ \vdots & & \vdots \\ M_k & \cdots & M_{2k} \end{vmatrix} \quad (3-22)$$

$$H_{2k+1} = \begin{vmatrix} M_1 & \cdots & M_{k+1} \\ \vdots & & \vdots \\ M_{k+1} & \cdots & M_{2k+1} \end{vmatrix}$$

with $H_{-2}=H_{-1}=H_0=1$. Based on the largest value of k for which $\zeta_k > 0$, the subset of realizable moments is identified [165]. Then, the Wheeler algorithm [166] is used to invert the realizable moments.

In order to improve the convergence and conservativeness of the system of equations, the mass balance equation of oil phase (Equation (3-1)) was substituted by the algebraic equation of the total volume of the phases:

$$\phi^I + \phi^{II} + \phi^{III} - 1 = 0 \quad (3-23)$$

where ϕ^{II} is the total volume fraction of disperse water droplets. Based on the definition of quadrature moments (Equations (3-19)), the total volume fraction of disperse droplets can be calculated as $\frac{\pi}{6} m_3$:

$$\phi^{II} = \sum_{d=1}^M \phi_d = \sum_{d=1}^M w_d \frac{\pi}{6} d^3 = \frac{\pi}{6} m_3 \quad (3-24)$$

Moreover, due to the batch characteristic of the electrostatic vessel, the average velocity of the system is zero:

$$u_{\text{sys}} = u^I \phi^I + u^{II} \phi^{II} + u^{III} \phi^{III} = 0 \quad (3-25)$$

Therefore, by determining the velocities of disperse and free water phases from Equations (3-11) and (3-13), the rising velocity of the oil phase can be calculated by Equation (3-25).

The independent variables of the resulting set of equations are the elevation and time

(z, t) , while the $2M$ first moments of classes of droplets (m_k); volume fraction of phases I and III (ϕ^I, ϕ^{III}), rising velocity of oil phase (u^I), and descending velocities of disperse and free-water phases (u^{II}, u^{III}) comprise the dependent variables.

The set of partial-differential-algebraic Equations (3-11), (3-12), (3-13), (3-20), (3-23), and (3-25) were expanded and solved using the finite volume method. The linear upwind scheme was used to estimate the gradient terms. For this reason, the height of the electrostatic vessel was discretized uniformly to 56 points. Uniform distribution of DSD and water content inside the vessel was considered as the initial condition. Moreover, it was considered that the initial velocity of the phases is zero. Besides, zero-fluxes at the upper and lower walls of the vessel were considered as the boundary condition. The numerical integrators of Dasslc [167] and ode15s (MathWorks) were used to solve the set of differential-algebraic equations.

3.2.4. Determination of the Initial DSD

As explained in the previous sections, in this work, the ImageJ Analyzer (National Institutes of Health) was used to determine the DSD. The ImageJ software provides only the droplets' size (diameter) of the selected sample. In this study, approximately 2000 droplets were counted by ImageJ software for each photo analysis. The sizes measured by ImageJ Analyzer comprise the initial normalized DSD. Therefore, to determine the non-normalized DSD, the volume fraction of water (ϕ_w) was divided into the volume fraction of the droplets measured by ImageJ Analyzer as

$$N_T = \frac{\phi_w}{\sum_{j=1}^{N_c} \frac{\pi}{6} d_j^3} \quad (3-26)$$

Then, the first $2M$ initial moments ($k = 0, 1, \dots, 2M-1$) of the number of classes for the QMOM formulation (Equation (3-20)) [160] were calculated by

$$m_{k_0} = N_T \sum_j d_j^k \quad (3-27)$$

3.2.5. Estimation of Model Parameters

In this work, the values of water content ($BS&W$) at the three sampling points (P1, P2, P3 in [Figure 3-4](#)) were used for parameter estimation; and the size distribution of the droplets was used for model verification. Based on the formulation of the model, the $BS&W$ can be calculated by

$$BS\&W = \frac{\left(\sum_{d=1}^M \varphi_d + \varphi^{III}\right)\rho_W}{\varphi^I \rho_O + \left(\sum_{d=1}^M \varphi_d + \varphi^{III}\right)\rho_W} \quad (3-28)$$

The objective function that was used to estimate the parameters of the model (K_{agg} , K_{cap0} , K_{capE}) is

$$Obj_F = \sqrt{\frac{1}{3N_E} \sum_{p=1}^{N_E} \sum_{h=1}^3 (BS\&W_{exp,p,h} - BS\&W_{cal,p,h})^2} \quad (3-29)$$

where N_E is the number of experimental points, the subscript h refers to the elevation of the sampling point and the subscript p indicates the points of the experimental matrix.

In this work, the Asynchronous and Immediate Update Parallel Particle Swarm Optimization (AIU-PPSO) algorithm developed by [Moraes \[168\]](#) was employed to determine the parameter of the model. The computer programs were written using the Matlab 2010 ([Mathworks](#)) software and were run on a 32G RAM, SSD 1Tb, quad-core i7, and 3.4GH machine.

3.3. Description of Continuous Pilot Plant Experiments

The accuracy of the aggregation and capture kernels developed in the previous section to simulate the electrocoalescence process is tested in this step. The kernels should be able to at least to some extent predict the dynamics of the continuous electrocoalescence pilot plant process. In the following subsections, a brief introduction to the electrocoalescence pilot plant that is used to perform the continuous experiments is presented. Further details about the procedure the continuous pilot plant experiments were performed and the setup can be found in the works of [Assenheimer \[169,170\]](#).

3.3.1. Pilot Plant

The setup of the Pilot plant is shown in **Figure 3-8**. The setup mainly consists of two sections. The first one is the emulsion generator (using a homogenizer). In this section, model oil and water are mixed and heated to make the desired emulsion. The second section is the electrostatic unit. In this section, the emulsion is broken/separated under the effect of electric field. The dehydrated oil finally is cooled down for disposal. The process description of the pilot plant is explained in the following section.



Figure 3-8. Electrocoalescence pilot plant

3.3.2. Description of Pilot Plant Process

The pilot plant process starts from two tanks, one for water (T-01) and the other one for oil (T-02). Two piston pumps (high-pressure dosing pump, Omel) are employed to flow the water (P-01) and the oil (P-02) through the process. The water feed line is equipped with one Coriolis (Micro Motion, Emerson) flowmeter (FIT-01) to measure the water mass flow rate, and where the water and oil pipes join there is another Coriolis flowmeter (FIT-02) to measure the total mass flow rate (oil and water). Two heat exchangers are connected to heat up the water (H-01) and the oil (H-02). Then, with the aid of a dynamic mixer (MP-01), the emulsion can be formed. The rotation frequency of the dynamic mixer can be altered to apply the proper shear rate to the fluids. After the formation of emulsion, there is a sampler (SP-01) where the emulsion sample can be taken to check the characteristic of the emulsion, e.g., water content by Karl Fisher titration and the average droplet size by microscopy. The emulsion then flows through the electrostatic treatment cell (INTERAV), (DC-01). The cell has thermocouples located in the bottom and top of

the cell to monitor the temperature and the water level is controlled by a needle valve in the bottom of the cell.

After the electrostatic treatment cell, the dehydrated oil flows to another sampler, (SP-02), where the treated oil samples are collected periodically (every 15 to 30 min, depends on the flow rate) from the top of the unit. The water fraction is measured by the Karl Fisher method until a steady state is reached (until the absolute error of the water content in the treated oil reaches a value lower than 5%). The last water content value is reported for each condition. The average droplet sizes are also measured and analyzed by microscopy using the ImageJ software. In the case of working at high temperature, a heat exchanger (H-03) is available to cool down the fluids before disposal. There is a control valve at the exit line of the pilot plant to regulate the system pressure (PIC-01). **Figure 3-9** shows the process flow diagram of the pilot plant.

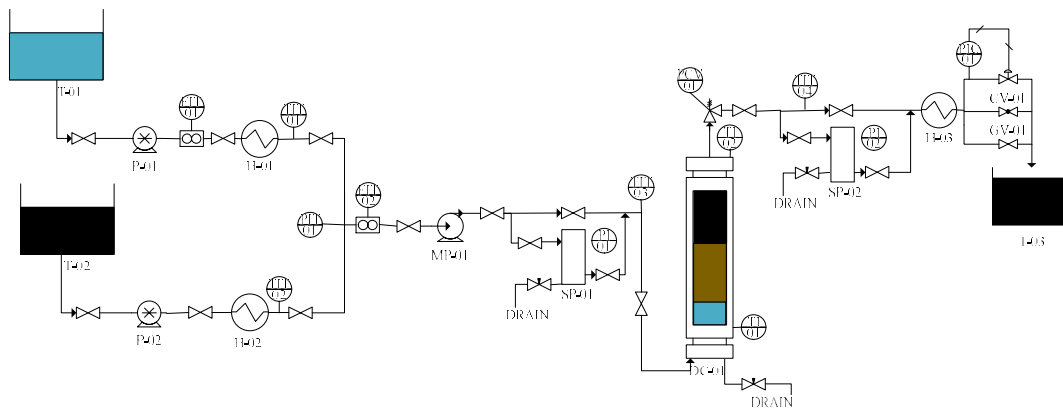


Figure 3-9. Pilot Plant Process Flow Diagram

The model that is considered to simulate the behavior of the continuous process, takes the data from the entrance to the electrostatic unit as model input and tries to predict the aggregation of dispersed droplets and separation of phases. In fact, only the second section of the pilot plant will be simulated. Therefore, due to its importance, in the flowing section, the electrocoalescer unit is explained in more detail.

3.3.3. Electrocoalescer Unit

The electrostatic coalescer, manufactured by INTERAV S/A (model DC-250) is shown in **Figure 3-10**. The equipment consists of two components: electrostatic cell and power supply unit.



Figure 3-10. Electrocoalescer unit

The electrostatic window cell is composed of a stainless steel body, with the length of 40cm and internal diameter of 5cm and an approximate volume of 820 ml. The glass window is made of tempered borosilicate for the observation of the fluid flow (Figure 3-11). The pressure threshold and maximum operating temperature of the cell are 34.5 bar and 150 °C.



Figure 3-11. Tempered borosilicate glass windows

At the bottom of the cell, there is an adjustable fluid distributor which allows the entrance of fluid at any desired level below the cell electrodes. The feeder is oriented horizontally with 12 holes of 2 mm internal diameter.



Figure 3-12. Emulsion feeder

In the lower side of the cell, there is a needle valve to drain the precipitated water. The valve is connected to a coil to cool down the water to prevent the evaporation of water when the samples are at high temperature.

At the upper side of the cell, the circular horizontal electrode plates are located. The space between the electrodes can be changed from 1 to 4 inches (25 to 100mm). In the upper flange, there is a needle valve with coil condenser, a pressure relief valve which can be adjusted from 0.68 to 15.5 bar and thermocouples to measure the inlet and outlet temperatures. (Figure 3-13).

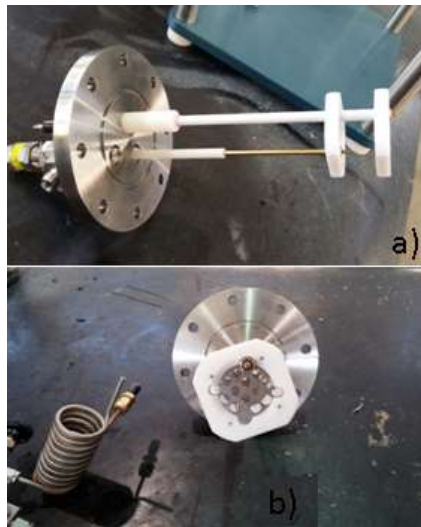


Figure 3-13. Electrodes of the electrostatic cell a) side view b) frontal view

3.4. Mathematical model for Continuous Electrocoalescence Process

In this section, the multiphase Eulerian model coupled with the QMOM population balance add-on of the Ansys Fluent (R) 17.2 software [96,171] was used to simulate the continuous electrostatic vessel. The Eulerian-QMOM model that was implemented in Ansys Fluent (R) [96,171] is similar to the batch electrocoalescence model. The aggregation and capture kernels derived in Section 3.2 were employed to implement the model.

In the following two sections, first, the Eulerian-QMOM model of Ansys Fluent (R) software is explained. Then, the detailed steps of the simulation of the continuous electrostatic vessel are presented.

3.4.1. Eulerian-QMOM Model of Ansys Fluent (R) software

The general mass/momentum conversation equations solved by Ansys Fluent (R) for the Eulerian model are presented [96]. The continuity equation for phase q is

$$\frac{\partial}{\partial t}(\varphi_q \rho_q) + \nabla \cdot (\varphi_q \rho_q \bar{\mathbf{u}}_q) = \sum_{p=1}^n (\dot{m}_{pq} - \dot{m}_{qp}) + S_q \quad (3-30)$$

where $\bar{\mathbf{v}}_q$ is the velocity of phase q and $\dot{m}_{pq} - \dot{m}_{qp}$ characterizes the net mass transfer from the p^{th} to q^{th} phase. By default, the source term S_q on the right-hand side of Equation (3-30) is zero, but it can specify a constant or user-defined mass source for each phase.

The momentum balance for phase q yields

$$\begin{aligned} \frac{\partial}{\partial t}(\varphi_q \rho_q \bar{\mathbf{u}}_q) + \nabla \cdot (\varphi_q \rho_q \bar{\mathbf{u}}_q \bar{\mathbf{u}}_q) = & -\varphi_q \nabla p + \nabla \cdot \overline{\overline{\boldsymbol{\tau}}_q} + \varphi_q \rho_q \bar{\mathbf{g}} \\ & + \sum_{p=1}^n (\bar{\mathbf{R}}_{qp} + \dot{m}_{pq} \bar{\mathbf{u}}_{pq} - \dot{m}_{qp} \bar{\mathbf{u}}_{qp}) \\ & + (\bar{\mathbf{F}}_q + \bar{\mathbf{F}}_{lift,q} + \bar{\mathbf{F}}_{wl,q} + \bar{\mathbf{F}}_{vm,q} + \bar{\mathbf{F}}_{td,q}) \end{aligned} \quad (3-31)$$

where $\overline{\overline{\boldsymbol{\tau}}_q}$ is the q^{th} phase stress-strain tensor, $\bar{\mathbf{F}}_q$ is an external body force, $\bar{\mathbf{F}}_{lift,q}$ is a lift force, $\bar{\mathbf{F}}_{wl,q}$ is a wall lubrication force, $\bar{\mathbf{F}}_{vm,q}$ is a virtual mass force, and $\bar{\mathbf{F}}_{td,q}$ is a turbulent dispersion force (in the case of turbulent flow only). $\bar{\mathbf{R}}_{qp}$ is an interaction force between phases, and p is the pressure shared between the phases. In this work, the coupled method (ANSYS 2016a) was used to solve the multiphase flow system.

In this work, the population balance add-on of Ansys Fluent (R) software [171] is used to solve the set of QMOM equations. The add-on is a set of user-defined scalars (UDS) which are solved to determine the distribution of the internal variable of a PBM for a secondary phase. The set of QMOM equations for a coalescence-breakage system in the Ansys Fluent (R) software [171] is:

$$\begin{aligned} \frac{\partial m_k}{\partial t} + \nabla \cdot (\bar{u} m_k) = & \frac{1}{2} \sum_{\alpha=1}^M \sum_{\gamma=1}^M (\langle \xi \rangle_{\alpha}^3 + \langle \xi \rangle_{\gamma}^3)^{k/3} Q_{\alpha\gamma} w_{\alpha} w_{\gamma} - \sum_{\alpha=1}^M \sum_{\gamma=1}^M \langle \xi \rangle_{\alpha}^k Q_{\alpha\gamma} w_{\alpha} w_{\gamma} \\ & + \sum_{\alpha=1}^N \bar{b}_{\alpha}^{(k)} a_{\alpha} w_{\alpha} - \sum_{\alpha=1}^N \langle \xi \rangle_{\alpha}^k a_{\alpha} w_{\alpha} \end{aligned} \quad (3-32)$$

where $\beta_{\alpha\gamma} = \beta(\langle \xi \rangle_{\alpha}, \langle \xi \rangle_{\gamma})$, $a_{\alpha} = a(\langle \xi \rangle_{\alpha})$ and

$$\bar{b}_{\alpha}^{(k)} = \int_0^{\langle \xi \rangle_{\alpha}} \xi^k b(\xi | \xi_2) d\xi \quad (3-33)$$

The procedure to solve the QMOM equations in Ansys Fluent (R) [171] is similar to what explained in Section 3.2.3. First, the moments are inverted using the PD algorithm (Gordon, 1968) to calculate the weights and abscissas. Then, the calculated values are used to integrate the $2M - 1$ moment equations (Equation (3-32)).

In order to couple the Eulerian and QMOM equations, the software uses the Sauter mean diameter: d_{32} as the representative diameter of the PBE secondary phase. Sauter mean diameter is the proportion of the 3rd to 2nd diameter-base moments:

$$d_{32} = \frac{m_3}{m_2} \quad (3-34)$$

The d_{32} represents the mean particle size and is used to calculate the drag coefficient (similar to Equation (3-3)).

3.4.2. Simulation of the Continuous Electrostatic Vessel

In this work, our initial intention was to simulate the exact 3D geometry of the electrostatic vessel (Figure 3-10). The 3D geometry of the vessel that was drawn by ANSYS SpaceClaim software [96] is shown in Figure 3-14.

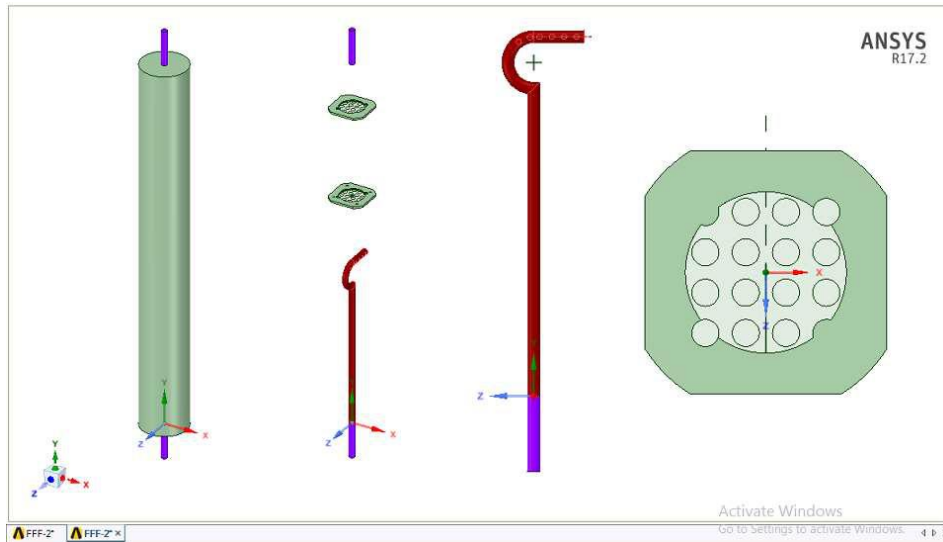


Figure 3-14: 3D geometry of the continuous electrostatic vessel

However, our initial simulations showed that the computational time of the 3D simulations is extremely high. Therefore, the 2D axisymmetric model was simulated. The exact dimensions of the continuous electrostatic vessel and electrodes are shown in Figure 3-15.

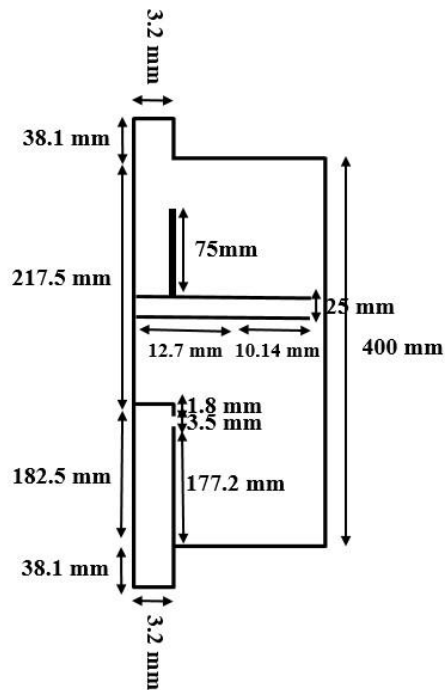


Figure 3-15: Axisymmetric dimensions of the continuous electrostatic vessel

The left side of **Figure 3-15** is the symmetry axis of the geometry. It's worth to mention that in the Ansys Fluent (R) software, the symmetry axis should be parallel to the X-axis [96]. The geometry of **Figure 3-15** consists of two incomplete rectangles which are the feeder and body of the continuous electrostatic vessel. The intersection of the two rectangles is the wall of the feeder. Besides, the outlet of the feeder is also the inlet of the body. Therefore, in order to implement the geometry in the Ansys Fluent (R) software, the two rectangles should be drawn and meshed (discretized) separately in two different files. In this work, the geometries were drawn in Ansys SpaceClaim 17.2 software and the meshes were created in the Ansys Meshing 17.2 software [96]. The feeder and body mesh files were combined together in the Ansys Fluent (R) software and the outlet of the feeder and the inlet of the body was then fused. The 2D mesh of the continuous electrostatic vessel is shown in **Figure 3-16**. Besides, the mesh repair command of the software (/mesh/repair-improve/repair) was used to improve the discretization.



Figure 3-16: 2D Axisymmetric mesh of the continuous electrostatic vessel

In this work, two meshes were used to check the convergence of the calculations. The properties of the three meshes are presented in **Table 3-4**. It is worth to mention that a third mesh with the cell length of $2.5e-4$ (m) was constructed to examine the mesh convergence. However, the Ansys Fluent (R) software was not able to initialize/solve the case of the mesh due to its high computational cost.

Table 3-4: Mesh properties used in the CFD-PBE simulations

| Mesh | Cell length (m) | Cells | Faces | Nodes |
|----------------------|-----------------|-------|--------|-------|
| 1 st Mesh | $5e-4$ | 39984 | 81323 | 41340 |
| 2 nd Mesh | $4e-4$ | 65520 | 132750 | 67231 |

As explained in **Section 3.4**, the CFD-PBE model that was implemented in the Ansys Fluent (R) software [96], is similar to the batch model described in section 3.2.1. The oil, disperse water, and free water phases were considered as the material present in the system. The interaction between the phases was presented as the drag force, lift force, mass transfer, and the surface tension force. Moreover, due to the low Reynolds number of the system ($Re < 1000$), the flow was considered laminar.

In this work, the Schiller-Nauman equation was used to calculate the drag force between the oil-disperse water and oil-free water phases [96,152]. Moreover, the DEFINE_EXCHANGE_PROPERTY user-defined function (UDF) was used to calculate the Marschall drag factor [154] explained in Section 3.2.1 (Equation (3-4)). To model the mass/momentum transfer from the disperse water phase to the free water, the DEFINE_MASS_TRANSFER UDF was employed. The function of this macro is similar to the calculation of capture term in the Equations (3-12) and (3-13).

The population balance add-on of the Ansys Fluent (R) software [96] was enabled (using the “define/models/addon-module 5” command) to model the coalescence between the disperse water droplets. The DEFINE_PB_COALESCENCE_RATE UDF was used to calculate the aggregation kernel (Equation (3-14)). Similar to the batch model, the QMOM technique with 8 moments was used to solve the population balance equation. Based on the settings of the Ansys Fluent (R) PBM, the maximum and minimum diameter of droplets were considered as 1e-3 (m) and 1e-7 (m), respectively. To calculate the capture source term in the PBE (similar to Equation (3-10)), DEFINE_SOURCE UDFs were written for each of the 8 moments. Therefore, enabling the population balance add-on for the disperse water phase, the Sauter-mean diameter was used as its representative diameter. Besides, based on the Equation (3-8), the DEFINE_PROPERTY UDF was used to calculate the representative diameter of the free water phase.

In the simulations, the inlet-velocity was considered as the boundary condition in the inlet of the vessel. Therefore, the velocity of oil/disperse/free phases plus the volume fraction of disperse/free water phases; and the 8 moments of the disperse phase at the inlet was inputted in the software. The pressure-outlet was considered as the boundary condition at the outlet of the vessel. This condition is known to results in the best numerical convergences. Based on the pilot plant experiments, the pressure at the outlet of the vessel was maintained at 10.6 atm. In the study, the walls of the vessel were considered to be stationary. Besides, it was considered that the contact angle between the water-oil phases is 45°, while the angle between the water phases is 0°.

As explained in Section 3.4, the coupled method (ANSYS 2016a) was used to solve the polydisperse system. In this study, the first-order upwind method was used for the discretization. The reason for not having used the higher-order upwind methods is that based on the book of Marchisio’s book [161] they might lead to nonconservation of the moments in the QMOM. The detailed setting of the simulations in the Ansys Fluent (R) software [96] is presented in Table 3-5.

Table 3-5: Settings of the CFD-PBE simulation in Ansys Fluent (R)

| | |
|--------------------------|--|
| General | <p>Solver: Double Precision</p> <p>Type: Pressure-base</p> <p>Velocity Formulation: Absolute</p> <p>Time: Dynamic</p> <p>2D Space: Axisymmetric</p> <p>Gravitational Acceleration: X (m/s²) -9.81</p> |
| Material | <p>Oil</p> <p>Disperse water</p> <p>Free water</p> |
| Models | <p>- Multiphase: Eulerian, Implicit formulation</p> <p>Number of phases: 3</p> <p>Primary Phase: Oil</p> <p>1st Secondary phase: Disperse Water</p> <p>2nd Secondary Phase: Free Water</p> <p>- Phase Interactions:</p> <p>Virtual Mass Modeling: none</p> <p>Drag: Schiller-Nauman + Drag Modification (user-defined)</p> <p>Lift: Legendre-magnaudet</p> <p>Wall Lubrification: none</p> <p>Mass: Mass Transfer (user-defined)</p> <p>Surface Tension Force Modeling: Continuum surface force modeling + Surface Tension Coefficient + Wall Adhesion</p> <p>Interfacial Area: ia-symmetric</p> <p>- Viscous: Laminar</p> |
| Population Balance Model | <p>Quadrature method of moment model (QMOM)</p> <p>k_v: 0.5235988</p> <p>Number of moments: 8</p> <p>Maximum diameter: 1e-3 (m)</p> <p>Minimum diameter: 1e-7 (m)</p> <p>Phenomena: Aggregation kernel (user-defined)</p> |
| Boundary condition | <p>- Walls: Stationary walls</p> |

| | |
|--------------------|---|
| | Contact angle: Oil- Disperse water (45°) Oil-Free water (45°) Disperse Water-Free water (0°) - Inlet: Inlet velocity - Outlet: Pressure outlet Mixture pressure outlet = 10.6 atm |
| Solution methods | - P-V coupling: Coupled - Spatial discretization Gradient: least-squares cell-based Momentum: 1 st order upwind Volume fraction: 1 st order upwind Moments: 1 st order upwind |
| Relaxation factors | Courant number: 200 Pressure: 0.5 Momentum: 0.5 Volume fraction: 0.25 Moments: 0.25 |

In this work, similar to [Section 3.2.2](#), the ComSol Multiphysics software (COMSOL Inc) was used to determine the profile of the steady-state electric field (DC) inside the continuous electrostatic vessel. The ComSol simulations were conducted for the two-dimensional geometry of [Figure 3-15](#). It's worth to mention that based on the electric field's equation ($E = -\nabla \phi$) [158], the profile of the DC electric field inside the vessel is independent on the local volume fraction of the water/oil. Then, the results of the simulation were used to fit a function in Matlab software ([Mathworks](#)) and the fitted function was implemented in Ansys Fluent using DEFINE_ON_DEMAND UDF. This macro was executed before running the CFD-PBE simulation to avoid the recalculation of the electric field. Moreover, the capture coefficient that is common between several UDFs were calculated in the DEFINE_ADJUST UDF to accelerate the calculation. The list of UDFs that were used in the simulations is presented in [Table 3-6](#).

Table 3-6: List of user-defined functions (UDFs)

| UDF | Functionality |
|----------------------------|--|
| DEFINE_ON_DEMAND | Determination of Electric field (1udf) |
| DEFINE_ADJUST | Calculation of Capture coefficient (1udf) |
| DEFINE_PB_COALESCENCE_RATE | Calculation of aggregation kernel (1udf) |
| DEFINE_PROPERTY | Calculation of representative diameter of free phase (1udf) |
| DEFINE_EXCHANGE_PROPERTY | Calculation of drag coefficient factor between oil-disperse water and oil-free water (2udfs) |
| DEFINE_MASS_TRANSFER | Calculation of mass transfer rate between the disperse and free water phases (1udf) |
| DEFINE_SOURCE | Calculation of source terms for the 8 moments (8udfs) |

Nomenclature

| | |
|------------------|---|
| a_α | breakage kernel |
| b_α | daughter distribution function |
| C_d | drag coefficient |
| d | diameter of droplet (m) |
| d_i | diameter of the smaller droplet (m) |
| d_{32} | Sauter-mean |
| $d_{electrodes}$ | distance between the electrodes (m) |
| d_{max}^{III} | maximum diameter of free water phase (m) |
| D_d | diffusion coefficient of the dispersed phase ($m^2.s^{-1}$) |
| e_{ij} | collision efficiency |
| E | electric field (N/C) |
| E_0 | electric field between the electrodes (N/C) |

| | |
|--------------------|--|
| f_{drag} | drag factor |
| $\vec{F}_{lift,q}$ | Lift force |
| \vec{F}_q | external body force |
| $\vec{F}_{td,q}$ | turbulent dispersion force |
| $\vec{F}_{wl,q}$ | wall lubrication force |
| $\vec{F}_{vm,q}$ | virtual mass force |
| g | gravitational acceleration (m/s ²) |
| G | droplet growth |
| H_k | Hankel determinants |
| K_{agg} | aggregation coefficient |
| K_{cap} | capture coefficient |
| m_k | k th moment of the classes of droplets (k = 0,...,2M-1) |
| \dot{m}_{pq} | mass transfer from the p^{th} to q^{th} phase |
| M | number of disperse droplet phases (M=4) |
| n | number density of droplets per volume of emulsion (1.m ⁻³ m ⁻³) |
| N | number of drops per volume of emulsion (1.m ⁻³) |
| N_n | normalized number of droplets per volume of emulsion (1.m ⁻³) |
| P | pressure (N/m ²) |
| $Q(d_i, d_j)$ | coalescence frequency of the droplets with diameters d_i and d_j |
| \vec{R}_{qp} | interaction force between phases |
| t | time (s) |
| S_q | source term in the continuity equation |
| v | characteristics size of droplets |
| V | volume (m ³) |
| u | velocity (m/s) |
| $u_{ij}^{(0)}$ | relative velocity of the two droplets (m/s) |
| w | weight in the QMOM formulation |

| | |
|-----|----------------------|
| z | special position (m) |
|-----|----------------------|

Greek symbols

| | |
|---------------------|---|
| ε | electrical permittivity (F. m ⁻¹) |
| ξ | abscissas in the QMOM formulation |
| μ | viscosity (kg·m ⁻¹ ·s ⁻¹) |
| $\hat{\mu}$ | ratio of the water viscosity to the oil viscosity |
| ρ | density (kg·m ⁻³) |
| $\hat{\rho}$ | ratio of the water density to the oil density |
| φ | volume fraction |
| ϕ | electrical potential |
| $\overline{\tau}_q$ | stress-strain tensor |
| λ | ratio of the radius of the small drop to that of the large drop |

Subscripts and Superscripts

| | |
|------------|--|
| <i>cal</i> | calculated by model |
| <i>cap</i> | capture term |
| <i>d</i> | droplet (disperse phase) |
| <i>e</i> | emulsion (oil + disperse water droplets) |
| <i>exp</i> | experimental value |
| <i>I</i> | oil phase |
| <i>II</i> | disperse water droplets in the oil phase |
| <i>III</i> | free-water phase |
| <i>O</i> | oil phase |
| <i>Sys</i> | system |
| <i>W</i> | water phase |

Abbreviations

| | |
|-------------------|--|
| <i>AC</i> | alternative current |
| <i>BS & W</i> | basic sediment and water (water content) |

Chapter 4 - Results and Discussions

4.1. Analysis of Batch Experiments and Model

In this section, first, the results of the batch experiments are presented. Then, the estimation of the parameters is discussed and the performance of the model to predict the experimental data is evaluated.

4.1.1. Analysis of the Stability of Emulsion

As explained in [Section 3.1.1](#), in this work, the model emulsion was used to perform the experiments. In order to examine whether the synthesized model emulsion has proper stability, the emulsions were examined using Turbiscan. [Figure 4-1-a](#) and [Figure 4-1-b](#) show the destabilization of the model emulsions with 15 and 5 water% w/w after 10 minutes, respectively, measured by backscattering.

The higher density of water makes the disperse droplets settle in the W/O emulsion. Therefore, the concentration of oil phase increases in the top of the Turbiscan's cuvette. As the refraction index of Exxsol ([Table 3-1](#)) suggests, it is a transparent solvent. Therefore, at the top of the cuvette, where the concentration of oil (here, the continuous phase of emulsion) is higher, a lower amount of beam is backscattered (clarification). The increase of backscattering at the bottom of the Turbiscan's cuvette is due to the accumulation of aqueous phase that creates an opaque white-colored abnormal emulsion.

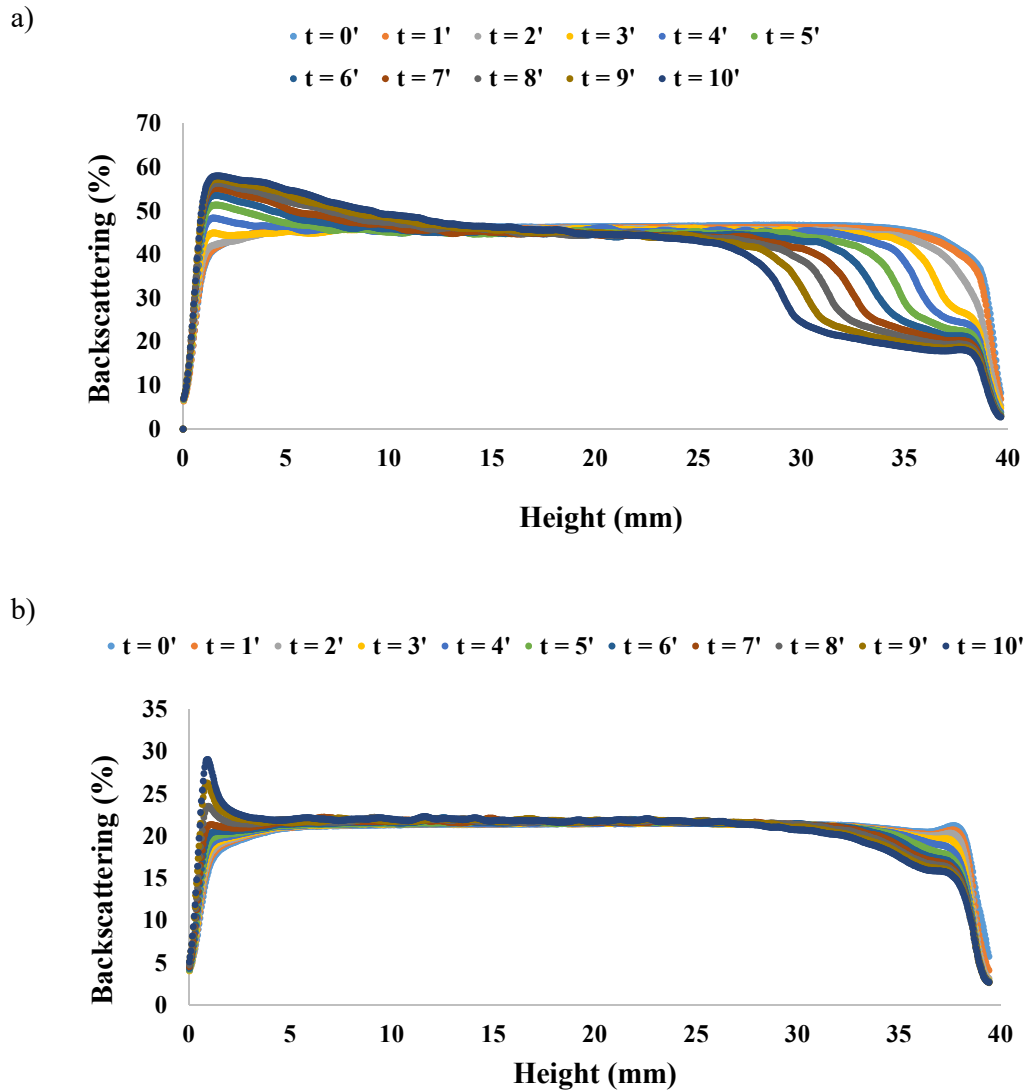


Figure 4-1: Turbiscan backscattering profile of the a) 15, b) 5 water% w/w model emulsions

Figure 4-1-a and Figure 4-1-b portray the backscattering analysis of the least and most stable synthesized emulsions in the experimental design matrix, respectively. The figures express that the model emulsion has enough stability for the electrostatic experiments which is comparable to crude oil.

The profile of Turbiscan backscattering had consistent/similar trends in other water% w/w and residence times. Although, due to the higher viscosity of emulsions with more amount of water% w/w (Equation (3-6)), the destabilization of emulsion was slower.

4.1.2. Analysis of the Stability of Saline Emulsions

Turbiscan analysis was also conducted for the saline emulsions. The addition of small% w/w of salt does not change significantly the density and viscosity of W/O emulsion. However, the presence of salt can increase or decrease considerably the surface tension of the W/O emulsion which affects its stability [4]. The change of surface tension by adding salt depends on the pH of salt solution and how it reacts with the W/O interface [4]. In this work, NaCl that is a neutral salt was added to the water-in-Exxsol emulsions. The result of stability tests showed that the addition of the salt increases the stability of W/O emulsions. This signifies that the reaction of NaCl with the water-Exxsol interface rigidifies the layer. **Figure 4-2-a** and **Figure 4-2-b** depict the destabilization of the saline model emulsions with 15 and 5 water% w/w after 10 minutes, respectively. The figures indicate that the backscattering of saline emulsions are lower than the equivalent emulsions without salt. The profiles of Turbiscan backscattering showed similar/consistent behaviors for other saline emulsions. Even though, likewise, the emulsions with a higher amount of saline content were more stable (**Equation (3-6)**).

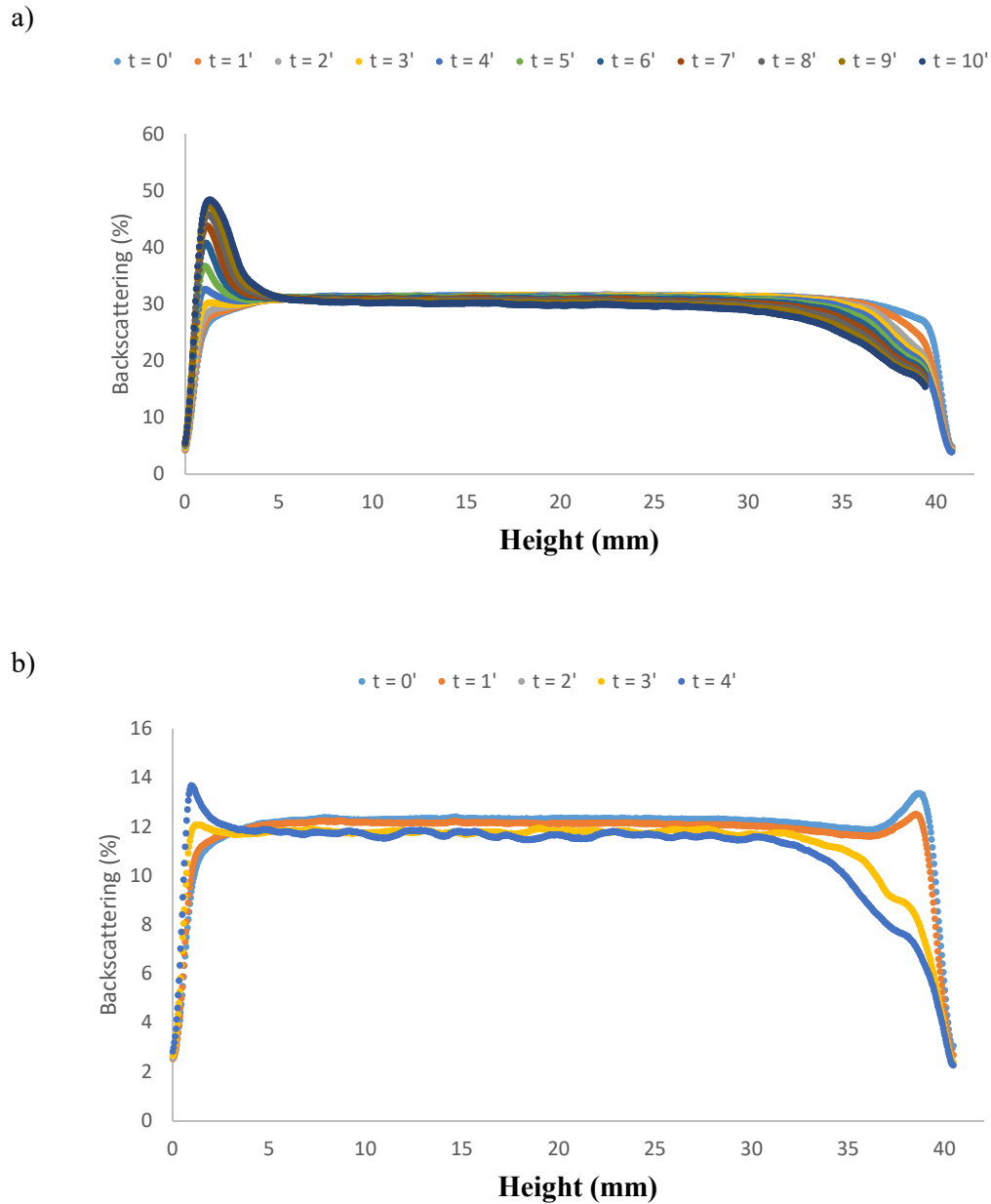


Figure 4-2: Turbiscan backscattering profile of the a) 15, b) 5 water% w/w saline model emulsions

4.1.3. Analysis of the Electrostatic and Sedimentation Experiments

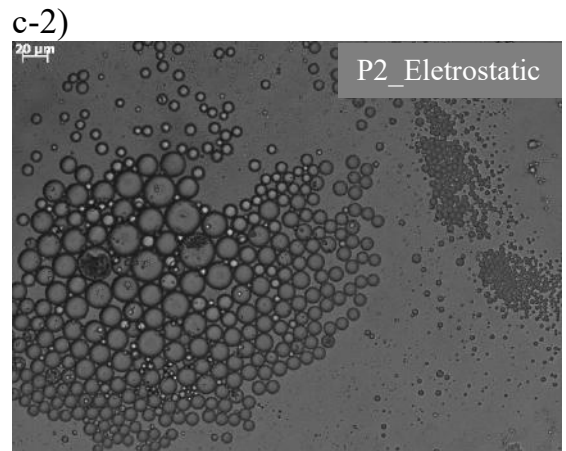
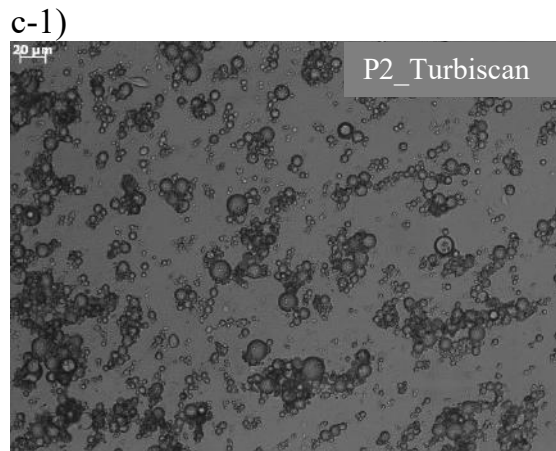
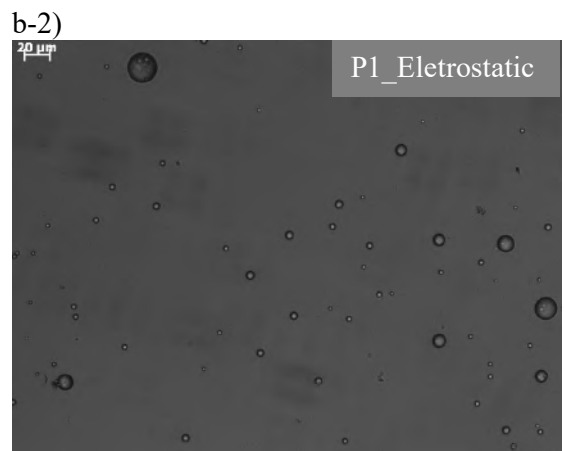
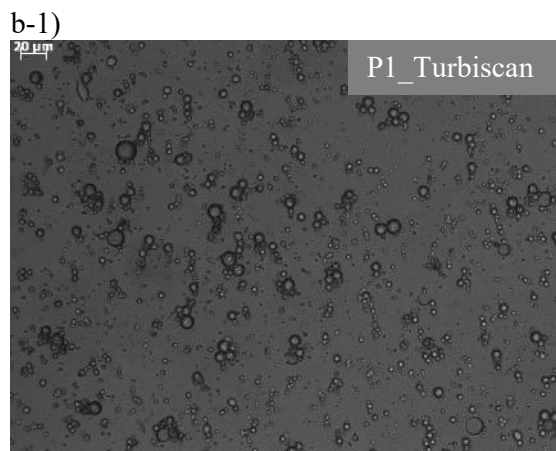
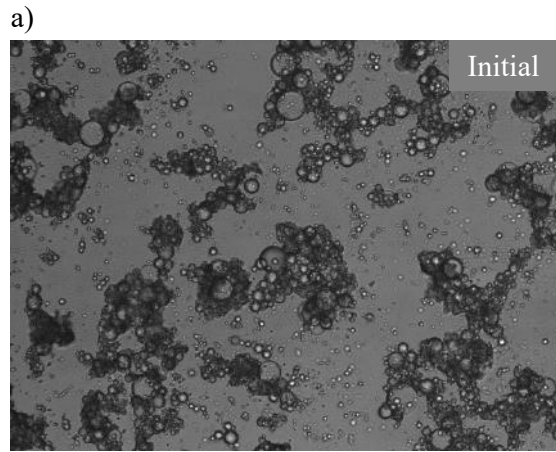
The BS&W values of the sedimentation and electrostatic tests are presented in Table 4-1. By reviewing the results of the experiments, it can be verified that the assumption of ignoring gravitational coalescence in comparison to electrocoalescence in Section 3.2.1 is justifiable. The difference between the values of BS&W in the Turbiscan and

electrostatic tests is attributed to the electric field which increases the size of droplets by making them coalesce together. Therefore, the settling velocity of aqueous phase increases, which enhances the sedimentation.

Table 4-1: Results of the electrostatic and Turbiscan tests

| Experimental design | | | | BS&W (Turbiscan) | | | BS&W (Eletrocoalescer) | | |
|---------------------|-----------|-----------|------------|---------------------|-------|-------|---------------------------|-------|-------|
| Run | WC (%) | V (kV) | t (min) | P1 | P2 | P3 | P1 | P2 | P3 |
| 1 | 1 | 1 | 1 | 2.68 | 16.77 | 17.41 | 1.36 | 10.90 | 54.53 |
| 7 | 1 | 1 | -1 | 9.37 | 15.16 | 15.58 | 1.27 | 41.60 | 50.73 |
| 6 | 1 | -1 | 1 | 2.51 | 17.10 | 17.50 | 0.84 | 26.56 | 48.88 |
| 9 | 1 | -1 | -1 | 7.61 | 12.26 | 9.88 | 0.96 | 32.25 | 55.04 |
| 2 | -1 | -1 | -1 | 4.45 | 4.61 | 4.58 | 1.47 | 1.46 | 2.34 |
| 10 | -1 | 1 | -1 | 3.24 | 3.50 | 3.50 | 1.02 | 1.13 | 28.55 |
| 3 | -1 | 1 | 1 | 3.99 | 4.42 | 4.34 | 0.62 | 0.88 | 9.77 |
| 4 | -1 | -1 | 1 | 4.42 | 4.64 | 4.74 | 0.54 | 0.81 | 15.46 |
| 5 | 0 | 0 | 0 | 3.75 | 9.37 | 9.32 | 0.96 | 1.11 | 46.74 |
| 8 | 0 | 0 | 0 | 3.55 | 10.11 | 11.04 | 1.01 | 1.13 | 44.70 |
| 11 | 0 | 0 | 0 | 2.81 | 9.68 | 11.31 | 0.95 | 1.01 | 32.01 |

The microscope images of the Turbiscan and electrostatic tests for the 1st experimental point (Table 3-2) are shown in Figure 4-3. The figure reverifies the assumption made in Section 3.2.1 The Turbiscan images show mild sedimentation of droplets with small changes in the DSD. While the electrocoalescer images illustrate the significant sedimentation of droplets with a considerable change of DSD. The increase of DSD under the effect of electric field is specifically sensible at the bottom of the electrocoalescer where the droplets are accumulated (Figure 4-3-d-2). The low concentration of disperse phase at the top of the vessel (Figure 4-3-b-2) is accredited to the increase of DSD which enhances the sedimentation of droplets and rise of the oil phase.



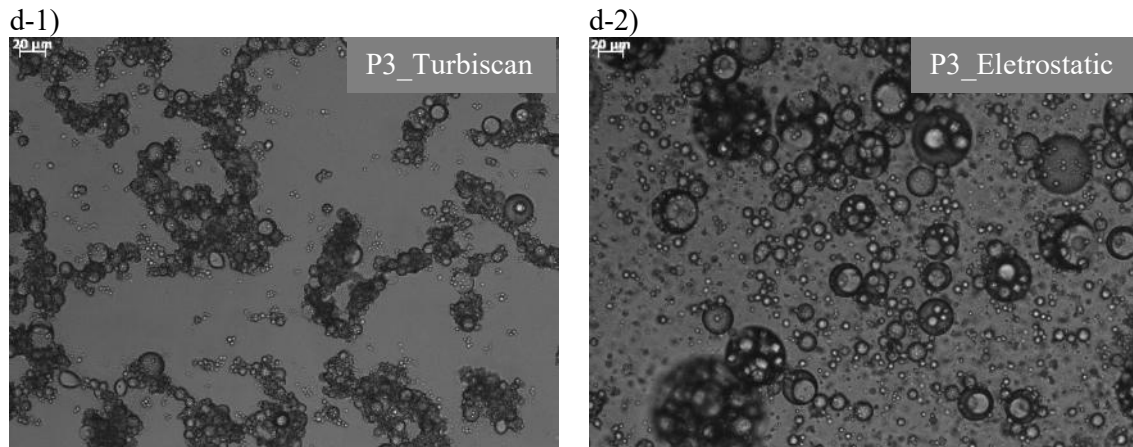


Figure 4-3: Microscopic images of the 1st experimental point: a) Initial sample, Turbiscan b-1) P1, c-1) P2, d-1) P3, Electrocoalescer b-2) P1, c-2) P2 d-2) P3

The electrostatic experiments analyzed the effects of electric field intensity, initial water content, and electrostatic time on the amount of separation. The influence of these variables is separately discussed in the following subsections.

4.1.3.1. Effect of Electric field Intensity

As shown in [Table 4-1](#), the increase of electric field intensity improves the separation of water droplets. However, there exists an optimal electrical intensity where the separation efficiency achieves its maximum value [172]. Electro-coalescence and electrodispersion are considered as the principal behaviors of water droplets in W/O emulsion under the effect of electric field. When a relatively low electric field is applied to W/O emulsion, droplets are immediately polarized due to the distribution of surface charges. The induced dipole interaction make pairs of droplets to approach and ultimately coalesce together. However, at relatively high electrical intensities, the bipolarity of droplets forms rotating elliptical droplets. The phenomenon: electro-dispersion, leads to breakage of the droplets which hinders the coalescence. These two phenomena can be perceived in [Table 4-1](#) as by increasing the electrical intensity, the rate of separation's enhancement has decreased.

4.1.3.2. Effect of Initial Water Content

As the experimental data in [Table 4-1](#) expresses, the increase of initial water content improves the separation. At a relatively low amount of water content, the distance

between the disperse phases is high which hinders the collision and coalescence of droplets. This phenomenon has been observed for the experimental points with the initial 5 water% w/w. As the initial water content increases, the distance between the droplets decreases while increasing the number/size of the droplets which enhances the coalescence. Nevertheless, there is an optimum amount of initial water content where the separation obtains its maximum efficiency [172].

The increase of initial water content increases the load on the electric field to polarize a higher number of droplets. Therefore, it is expected that the separation's efficiency decreases after reaching a certain limit of initial content. This is witnessed in [Table 4-1](#) as for the increase of initial water content from 10 to 15 water% w/w, the rise of separation has decreased.

4.1.3.3. Effect of Electrostatic Time

As presented in [Table 4-1](#), the increase of electrostatic time enhances the separation of phases. The increase of electrostatic time provides the necessary residence time for a higher number of the droplets to be polarized and coalesce together. However, as the droplets coalesce together and sediment, a fewer number of droplets will be available in the space between the electrodes and consequently, an unnecessary amount of energy will be used. As a result, there exist an optimum electrostatic time when the separation of droplets obtains its maximum. This trend is observed in [Table 4-1](#) as the increase of electrostatic time from 7 to 10 minutes is not compensated by a sensible augmentation of aqueous phase separation.

4.1.4. Analysis of the Electrostatic and Turbiscan Experiments for saline emulsions

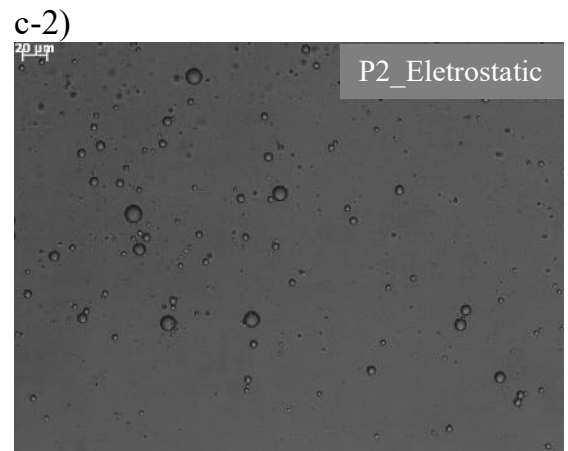
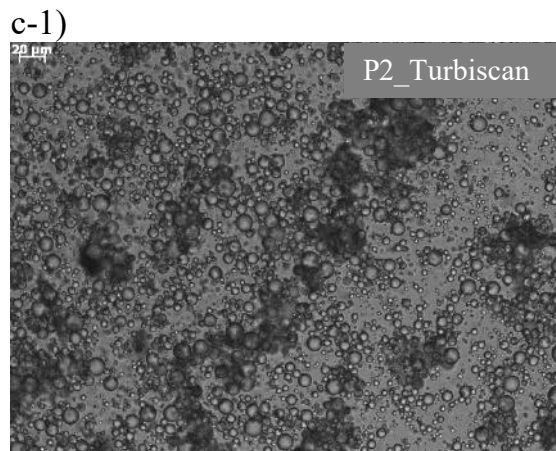
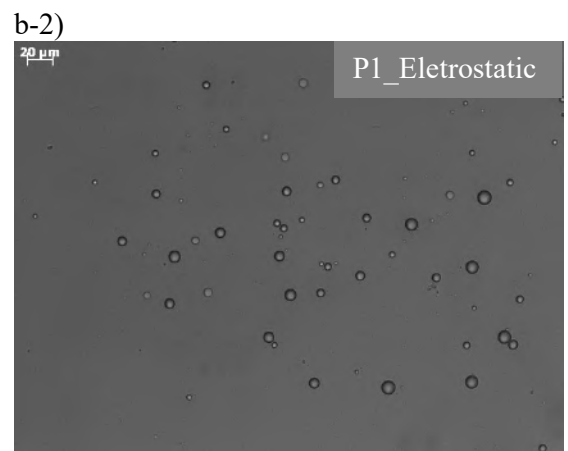
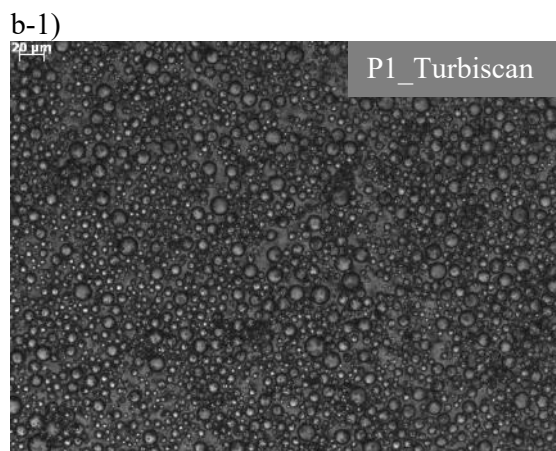
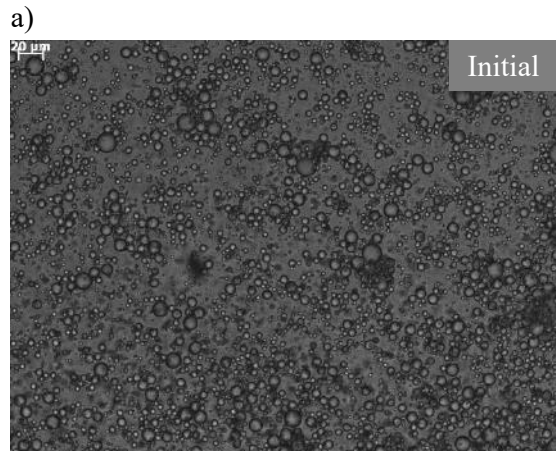
The addition of salt to the W/O emulsions has two separate effects on the performance of electrocoalescence [4]. As explained in [Section 4.1.2](#), the presence of salt in the emulsion can alter the surface tension and consequently the stability of the emulsion. In this study, the results of Turbiscan analysis showed that the addition of 3.5% w/w of NaCl to aqueous phase water-in-Exxsol emulsion decreases the surface tension. The other effect of salt is the increase of the dielectric constant of the emulsion that enhances the efficiency of electrocoalescence. Therefore, depending on the two effects, the addition of salt to the

emulsion could improve or diminish the separation of phases in the electrocoalescence process. Different conclusions have been drawn in the literature about the influence of the addition of salt in the electrocoalescence process [4]. In this work, the results of experiments showed that the addition of salt improved the electrocoalescence. The BS&W values of the Turbiscan and electrostatic tests for saline emulsions are presented in Table 4-2.

Table 4-2: Results of the electrostatic and Turbiscan tests for saline emulsions

| Experimental design | | | | BS&W (Turbiscan) | | | BS&W (Electrocoalescer) | | |
|---------------------|--------|--------|---------|------------------|-------|-------|-------------------------|------|-------|
| Run | WC (%) | V (kV) | t (min) | P1 | P2 | P3 | P1 | P2 | P3 |
| 1 | 1 | 1 | 1 | 7.46 | 9.09 | 8.95 | 0.32 | 0.72 | 92.97 |
| 7 | 1 | 1 | -1 | 9.88 | 9.35 | 9.10 | 0.61 | 0.90 | 94.24 |
| 6 | 1 | -1 | 1 | 9.06 | 10.28 | 11.03 | 0.86 | 1.00 | 51.66 |
| 9 | 1 | -1 | -1 | 1.02 | 2.48 | 90.59 | 9.80 | 9.87 | 9.63 |
| 2 | -1 | -1 | -1 | 3.11 | 3.35 | 1.52 | 0.84 | 5.92 | 0.44 |
| 10 | -1 | 1 | -1 | 3.29 | 2.89 | 2.52 | 0.53 | 0.64 | 4.52 |
| 3 | -1 | 1 | 1 | 0.63 | 3.85 | 3.37 | 0.49 | 0.95 | 1.79 |
| 4 | -1 | -1 | 1 | 3.16 | 4.09 | 3.49 | 0.53 | 0.64 | 1.79 |
| 5 | 0 | 0 | 0 | 8.59 | 10.76 | 9.52 | 0.63 | 0.52 | 67.21 |
| 8 | 0 | 0 | 0 | 7.89 | 9.65 | 8.60 | 0.68 | 0.36 | 52.32 |
| 11 | 0 | 0 | 0 | 9.67 | 7.24 | 8.57 | 0.48 | 0.66 | 42.57 |

The microscope images of the Turbiscan and electrostatic tests for the 1st experimental point (Table 3-2) of saline emulsions are shown in Figure 4-4. The processing of the Turbiscan and electrostatic images are similar/consistent to Figure 4-3. However, by comparing Figure 4-3 and Figure 4-4 it can be concluded that the addition of salt improved the separation of phases in the electrocoalescence process. Figure 4-4-b-2 and Figure 4-4-c-2 show that the number of droplets that remained at the top and middle of the vessel is smaller. Furthermore, Figure 4-4-d-2 expresses that the accumulated droplets at the bottom of the vessel are more and bigger.



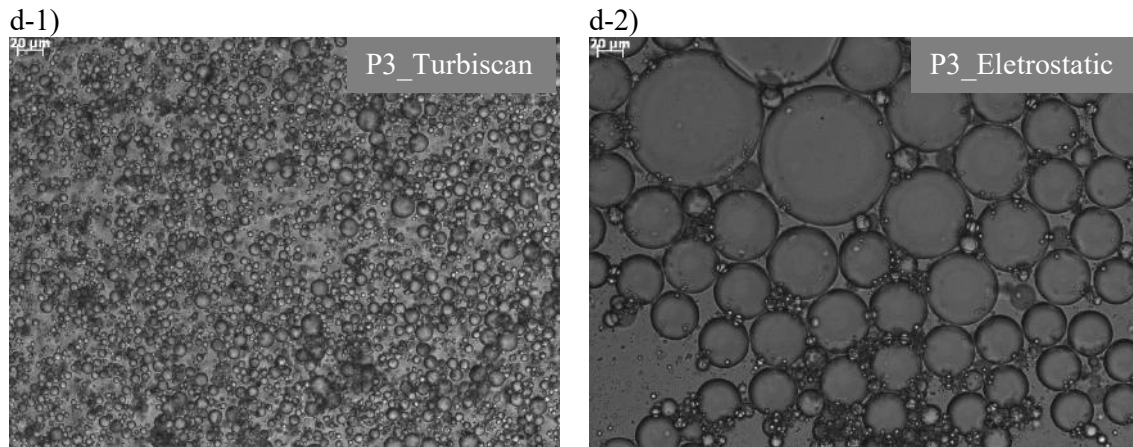


Figure 4-4: Microscopic images of the 1st experimental point for saline emulsions: a) Initial sample, Turbiscan b-1) P1, c-1) P2, d-1) P3, Electrocoalescer b-2) P1, c-2) P2 d-2) P3

The results of electrostatic experiments for saline emulsions were to some extent similar to [Section 4.1.3.1-3](#). However, due to the probable bad preparation of the model emulsion and batch characteristic of the experiments, it was not possible to find trends for all experimental point. Nevertheless, it can be concluded that the increase of dielectric constant by adding salt was dominant to other influencing/hindering factors. The amounts of separation in almost all experimental points ([Table 4-2](#)) are more than the equivalent test for non-saline emulsions ([Table 4-1](#)). The results suggest that a smaller period of time was needed to break the emulsions. This signifies that the segregation of phases did not improve considerably by increasing electrostatic time. Moreover, the electric field was able to overcome the significant drag force at high water contents and reach >90% separation ([Table 4-2](#)) at P3 ([Figure 3-4-a](#)). Unfortunately, in the batch experiments, the water content at the exact bottom wall of the vessel was not measured. Therefore, it was not possible to see whether 100% is reached or not. For this reason, it is not possible to draw a conclusion about the effect of increasing the electric field on the efficiency of electrocoalescence.

4.1.5. Estimation of Batch Model Parameters

In this section, the results of the batch electrostatic experiments were used to estimate the parameters of the model described in [Section 3.2](#). In order to run the batch model, the distribution of the electric field inside the batch vessel should be determined. The profile of electric field for the central experimental point ([Table 3-2](#)) obtained by ComSol

software (COMSOL Inc) is shown in [Figure 4-5](#). In the figure, V_0 is the potential of the charged electrode.

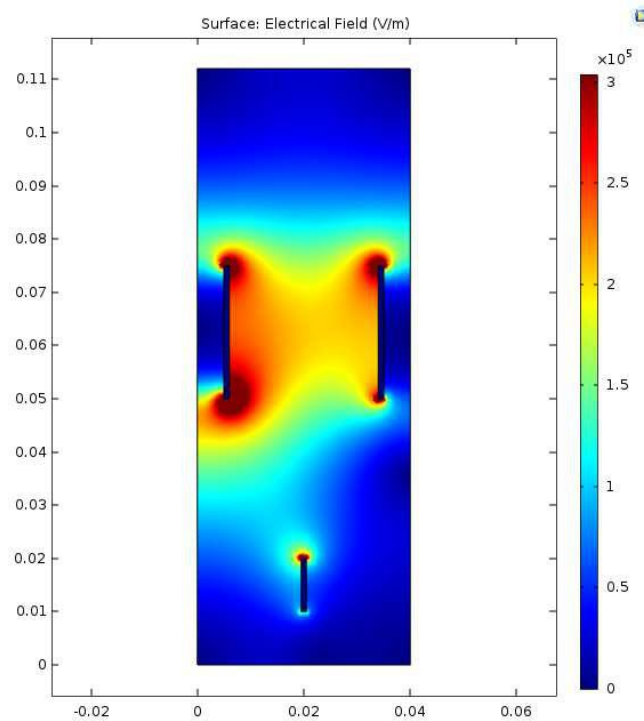


[Figure 4-5](#): 2D Profile of electric field inside the batch vessel ($V_0 = 6\text{kV}$)

[Figure 4-5](#) shows that the electric field is nonzero at all point of the vessel. This means that based on the aggregation kernel ([Equation \(3-14\)](#)), the coalescence between the droplets happens in all elevations of the vessel. However, the figure displays because of the higher gradient of the electrical potential, that the electric field between the electrodes is stronger. The figure also indicates that at the two corners of the non-ground electrode (left electrode in [Figure 4-5](#)), has the highest values of electric field. The distribution of electric field inside the batch vessel for other potentials $V_0 = 4\text{kV}$ and $V_0=8\text{kV}$ are portrayed in [Figure 4-6-a](#) and [Figure 4-6-b](#), respectively. The figures have similar trends to [Figure 4-5](#). Nevertheless, the profiles of electric field are stronger for $V_0=8\text{kV}$ and weaker for $V_0 = 4\text{kV}$, respectively, compared to [Figure 4-5](#).

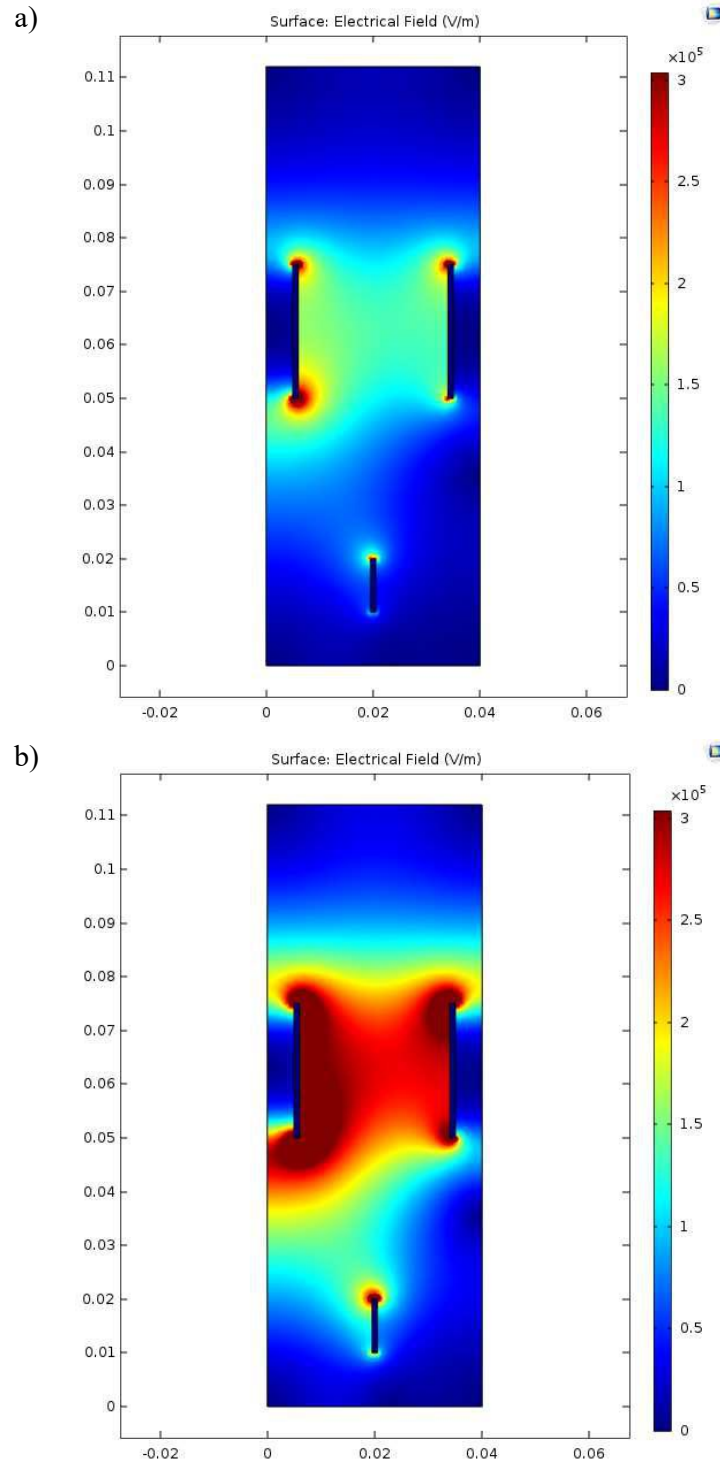


Figure 4-6: 2D Profile of electric field inside the batch vessel for a) $V_0 = 4\text{kV}$ b) $V_0 = 8\text{kV}$

The parameters of the batch model are $K_{cap,0}$, $K_{cap,E}$, K_{agg} . The $K_{cap,0}$ coefficient characterizes the capture of droplets in the absence of electric field. The $K_{cap,E}$ expresses

the influence of electric field on the segregation/capture of droplets while K_{agg} describes the collision and coalescence of droplets under the effect of electric field. In this work, the subsets of experimental points of electrocoalescence tests with the same values of initial water content and electrical potential were used to estimate the parameters. Besides, the results of Turbiscan tests were used to find an initial interval of $K_{cap,0}$ for parameter estimation, while the other two parameters were made equal to zero. Here, it is worth to mention some numerical issues about the parameter estimation. Due to the physical/numerical limitations of PBE, it was not possible to increase the K_{agg} above certain values for each experimental point. There are two mathematical tricks to stop the rise of DSD in a pure aggregation PBE. The first one is to zero the birth/death aggregation terms in case the average diameter of droplets passes a certain limit. The second way is to zero the aggregation kernel when one or both of the two droplets coalescing together are bigger than a specified diameter. However, in this study, our executions showed that for both ways, the Dassl [167] and ode15s (Mathworks) integrators face problems to proceed if they reach the conditions. Likewise, the moment inversion to calculate the source terms of the PBE (Equation (3-10)) was quitted if the volume fraction of disperse water phase was less than $1e-4$. Moreover, unfeasible values of capture coefficient could create instabilities in the integration. Therefore, in this work, first, the estimative intervals of the parameters were obtained by try and error, and then the PSO algorithm [168] was used to estimate the parameters. Furthermore, because of the high gradient of the variables especially at the bottom of the vessel (where the water phases accumulate), it was necessary to monitor the Courant number: $C = u\Delta t/\Delta x$. The reason is to check/set the maximum Δt of the integrator to ensure stable/conservative results. The values of estimated parameters are presented in Table 4-3.

Table 4-3: Values of estimates parameters

| Experiment | $K_{cap,0}$ | $K_{cap,E}$ | K_{agg} |
|----------------------------|-------------|-------------|-----------|
| 1,7 (BS&W=15%, V0=8kV) | 2.1543e7 | 2.215e3 | 4.8e-9 |
| 6,9 (BS&W=15%, V0=4kV) | 1.2503e7 | 1.2564e3 | 9.9e-9 |
| 2,4 (BS&W=5%, V0=4kV) | 5.688e7 | 4.914e3 | 5.8e-8 |
| 10,3 (BS&W=5%, V0=8kV) | 5.526e7 | 4.917e3 | 1.4e-8 |
| 5,8,11 (BS&W=10%, V0=6kV) | 3.3649e7 | 2.2621e3 | 1e-8 |

The results of parameter estimation show that the electrocoalescence is more important for emulsions with a lower amount of water content. As [Table 4-3](#) suggests, for experimental points with the same electrical potential, the value of K_{agg} is greater for emulsions with lower water contents. Conversely, the capture phenomenon is dominant in emulsion with a higher amount of water%.

The calculated and experimental values of the BS&W for all 11 experimental points are presented in [Table 4-4](#). In the table, the BS&W-Error is the root of the mean square errors of the three sample points (P₁, P₂, and P₃ in [Figure 3-4-a](#)). The table indicates that the model has a decent performance in predicting the behavior of batch electrocoalescence. However, there are differences between the calculated and experimental values that need to be explained. The first kind of deviation is related to the experiments. The stability of model emulsions could alter in different preparations. Therefore, the quality of electrocoalescence tests could be influenced by improper preparation of emulsions. This factor was specifically evident in emulsions with low amount of water content ([Table 4-1](#)) where the stability of emulsions are inherently less (2nd, 10th experimental points). Moreover, the Karl Fischer equipment (KF Titrand 836, Metrohm) and microscope (Carl Zeiss)/imageJ analyzer (National Institutes of Health) that were used to measure the BS&W and DSD, respectively, have intrinsic errors. Additionally, measuring specifically from the bottom of the vessel where the gradient of variables is high, is prone to large errors. Consequently, a small change in the elevation of sample measuring (P₂, P₃ in [Figure 3-4-a](#)) makes big differences. Another important point is the measuring delay time that is at least 1-2 minutes. In the experimental design of the experiments, the electrostatic time is referred to the moment when the electrical source is turned off. However, because of the creation of a noticeable amount of free phase, the separation of phases continues without the presence of electric field. This factor can be mathematically seen through the $K_{cap,0}$ coefficient ([Equation \(3-17\)](#)) that is independent of the electric field. This segregation of phases is specifically influential for experiments with short electrostatic time (4 minutes) (e.g. 9th experimental point).

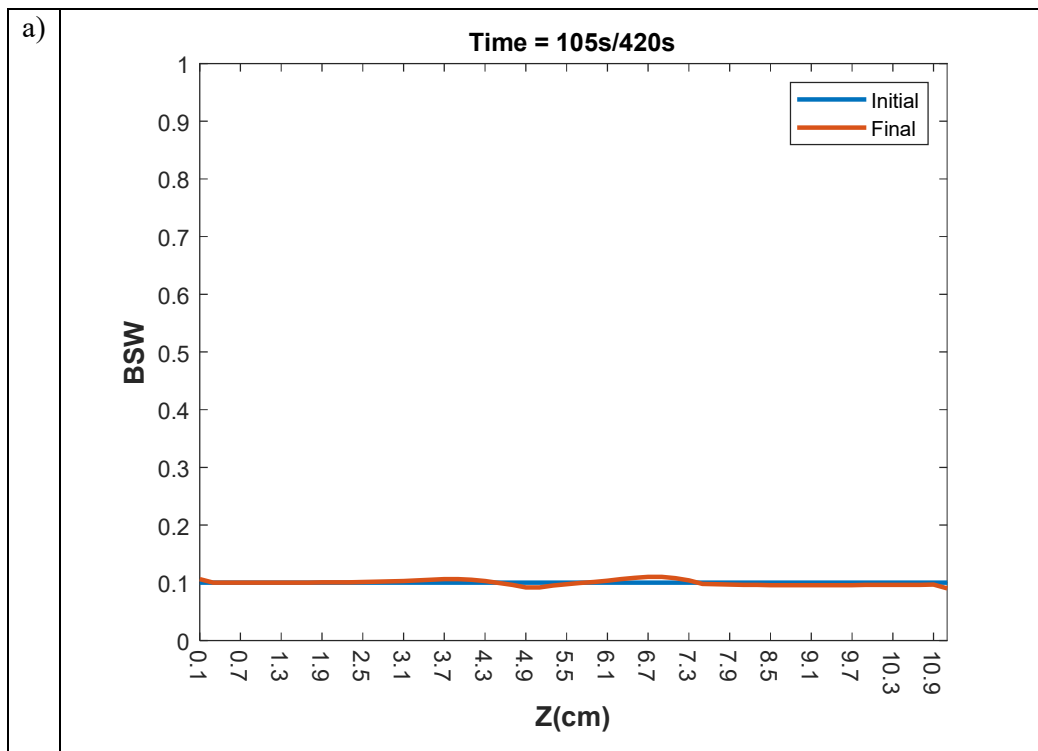
Table 4-4: Calculated and experimental values of BS&W

| Experiment | d_ave (μm) | P1- Exp | P1- Cal | P2- Exp | P2- Cal | P3- Exp | P3- Cal | BS&W- Error |
|------------|----------------------------|------------|------------|------------|------------|------------|------------|----------------|
| 1 | 4.7 | 1.36 | 1.95 | 10.90 | 11.95 | 54.53 | 69.26 | 8.52 |
| 7 | 6.2 | 1.27 | 3.42 | 41.60 | 30.24 | 50.73 | 38.66 | 9.65 |
| 6 | 4.5 | 0.84 | 3.84 | 26.56 | 21.84 | 48.88 | 48.86 | 3.23 |
| 9 | 6.7 | 0.96 | 12.84 | 32.25 | 16.93 | 55.04 | 15.01 | 25.68 |
| 2 | 6.8 | 1.47 | 1.08 | 1.46 | 4.81 | 2.34 | 12.37 | 9.57 |
| 10 | 6.1 | 1.02 | 2.43 | 1.13 | 7.87 | 28.55 | 8.75 | 12.10 |
| 3 | 5.5 | 0.62 | 0.68 | 0.88 | 2.52 | 9.77 | 11.14 | 1.23 |
| 4 | 5.7 | 0.54 | 0.36 | 0.81 | 1.81 | 15.46 | 13.27 | 1.39 |
| 5 | 6.3 | 0.96 | 1.53 | 1.11 | 7.18 | 46.74 | 47.18 | 3.92 |
| 8 | 6.2 | 1.01 | 1.61 | 1.13 | 7.52 | 44.70 | 45.16 | 3.72 |
| 11 | 5.5 | 0.95 | 2.07 | 1.01 | 9.53 | 32.01 | 33.05 | 4.99 |

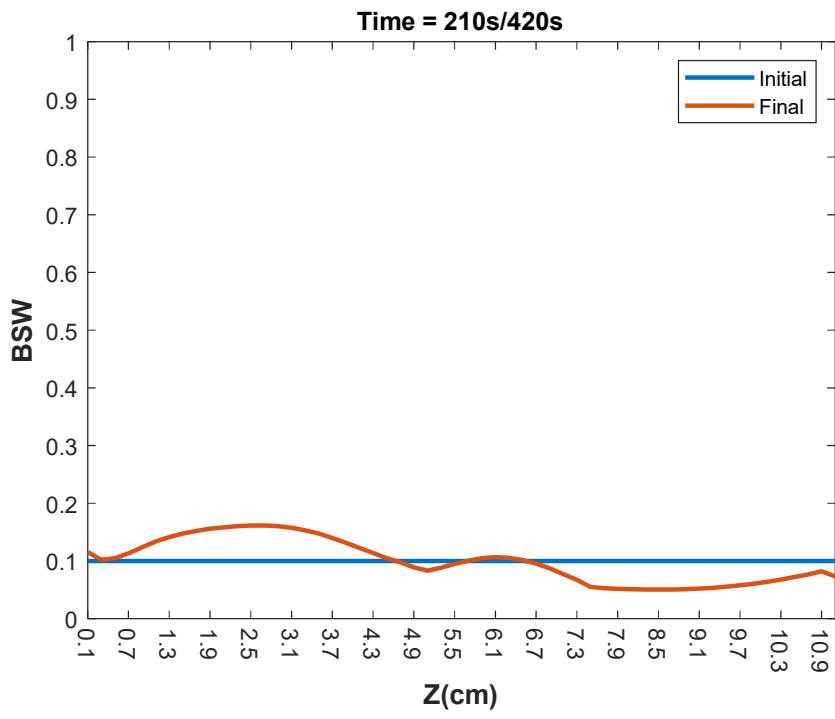
The second type of deviation is related to the batch model. In this work, it was considered that the initial emulsion is homogenous and the BS&W/DSD in all elevations of the vessel are the same. The nonhomogeneous characteristic of emulsion creates perturbations that could affect the precision of the model. The homogeneousness of the emulsion is mostly questionable at the top and bottom of the vessel where a proper initial mixing of the emulsion is difficult. Although the precision of the model to predict the water content at the P1 point (Figure 3-4-a) seems to be notable, the main deviation from the experimental data was seen at the bottom of the vessel (P2, P3 in Figure 3-4-a). In this work, the polydisperse Eulerian-Eulerian model was employed to predict the separation of phases in the electrocoalescence process. The fundamental assumption of the model is that the secondary phase is disperse and it is represented by a diameter. However, at the bottom of the vessel where the water phases accumulate, it is difficult to differentiate between disperse or continuous water phase. Therefore, the assumption of the Eulerian model would be questionable. This factor along the high gradient of the variables at the bottom of the vessel can be attributed to the deviations of the model from experimental data (e.g. 1st, 7th experimental points).

In this section, the detailed results of the batch model for three experimental points (1, 3, and 5) are discussed. The profiles of BS&W for the central (5th) experimental point at time=105s, 210s, 315s, 420s are shown in Figure 4-7. The phenomena happen

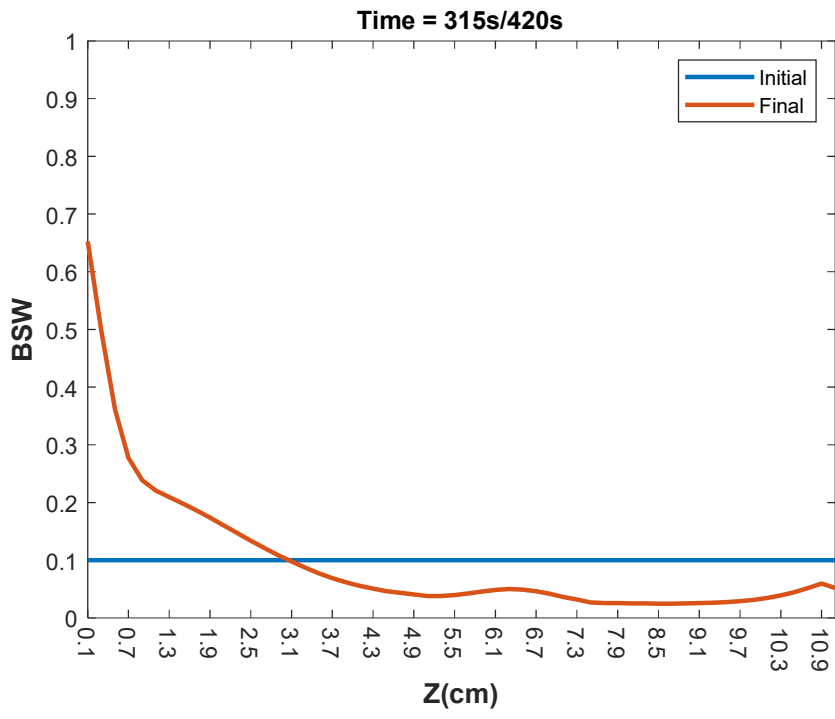
simultaneously in the electrostatic vessel are electrocoalescence, capture, and sedimentation that lead to the segregation of aqueous phases from oil. In the absence of electric field, the electrocoalescence is zero and the capture is slow. As the process starts, initially, the dominant phenomenon is the electrocoalescence specifically between the electrodes where the electric field is stronger (Figure 4-5). The creation of bigger droplets reduces the drag coefficient (Equation (3-3)) which leads to the local changes of BS&W and sedimentation in the regions between the electrodes (Figure 4-7-a). The two small picks of the BS&W is due to the high electric field at the two corners of the potential electrode (Figure 4-5). Besides, the slight changes of BS&W at the two ends of the figure is because of the accumulation of water and oil at the bottom and top of the vessel, respectively. As the process continues, the capture term becomes important and the creation of free phase results in the sedimentation of the aqueous phases (Figure 4-7-b). The free phase reaches the bottom of the vessel and the water phases accumulate (Figure 4-7-c). The accumulation of water at the bottom of vessel attains a maximum value (Figure 4-7-d). This is due to the high amount of drag force at a concentrated volume fraction of secondary phase. Mathematically, the saturation of accumulation of water phases is because of the mathematical form of the modified drag coefficient (Equation (3-4)).



b)



c)



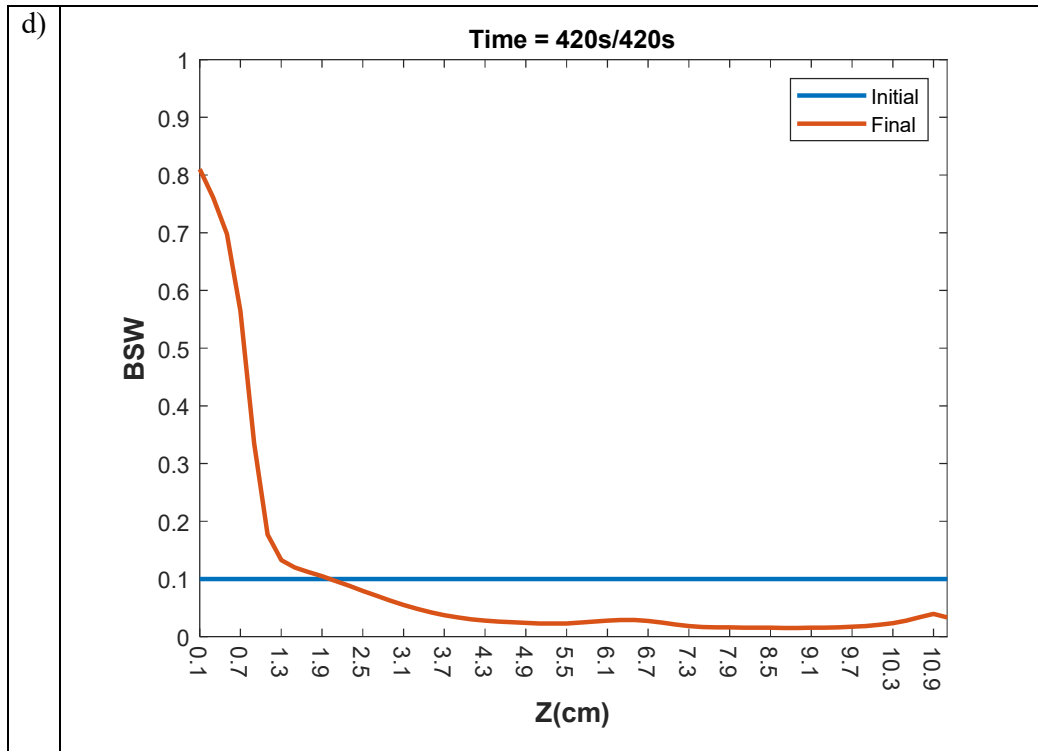
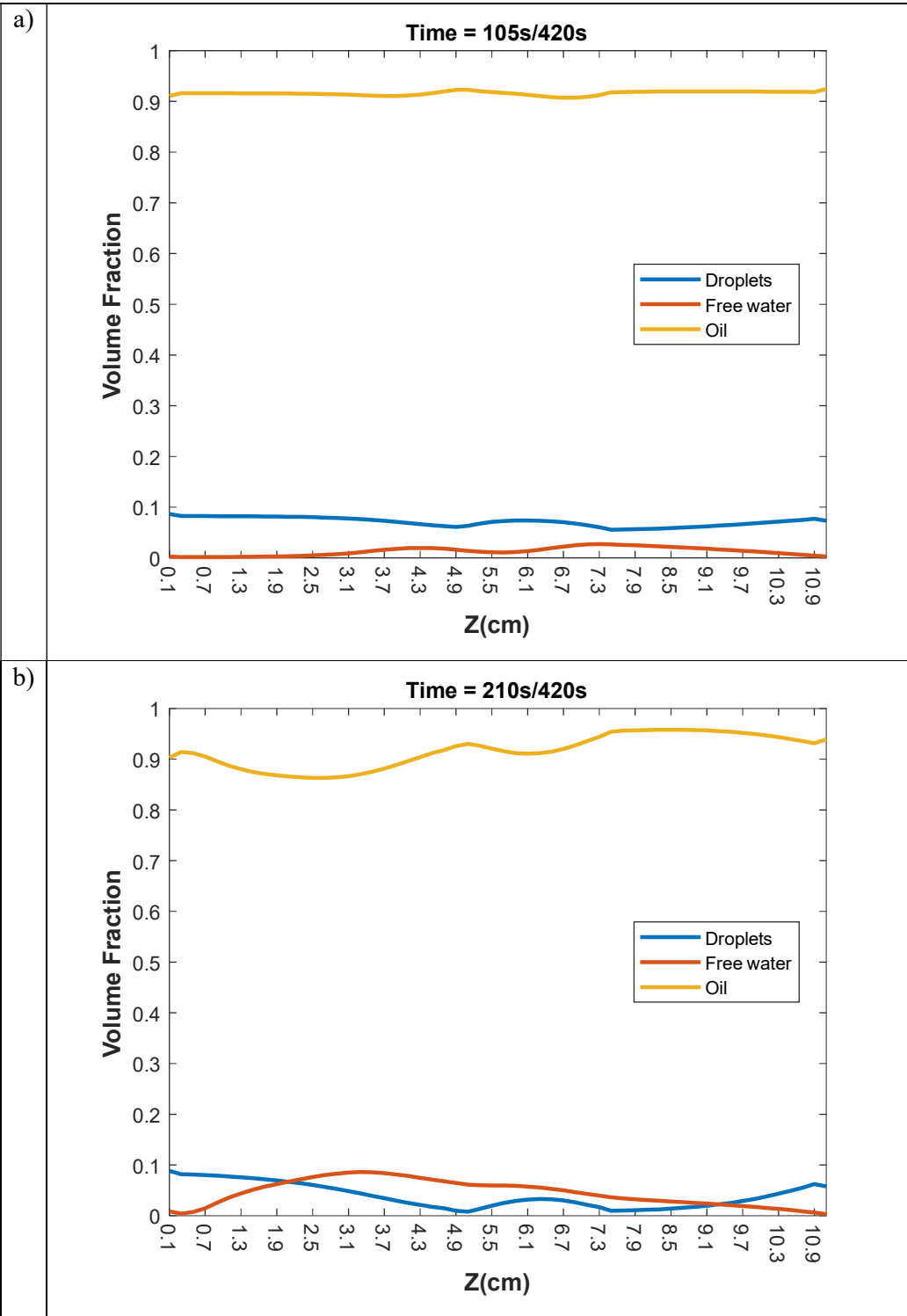


Figure 4-7: Profile of BS&W for the central (fifth) experimental point at a) time = 105s, b) time = 210s, c) time = 315s, d) time = 420s

The separation/segregation in the electrocoalescence process can be better observed in the figure volume fraction of phases. The profiles of volume fractions of the phases for the central (5th) experimental point at time=105s, 210s, 315s, 420s are depicted in Figure 4-8. It is perceivable from the figure that as the process proceeds, the capture dominates the aggregation of droplets. The highest rate of capture is between the electrodes where the electric field is higher and the droplets have the highest diameters (Equation (3-17)). On the contrary, the capture at the top of the vessel is small as the volume fraction of free phase is low. Therefore, the volume fraction of droplets at the top of the vessel is locally higher. However, this is a deviation of the model from the experimental data. This is due to the non-homogeneous of the initial emulsion at the top of the vessel that was not considered in the modeling. As the free phase sediments, it captures the droplets. The accumulated free phase at the bottom of the vessel capture the droplets at a high pace. This is why ultimately, the maximum volume fraction of droplets is in the regions before the bottom of the vessel. Based on Figure 4-8, the sedimentation of the aqueous phases is because of the creation of free phase that is initially dependent on aggregation and in continuation because of the capture.



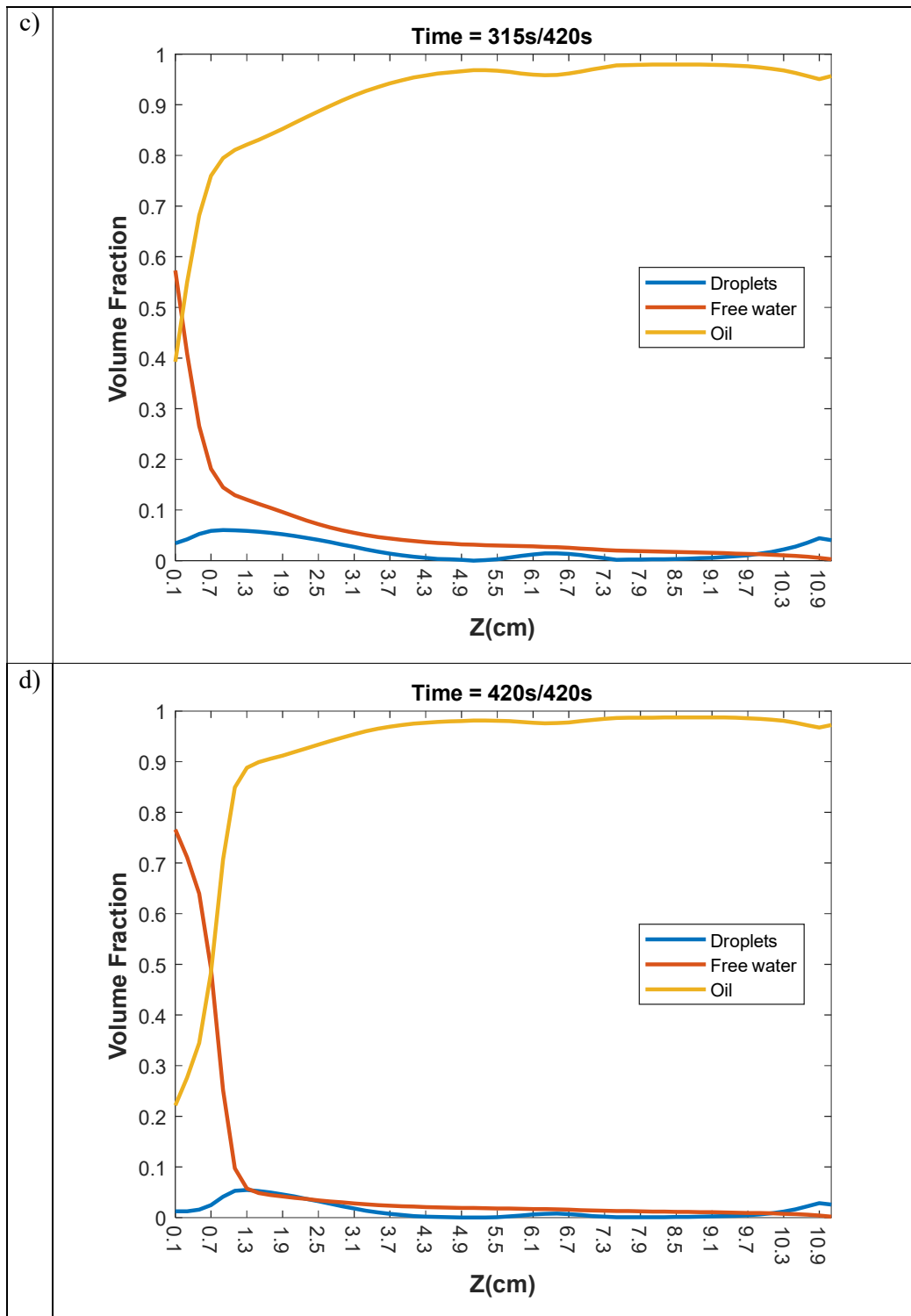
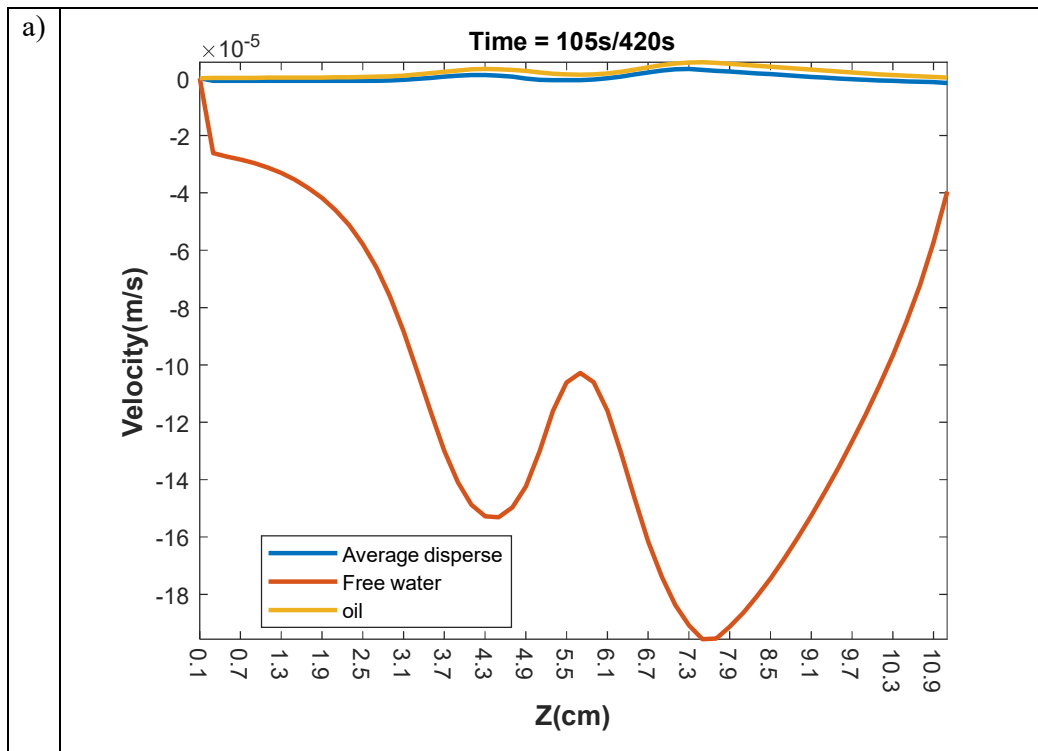
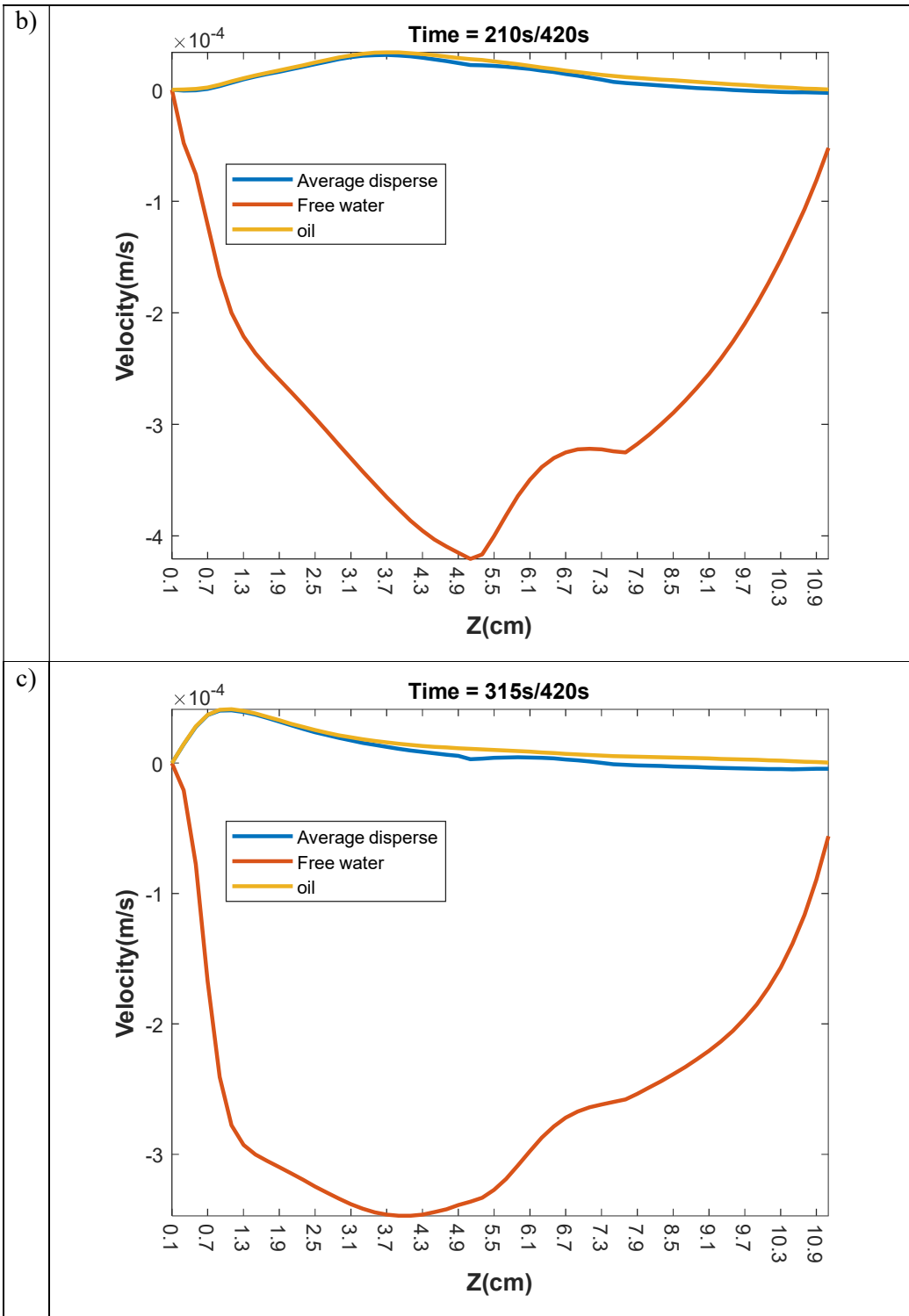


Figure 4-8: Profile of volume fraction of phases for the central (fifth) experimental point at a) time = 105s, b) time = 210s, c) time = 315s, d) time = 420s

The profiles of velocities of the phases for the central (5th) experimental point at time=105s, 210s, 315s, 420s are portrayed in Figure 4-9. In this figure, the negative and

positive values of velocity represent the sedimentation and rise of the phases, respectively. As the process starts, the droplets are carried upwards by the oil the phase because of their high drag force. The main difference between the velocities of droplet and oil phases is in the regions where the aggregation is considerable as the droplets become bigger. On the contrary, the free phase sediments because of its high representative diameter. The two picks of free phase's velocity in Figure 4-9-a are the results of high electric fields at the two corners of the potential electrode (Figure 4-5). As the two waves of the free phase descend, they capture the droplets while getting closer together as they reach the bottom of the vessel (Figure 4-9-b-d). As the free phase accumulates at the bottom of the vessel, the gradient of its velocity decreases (Figure 4-9-c-d). This is due to the high volume fraction of secondary phase (Equation (3-4)) which increases the drag force and decrease the velocity.





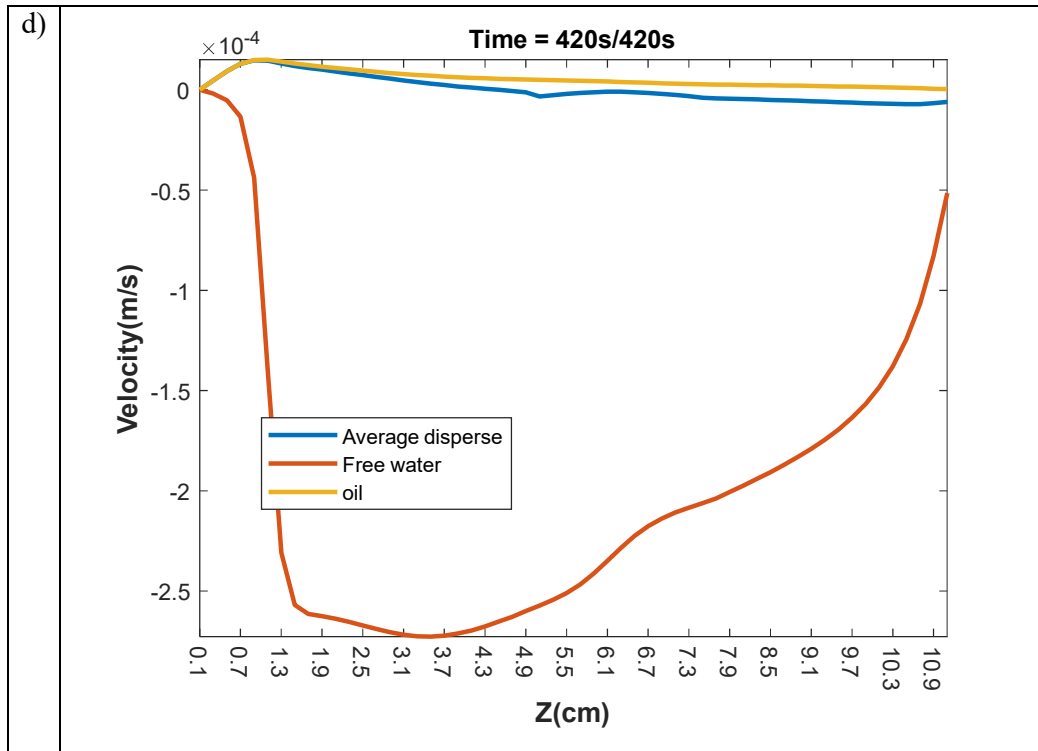
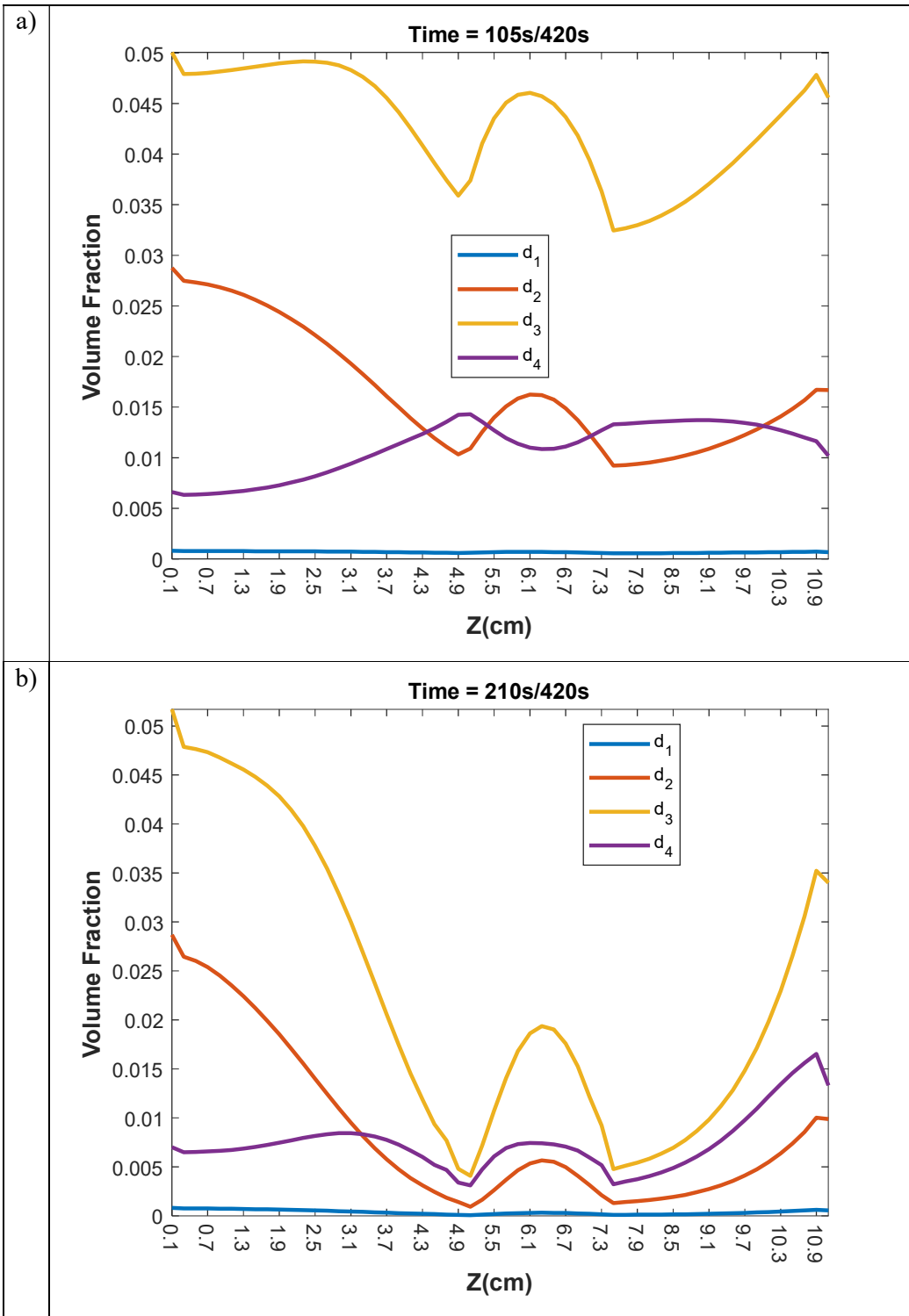


Figure 4-9: Profile of velocity of phases for the central (fifth) experimental point at a) time = 105s, b) time = 210s, c) time = 315s, d) time = 420s

The profiles of volume fractions of the droplets classes for the central (5th) experimental point at time=105s, 210s, 315s, 420s are shown in Figure 4-10. As the process starts, the aggregation of small classes of droplets increases the volume fraction of bigger droplets (Figure 4-10-a). This coalescence mainly happens in the regions between the electrodes where the electric field is stronger. The two peaks in the volume fraction of 4th class of droplets (d_4) in Figure 4-10-a is because of the higher electric fields at the two corners of the potential electrode (Figure 4-5). As the process continues, the capture of droplets becomes important. The significant decrease of the volume fraction of droplets is between the electrodes especially at the corners of the potential one where the capture has its highest rate (Figure 4-10-b). The accumulation of free phase at the bottom of the vessel decreases the volume fraction of droplets (Figure 4-10-c). Therefore, the maximum volume fraction of droplets is in the regions before the bottom of the vessel (Figure 4-10-c). Conversely, the local high volume fraction of droplets at the top of the vessel is due to the low volume fraction of free phase (Figure 4-10-c). As the process reaches its end, the sedimentation of aqueous phases slows down (Figure 4-10-d). The reason is that the main wave of free phase has reached to the bottom of the vessel and the movement of small droplets is slow.



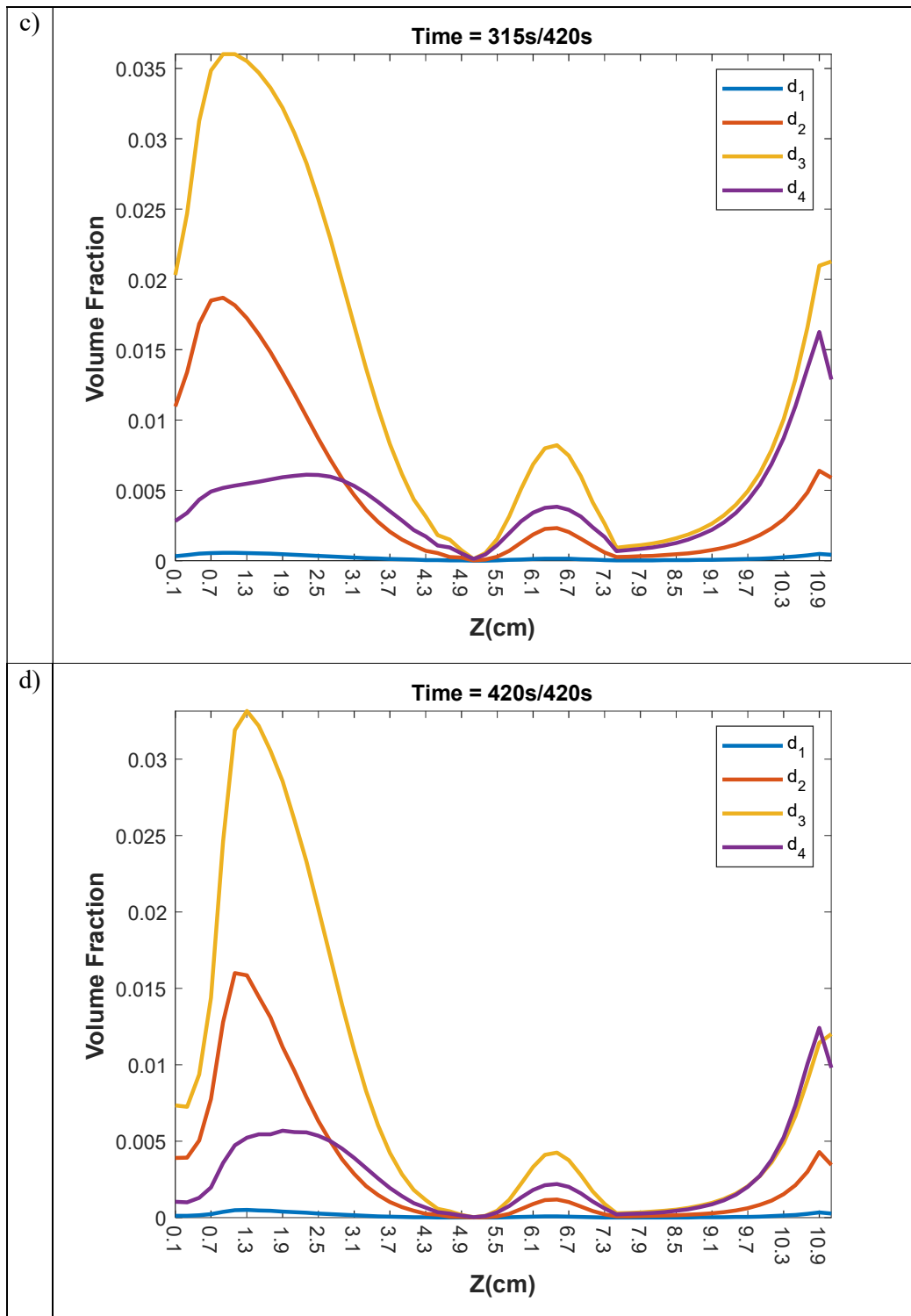
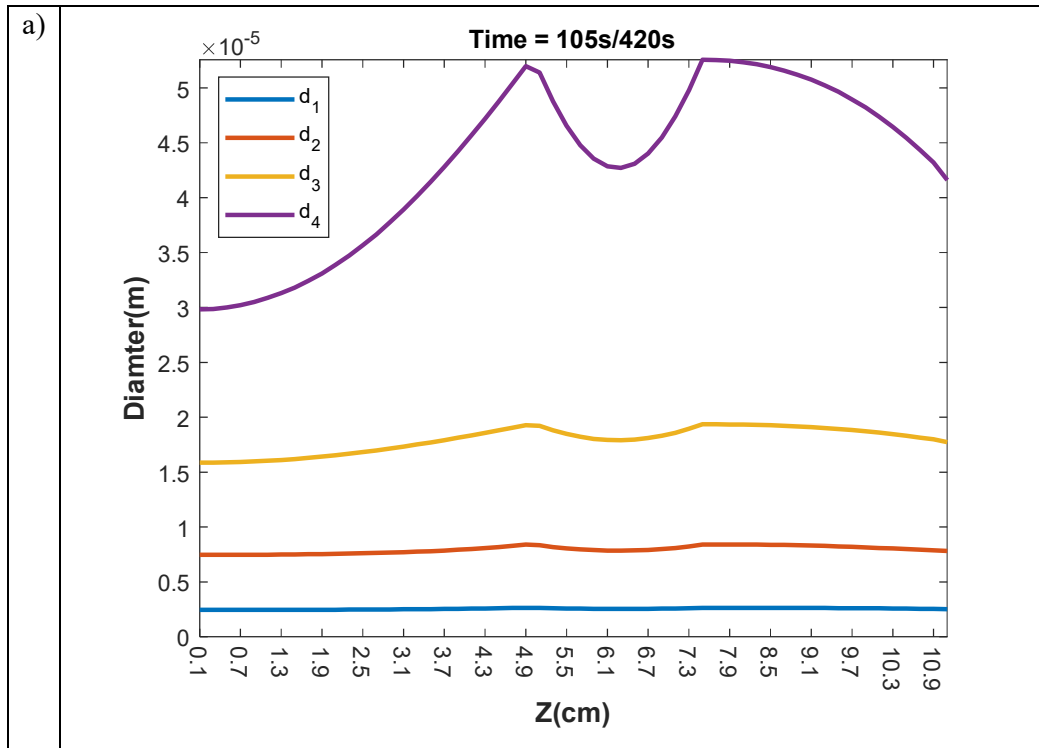
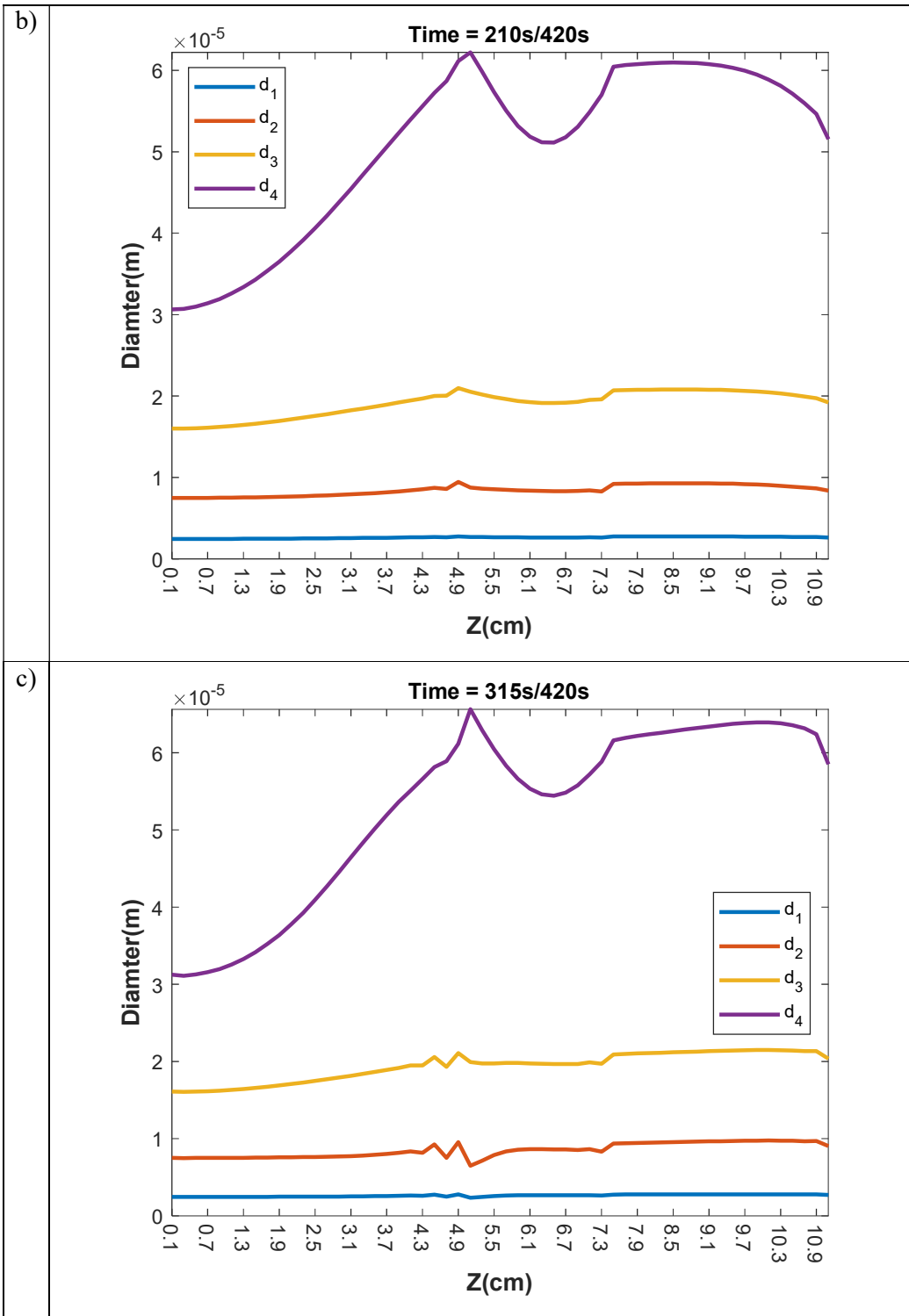


Figure 4-10: Profile of volume fraction of the droplets classes for the central (fifth) experimental point at a) time = 105s, b) time = 210s, c) time = 315s, d) time = 420s

The profiles of diameters of the droplets classes for the central (5th) experimental point at time=105s, 210s, 315s, 420s are depicted in Figure 4-11. As the process starts, the classes

of disperse water coalesce together and form bigger droplets. The increase of the diameter of droplets mainly happens in the regions between the electrodes where the electric field is high (Figure 4-11-a). The two picks of diameters in Figure 4-11-a is related to the two corners of the potential electrode where the electric field has its maximum values (Figure 4-5). As the process continues, the capture of droplets becomes significant. Therefore, the number of droplets specifically in the regions between the electrodes decreases which slows the electrocoalescence (Figure 4-11-b). On the contrary, due to low capture at the top of the vessel, the electrocoalescence makes the diameter of droplets to increase (Figure 4-11-b-d). The increase of capture specifically at the lower corner of the potential electrode causes abrupt changes in the rate of electrocoalescence. Therefore, nonsmooth behaviors can be observed through in the profiles of diameters (Figure 4-11-c-d). The smallest size of droplets (disperse water) are found at the bottom of the vessel where the electric field is weak and most droplets are captured by free phase (Figure 4-11-d). Based on the batch model (Section 3.2.1), the accumulated big droplets at the bottom of the vessel (Figure 4-3-d-2) are related to the free water phase.





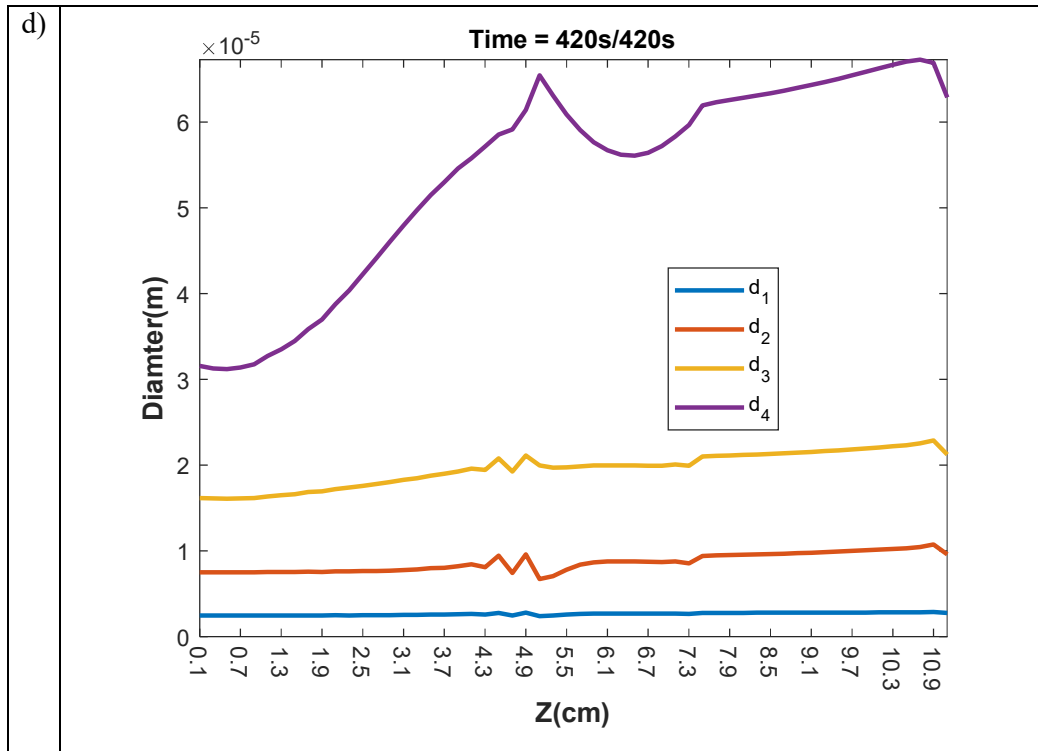
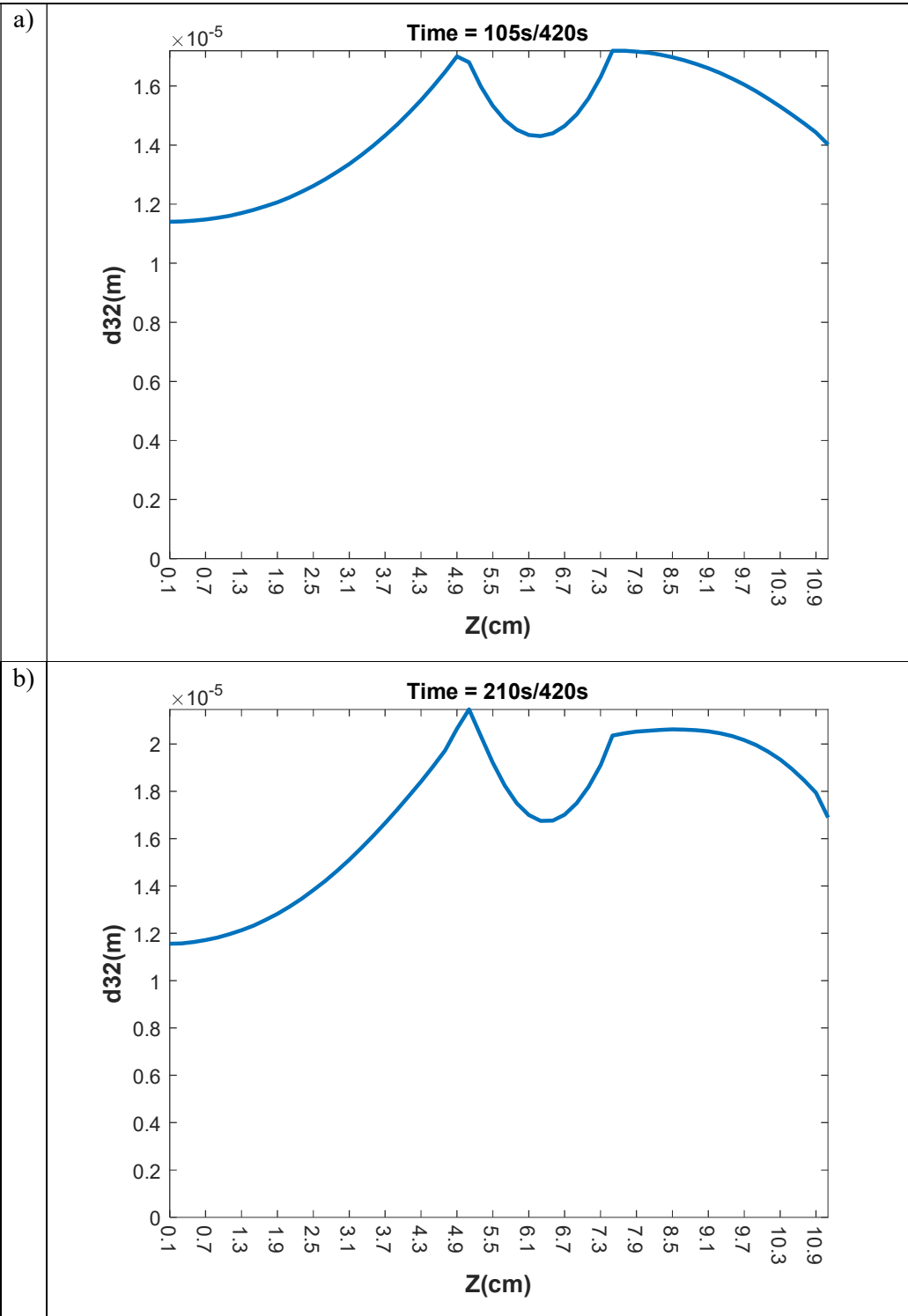


Figure 4-11: Profile of final diameter of the droplets classes for the central (fifth) experimental point at a) time = 105s, b) time = 210s, c) time = 315s, d) time = 420s

The profiles of the Sauter mean diameter of droplets classes (Equation (3-34)) for the central (5th) experimental point at time=105s, 210s, 315s, 420s are portrayed in Figure 4-12. The figure is consistent with Figure 4-11. At the beginning of the process, the maximum d_{32} is observed in the regions between the electrodes Figure 4-12-a. As the free phase captures the droplets, the rate of electrocoalescence between the electrodes decreases. Conversely, due to low capture at the top of the vessel, the d_{32} of droplets increases (Figure 4-12-b-d). The abrupt change of d_{32} is at the lower potential electrode where the electrocoalescence and capture have their highest rates.



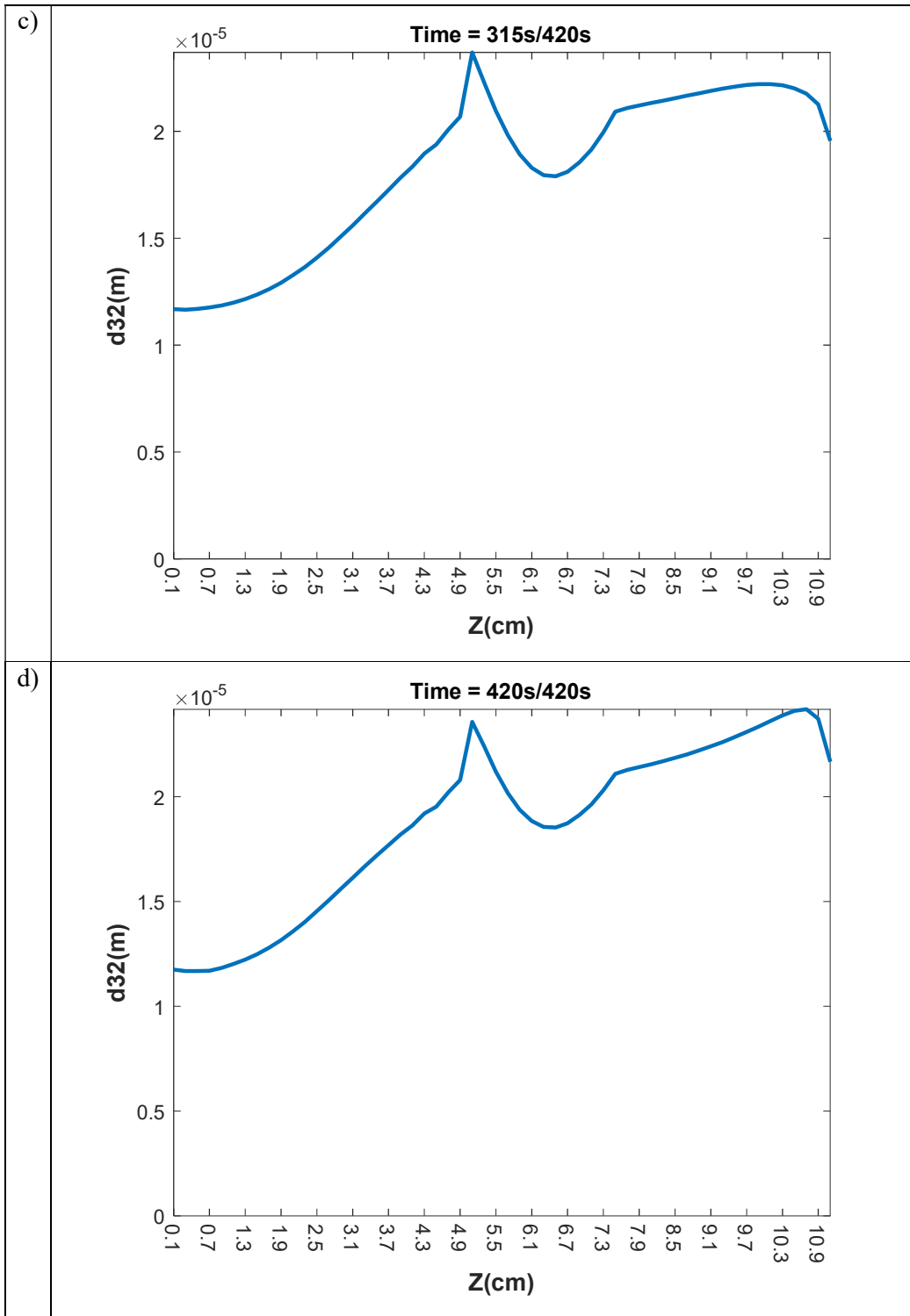


Figure 4-12: Profile of d_{32} of the droplets classes for the central (fifth) experimental point at a) time = 105s, b) time = 210s, c) time = 315s, d) time = 420s

The gif-files that display the animated profiles of BS&W, volume fraction, the velocity of phases, volume fraction/diameter of disperse phases, and d_{32} for the central (5th)

experimental point is present in the CD of the thesis (Batch Model Results\ gifs_nonsaline\ Central_5th_ Experimental_Point).

In order to compare the influence of coalescence and capture in the PBE (Equation (3-10)), the batch model was executed twice for the central experimental point while zeroing the two terms separately. Therefore, for the pure coalescence case (zero-capture), the $K_{cap,0}$, $K_{cap,E}$ were made equal to zero while using the K_{agg} of Table 4-3. Similarly, for the pure capture case (zero-coalescence) the K_{agg} was made equal to zero while using the capture coefficients of Table 4-3. The profiles of final BS&W for the central experimental point for the pure coalescence, pure capture, and coalescence-capture cases are shown in Figure 4-13. As can be seen in the figure, for the pure aggregation case, the changes of BS&W only happen in the regions between the electrode where the electric field is strong and at the top and bottom of the vessel where the oil and water accumulate, respectively. Therefore, the separation of phases could not be observed in this case. For the pure capture case, because of the high representative diameter of free phase, the separation of phases is noticeable. However, the pure capture model is not able to capture the experimental trends specifically at the top of the vessel where the capture is low. Thus, it can be concluded that the insertion of coalescence and capture terms in the PBE (Equation (3-10)) are necessary to correctly predict the batch electrocoalescence process.

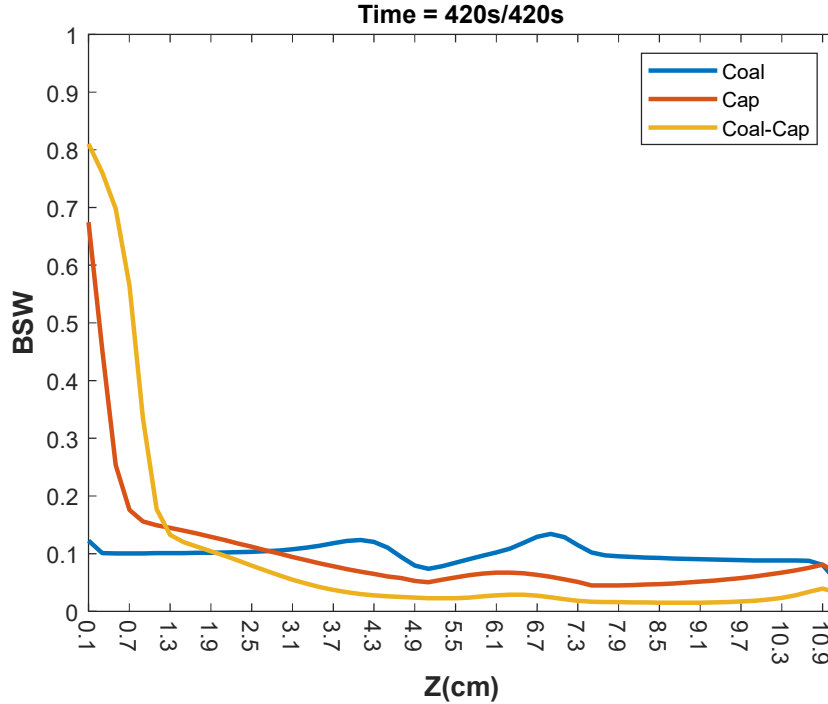


Figure 4-13: Profile of the final BS&W for the central point for pure aggregation, pure capture, and coalescence-capture cases

In order to analyze the sensitivity of estimated parameters to the initial diameter of droplets, the batch model was executed for two other distribution of droplets. Two gamma distribution of droplets with the average diameters of $d_{ave} = 5.0023 \mu\text{m}$ (Matlab command: `gampdf(:,2.5,2e-6)`) and $d_{ave} = 5.627 \mu\text{m}$ (Matlab command: `gampdf(:,2.5,2.5e-6)`) were compared to the central experimental point ($d_{ave} = 6.2517 \mu\text{m}$). The profile of final BS&W for the central experimental point with initial for the three distribution of diameters are depicted in **Figure 4-14**. As can be observed from the figure, for the regions where the electric field is high, the differences between the BS&W of three DSD are negligible. However, at the bottom of the vessel where the gradient of volume fraction is high, the differences are considerable. For example, for the initial average diameter of $d_{ave} = 5.0023 \mu\text{m}$, $d_{ave} = 5.627 \mu\text{m}$, and $d_{ave} = 6.2517 \mu\text{m}$, the final BS&Ws at the elevation of 0.8 cm (P3 in **Figure 3-4-a**) are 0.2586, 0.3507, and 0.4516, respectively.

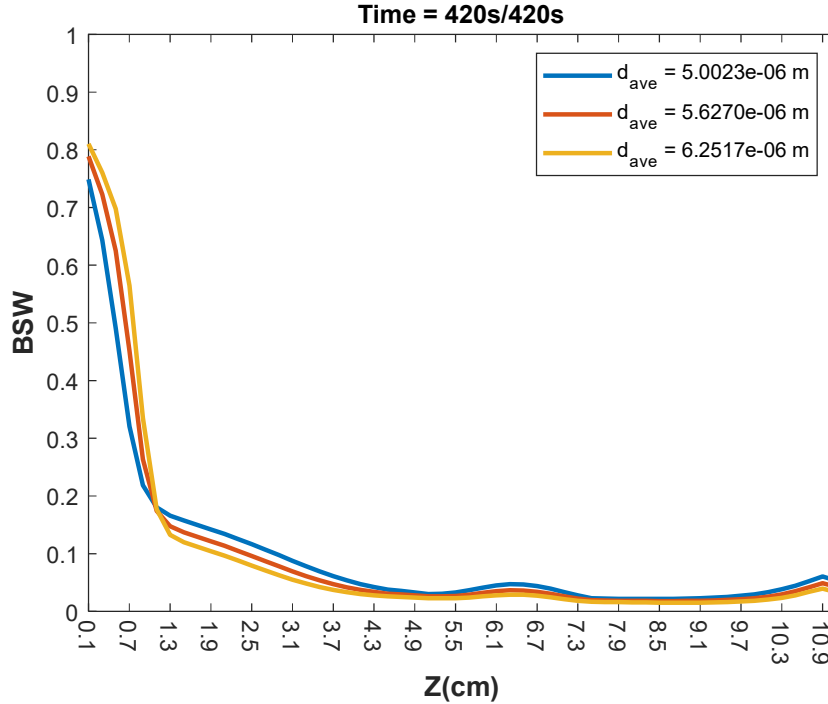


Figure 4-14: Profile of the final BS&W for the central point with initial $d_{ave} = 5.0023 \mu\text{m}$, $d_{ave} = 5.627 \mu\text{m}$, and $d_{ave} = 6.2517 \mu\text{m}$

The profiles of BS&W, volume fraction, the velocity of phases, volume fraction/diameter of disperse phases, and d_{32} for other experimental points were similar to the central experimental point. However, there are some extra details about the 1st and 3rd experimental point that worth being explained. If the volume fraction of classes of droplets approaches zero (e.g. less than $1e-5$), the moments could be unrealizable. This is principally due to the gradient term in the PBE (Equation (3-10)) [161]. In this work, this case was specifically seen for the 1st experimental point where the water content, electric field, and electrostatic time had their highest values. The profile of final volume fraction of phases for the 1st experimental point is depicted in Figure 4-15. The non-smoothness of the volume fractions specifically at the lower part of the vessel is due to the high rates of capture and sedimentation of the free phase which create high gradients in the system of equations. This behaviour could also be attributed to the numerical difficulties of the integrator when the volume fraction of droplets reaches small values. Nevertheless, it should be mentioned that for this cases the highest possible limits of computation ($\Delta t \approx 1e-5$) were used to maintain the conservation of equations. Moreover, Figure 4-15 suggests that for emulsions with more amount of water content the effect of drag force is seen for a higher elevation from the bottom of the vessel (Equation (3-4)).

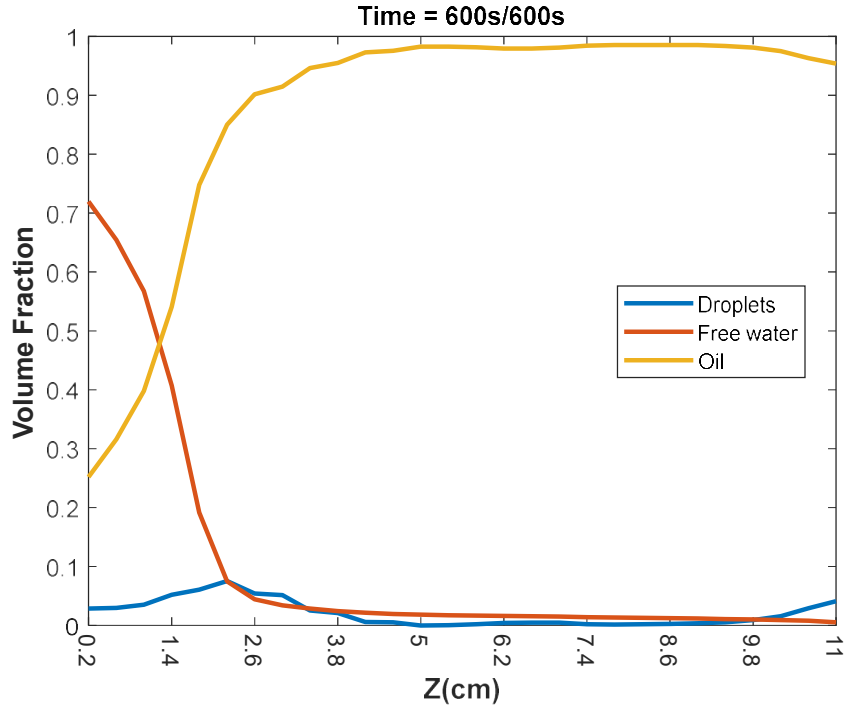


Figure 4-15: Profile of the final volume fraction of phases for the first experimental point

The quick capture of droplets at the bottom of the vessel can be better observed in Figure 4-16 where the final profile of the volume fraction of the droplets classes are portrayed. The low volume fraction of the smallest class is due to the pure aggregation characteristics of the problem. Besides, the small volume fraction of the biggest phase is due to its high capture rate (Equation (3-17)). The profile of the final diameter of the disperse phases for the 1st experimental point Figure 4-17. As the figure expresses, when the volume fraction of a phase reaches zero, its representative diameter becomes zero (meaningless). This factor causes the non-smoothness/oscillation in the profiles of volume fraction/diameter of the classes of droplets.

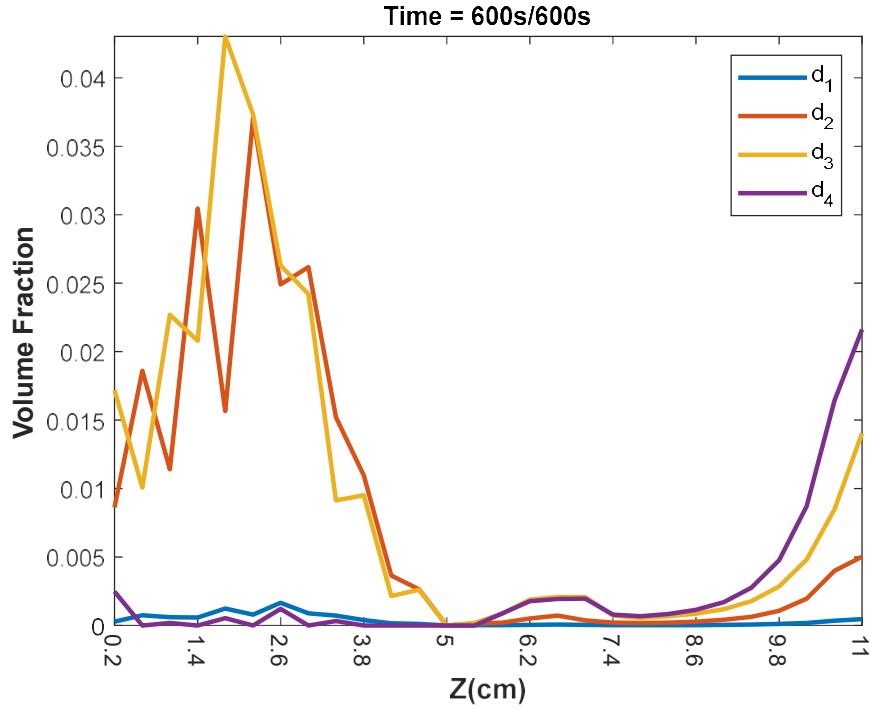


Figure 4-16: Profile of the final volume fraction of the droplets classes for the first experimental point

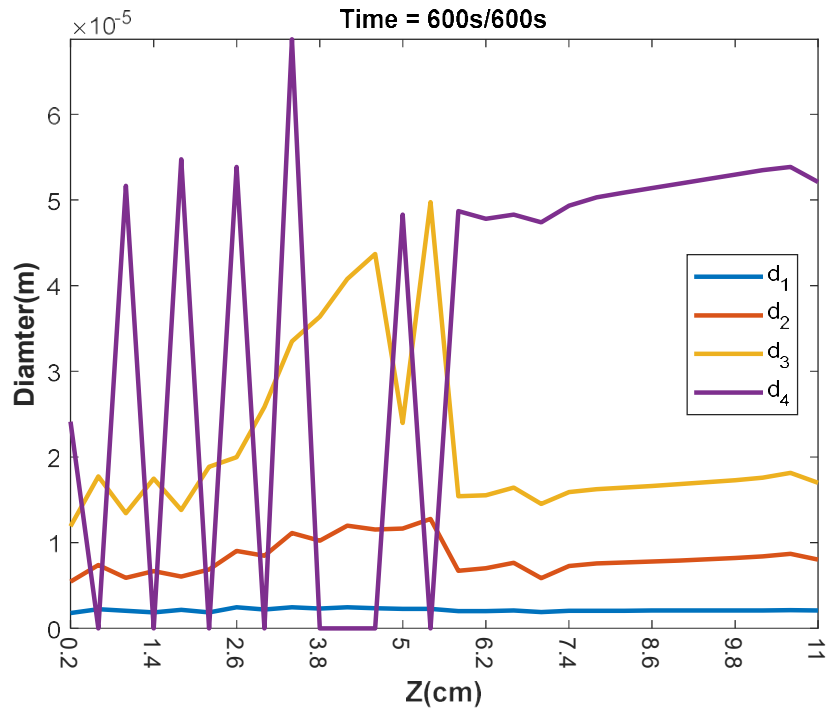
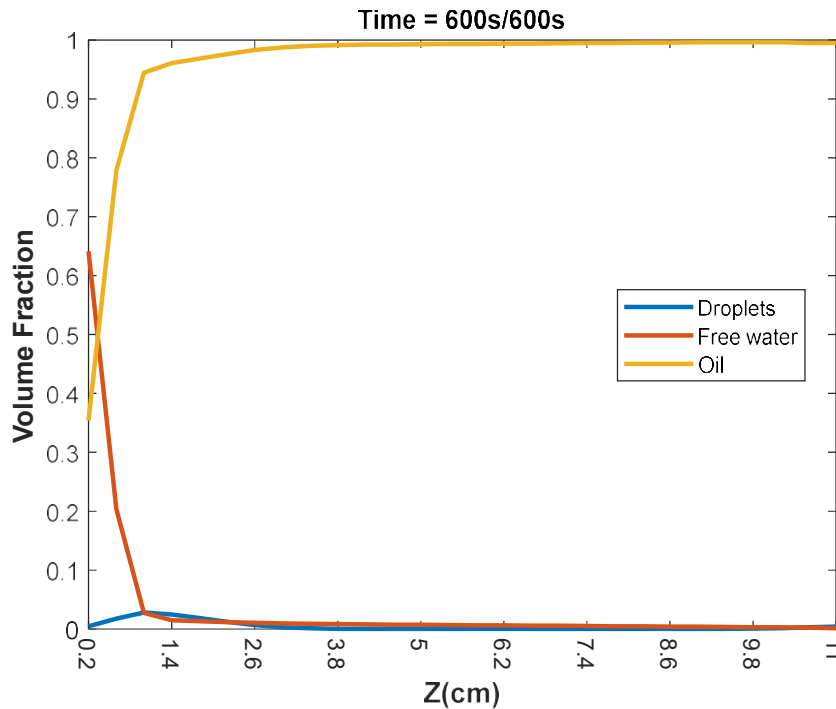


Figure 4-17: Profile of the final diameter of the droplets classes for the first experimental point

The gif-files that display the animated profiles of BS&W, volume fraction, the velocity of phases, volume fraction/diameter of disperse phases, and d_{32} for the 1st experimental point are present in the CD of the thesis (Batch Model Results\ gifs_nonsaline\ 1st_Experimental_point).

In emulsions with a low amount of water content (5%), the distance between the droplets is bigger. Thus as parameters in [Table 4-3](#) suggests, the electrocoalescence between the droplets becomes more important. Therefore, the creation of a significant amount of free phase takes more. In this work, this case was specifically seen for the 3rd experimental point. The profile of BS&W for the 3rd experimental point is shown in [Figure 4-18](#). As the figure shows, because of the high electrocoalescence at the regions between the electrodes and top of the vessel, the final volume fraction of droplets is negligible. Moreover, due to the low volume fraction of the secondary phase, the drag force was small and most of the water phases could accumulate at the bottom of the vessel. Meanwhile, it should consider that the stability of emulsions with a lower amount of water content is less.



[Figure 4-18](#): Profile of the final volume fraction of phases for the third experimental point

The profiles of volume fraction and diameter of the droplets classes for the 3rd experimental point are portrayed in Figure 4-19 and Figure 4-20, respectively. The figures verify that in this experimental point, the capture of droplets specifically at the two corners of the potential electrode (Figure 4-6-a) is not sharp and the droplets have more time to coalesce together.

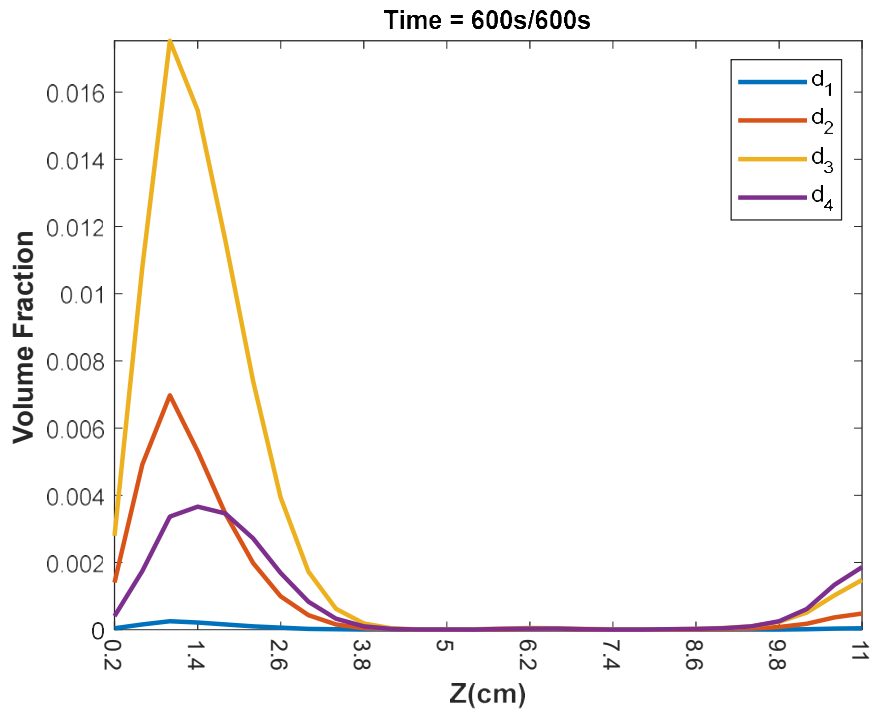


Figure 4-19: Profile of the final volume fraction of the droplets classes for the third experimental point

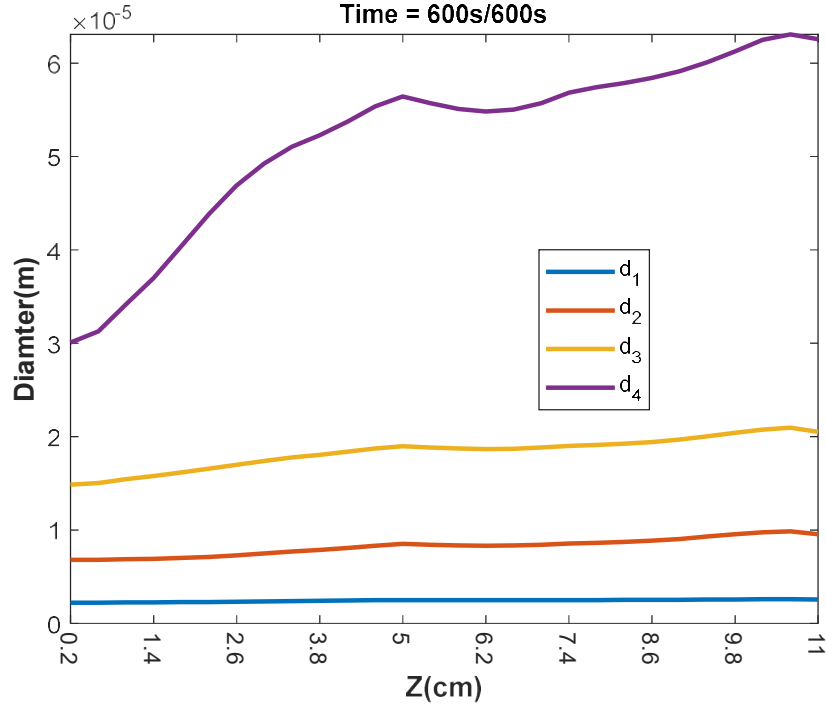


Figure 4-20: Profile of the final diameter of the disperse phases for the third experimental point

The gif-files that display the animated profiles of BS&W, volume fraction, the velocity of phases, volume fraction/diameter of disperse phases, and d_{32} for the 3rd experimental point are present in the CD of the thesis (Batch Model Results\ gifs_nonsaline\ 3rd_Experimental_point).

4.1.6. Estimation of Batch Model Parameters for Saline Emulsions

In this section, the results of parameter estimation for saline emulsions are presented. As explained in Section 4.1.4, in this work, the addition of 3.5% w/w of NaCl to the aqueous phase in the water-in-Exxsol emulsion enhanced the separation of phases in electrocoalescence. The values of estimated parameters are presented in Table 4-5. The table shows that in most experimental points, the capture and aggregation coefficients are greater than the values calculated for non-saline emulsions (Table 4-3). Although it should consider that for saline emulsions especially the ones with low water content, the stability was questionable (Table 4-2).

Table 4-5: Values of estimates parameters for saline emulsion

| Experiment | $K_{cap,0}$ | $K_{cap,E}$ | K_{agg} |
|----------------------------|-------------|-------------|-----------|
| 1,7 (BS&W=15%, V0=8kV) | 3.9755e7 | 3.9160e3 | 5.02e-9 |
| 6,9 (BS&W=15%, V0=4kV) | 1.4395e7 | 1.0726e3 | 1.05e-8 |
| 2,4 (BS&W=5%, V0=4kV) | 6.3667e7 | 8.782e3 | 4.98e-8 |
| 10,3 (BS&W=5%, V0=8kV) | 7.7180e7 | 8.5738e3 | 1.76e-8 |
| 5,8,11 (BS&W=10%, V0=6kV) | 5.3644e7 | 5.0510e3 | 11.28e-8 |

The calculated and experimental values of the BS&W for all 11 experimental points for saline emulsions are presented in [Table 4-6](#).

Table 4-6: Calculated and experimental values of BS&W for saline emulsion

| Experiment | d_ave (μm) | P1-Exp | P1-Cal | P2-Exp | P2-Cal | P3-Exp | P3-Cal | BS&W-Error |
|------------|------------|--------|--------|--------|--------|--------|--------|------------|
| 1 | 5.7 | 0.32 | 0.57 | 0.72 | 2.28 | 92.97 | 80.04 | 7.52 |
| 7 | 5.9 | 0.61 | 2.64 | 0.90 | 26.47 | 94.24 | 46.84 | 30.1 |
| 6 | 5.2 | 0.86 | 3.18 | 1.00 | 19.60 | 51.66 | 56.01 | 11.13 |
| 9 | 5.8 | 9.80 | 13.05 | 9.87 | 16.68 | 9.63 | 15.01 | 5.35 |
| 2 | 6.2 | 0.84 | 1.29 | 5.92 | 6.35 | 0.44 | 11.25 | 6.25 |
| 10 | 6 | 0.53 | 1.35 | 0.64 | 6.03 | 4.52 | 10.67 | 4.74 |
| 3 | 5.8 | 0.49 | 0.33 | 0.95 | 1.21 | 1.79 | 2.29 | 0.34 |
| 4 | 5.6 | 0.53 | 0.29 | 0.64 | 1.33 | 1.79 | 3.16 | 0.89 |
| 5 | 6.1 | 0.63 | 0.92 | 0.52 | 3.95 | 67.21 | 67.34 | 1.99 |
| 8 | 5.1 | 0.68 | 1.33 | 0.36 | 5.9 | 52.32 | 54.19 | 3.44 |
| 11 | 4.6 | 0.48 | 1.66 | 0.66 | 7.42 | 42.57 | 44.21 | 4.07 |

[Table 4-6](#) shows that the model has a proper performance in predicting the behavior of batch electrocoalescence. Nevertheless, there are differences between the calculated and experimental values. The explanations about the experimental and modeling errors are presented in [Section 4.1.5](#).

The behavior of the batch model for saline emulsions was similar to [Section 4.1.5](#). The gif-files that display the animated profiles of BS&W, volume fraction, the velocity of phases, volume fraction/diameter of disperse phases, and d_{32} for the 1st, 3rd, and central

(5th) experimental point of saline emulsions are present in the CD of the thesis (Batch Model Results\ gifs_saline).

The conceptual error that is observable in [Table 4-6](#) and the gif-files is that the model is not able to predict the values of BS&W that are greater than 87%. In this work, the polydisperse Eulerian-Eulerian model was employed to predict the separation of phases in the electrocoalescence process. The fundamental assumption of the model is that the secondary phase is always disperse and it is represented by a diameter. However, if the amount of separation in the electrocoalescence passes certain limits (e.g. >90%), the water phase could, in fact, create a continuous phase. This can be considered as the point where the polydisperse Eulerian model fails. In this study, due to the mathematical form of drag coefficient factor ([Equation \(3-4\)](#)), the maximum amount of water volume fraction could not pass 87%. This can be considered as a deficiency/shortcoming of the proposed model. A premature way to solve the issue is to increase the d_{max}^{III} in [Equation \(3-8\)](#). However, considering a very big value as a diameter of a droplet (e.g. >1000 μ) is not logical/feasible. An intelligent way to overcome this limitation could be to provide a model that can switch between polydisperse and VOF (volume of fluid) model based on specific criterions. Based on our knowledge this model has not been developed (at least for the electrocoalescence process) in the literature and could be a novelty for future research.

4.2. Evaluation of Continuous Pilot Plant Simulations

In this work, our initial intention was to simulate the 11 experimental points of the work of Assenheimer et al. [[169,170](#)]. However, in their study, decent amounts of separation/segregation of phases were not reached in all experimental points. Therefore, instead of simulating all cases, we decided to perform a sensitivity analysis on the operational conditions at the central experimental point [[169,170](#)].

The profile of electric field in the vessel implemented in the Ansys Fluent software [[96](#)] is shown in [Figure 4-21](#).

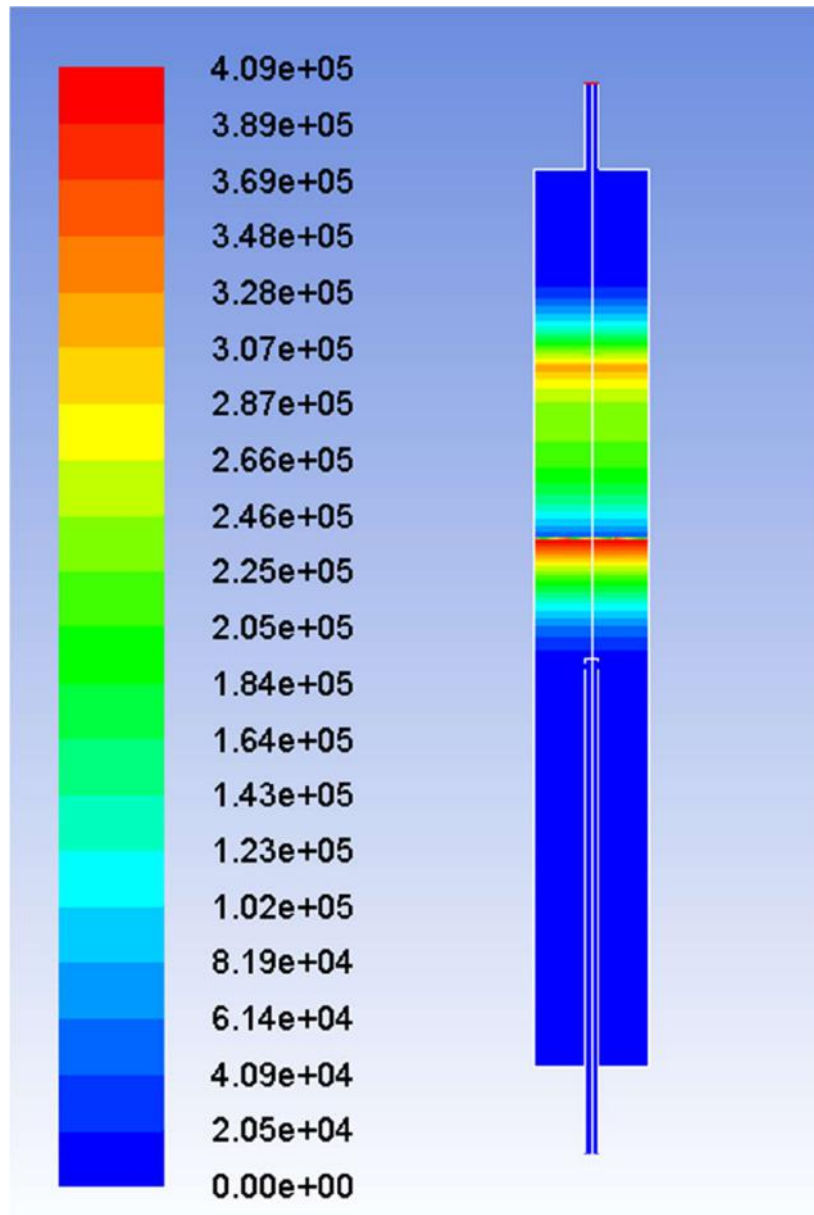


Figure 4-21: Contour of DC electric field inside the vessel for $V_0=3\text{kV}$ (central experimental point in the work of Souza [169])

As can be observed in Figure 4-21, similar to the batch electrocoalescer (Figure 3-2, Figure 4-5), the maximum amounts of electric field are at the two corners of the potential electrode (Figure 3-13, Figure 3-15) where the gradient of voltage ($E = -\nabla \phi$ [158]) is higher. Nevertheless, it should consider that unlike the batch electrostatic vessel, there are regions inside the continuous electrostatic vessel where the electric field is zero.

In this work, the sensibility of simulations to the aggregation/capture parameters (

K_{agg} , $K_{cap,0}$, and $K_{cap,E}$ in Section 3.2) and the initial diameter of W/O emulsion at the central experimental point of the work of Souza [169] was analyzed. The cases of simulation are presented in Table 4-7. The time of simulations was 15 minutes, the time step size was 0.1s, and the time stepping method was iterative with the minimum time step of 0.001s [96].

Table 4-7: Cases of simulation

| Run | d_{ave} (μm) @inlet | d_{32} (μm) @inlet | K_{agg} | $K_{cap,0}$ | $K_{cap,E}$ |
|-----------------|---------------------------------------|--------------------------------------|-----------|-------------|-------------|
| 1 (saline) | 5.0 | 9.0 | 1.18e-8 | 5.3644e7 | 5.0510e3 |
| 2 (non-saline) | 5.0 | 9.0 | 1e-8 | 3.3649e7 | 2.2621e3 |
| 3 (half-saline) | 5.0 | 9.0 | 1.09e-8 | 4.3647e7 | 3.6566e3 |
| 4 (half-saline) | 4.0 | 7.2 | 1.09e-8 | 4.3647e7 | 3.6566e3 |
| 5 (half-saline) | 6.0 | 10.8 | 1.09e-8 | 4.3647e7 | 3.6566e3 |

The 1st and 2nd cases in Table 4-7 utilize the parameters that were estimated for the saline and non-saline emulsions with 10 water% w/w, respectively (Table 4-5, Table 4-3). The half-saline case in Table 4-7 uses the average value of the non-saline and saline cases parameters. It should be mentioned that in the batch experiments, the saline emulsion was prepared by adding 3.5% w/w of NaCl to the aqueous phase. While in the study of Souza [169], the 10 water w/w% saline emulsion was made by adding 0.18 salt% w/w to the aqueous phase. Therefore, it is not possible to quantitatively compare the central point of the work of Souza [169] with the cases considered in simulations (Table 4-7). However, we expect that the result of the 4th case simulation (Table 4-7) be consistent with the central experimental point ($d_{ave} = 4\mu\text{m}$) of the work of Souza [169]. In this section, the gamma distribution function was used to determine the DSDs with the average diameters of $d_{ave} = 4.0\mu\text{m}$ (Matlab command: `gampdf(:,2.5,1.6e-6)`), $d_{ave} = 5.0\mu\text{m}$ (Matlab command: `gampdf(:,2.5,2e-6)`), and $d_{ave} = 6.0\mu\text{m}$ (Matlab command: `gampdf(:,2.5,2.4e-6)`).

In this work, in order to examine the mesh convergence, the profile of area-weighted average (ANSYS 2016a) of water volume fraction at the bottom of the vessel for the first 3 minutes of the 3rd simulation case (Table 4-7) was determined for the two meshes (Table 3-4). The results of the three simulations are shown in Figure 4-22.

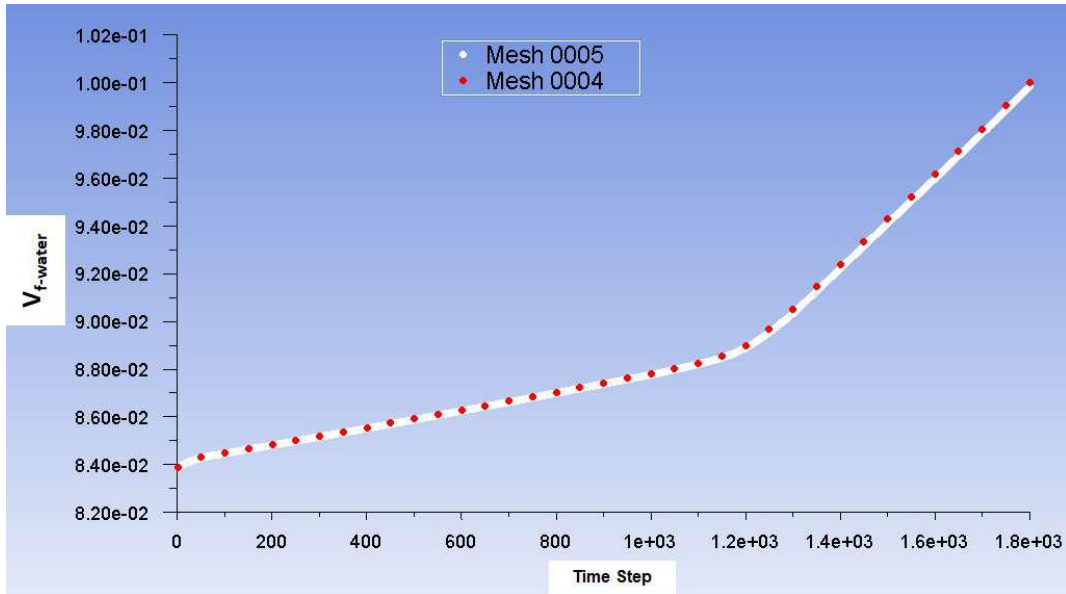


Figure 4-22: Examination of mesh convergence using the 3rd simulation case (Timestep = 0.1s)

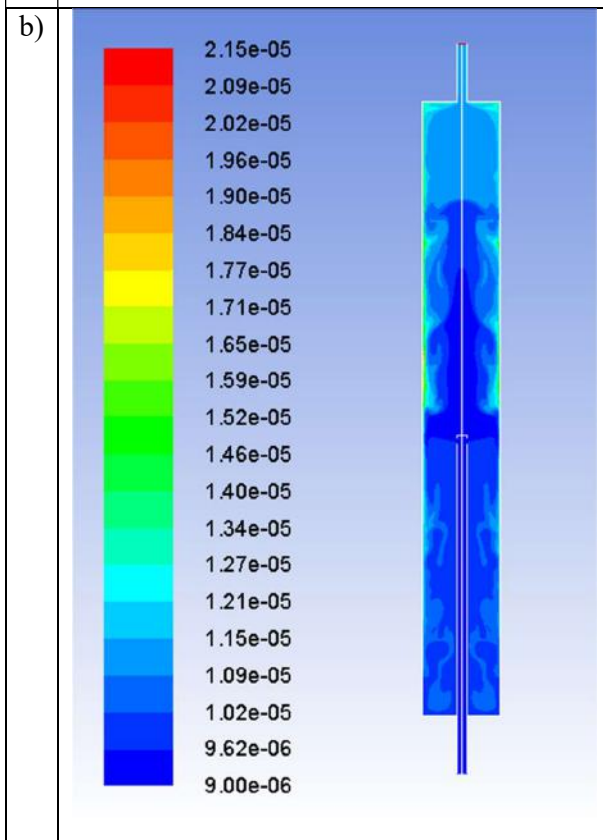
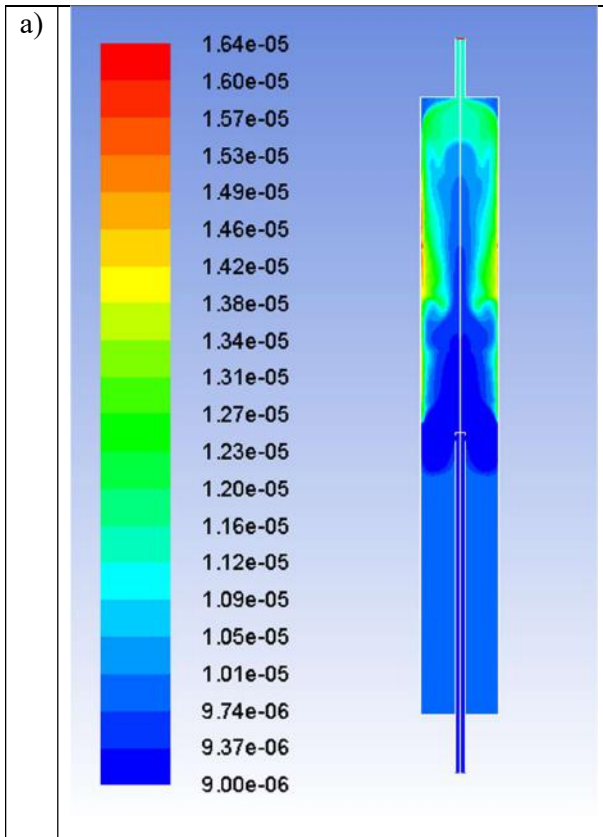
Figure 4-22 shows that for the two meshes, the profiles of water volume fraction at the bottom of the vessel are consistent. Therefore, in this work, in order to reduce the computational cost, the simulations were performed using the 1st Mesh (Table 3-4). The results of the simulation cases (Table 4-7) are presented in Table 4-8.

Table 4-8: Results of simulation cases

| Run | d _{ave} (μm) @inlet | d ₃₂ (μm) @inlet | v _{f_water} @outlet | d ₃₂ (μm) @outlet | v _{f_water} @bottom |
|-----------------|---------------------------------|--------------------------------|---------------------------------|---------------------------------|---------------------------------|
| 1 (saline) | 5.0 | 9.0 | 0.045 | 11.01 | 0.88 |
| 2 (non-saline) | 5.0 | 9.0 | 0.068 | 13.8 | 0.85 |
| 3 (half-saline) | 5.0 | 9.0 | 0.047 | 16.4 | 0.865 |
| 4 (half-saline) | 4.0 | 7.2 | 0.075 | 9.04 | 0.79 |
| 5 (half-saline) | 6.0 | 10.8 | 0.054 | 16.3 | 0.87 |

In the batch model (Sections 4.1.5-6), it was seen that the separation of phases enhances by the increase of aggregation/capture coefficients. Moreover, it was observed that for a higher average diameter of initial emulsion, the segregation of phases is more. However, Table 4-8 shows that the results of simulation cases are not consistent with the findings

of the batch model in all points. This can be attributed to the characteristic of the continuous process. Therefore, it is important to understand the phenomena happen during the continuous electrocoalescence. **Figure 4-26** portrays the contour of d_{32} of droplets for the 3rd simulation case at times = 3.75min, 7.5min, 11.25min, and 15min. **Figure 4-26-a** shows that as droplets get bigger they migrate to the regions close to the wall of the vessel. In the absence of electric field, small droplets are carried upwards by the oil phase because of the high drag force (**Equation (3-3)**). The carriage of small droplets by oil phase happens especially at the center of the vessel where the rising velocity is higher. Here it is worth to mention that the flow is laminar and the velocities of phases are small. As the electrocoalescence and capture happen, big droplets are created that have small drag coefficients (**Equation (3-3)**). Therefore, the drag force that makes the droplets move with the oil phase decreases. Consequently, the bigger droplets migrate to the regions close to the wall of the vessel where the velocity of oil phase is smaller. Meanwhile, it should consider that due to the high drag force in regions with high water content (**Equation (3-4)**), the separation of bigger droplets at the regions close to the wall is not explicit. In continuation, because of the higher density of water phase, the bigger droplets move towards the bottom of the vessel from the regions close to the wall of the vessel (**Figure 4-26-b**). When big droplets reach to the regions below the feeder they start to move towards the center of the vessel where the velocity of oil phase is not high. Ultimately, the water phases reach the bottom of the vessel and accumulate.



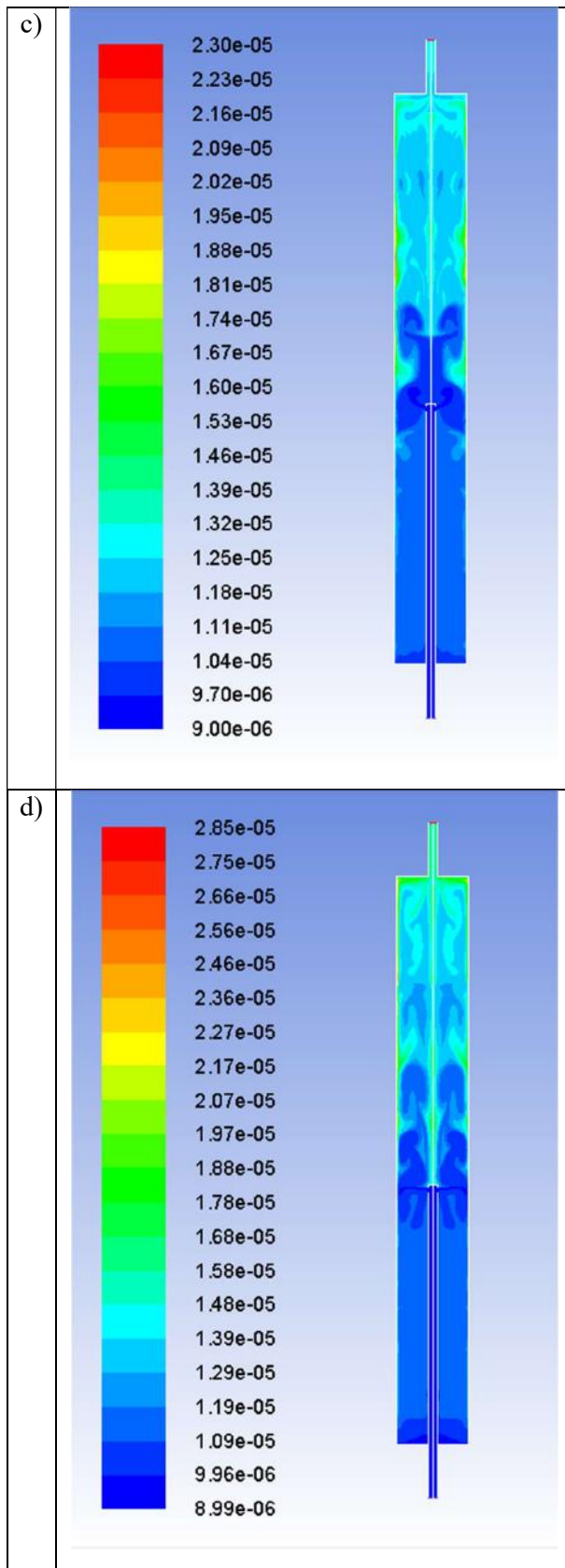
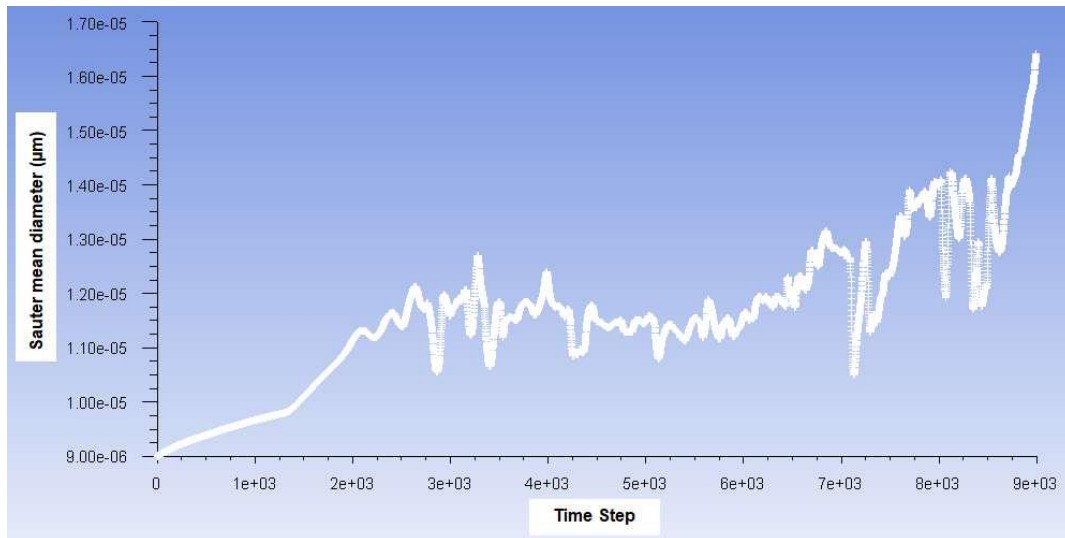


Figure 4-23: Contour of the d_{32} of the droplets for the 3rd simulation case at a) time = 3.75min, b) time = 7.5min, c) time = 11.25min, d) time = 15min

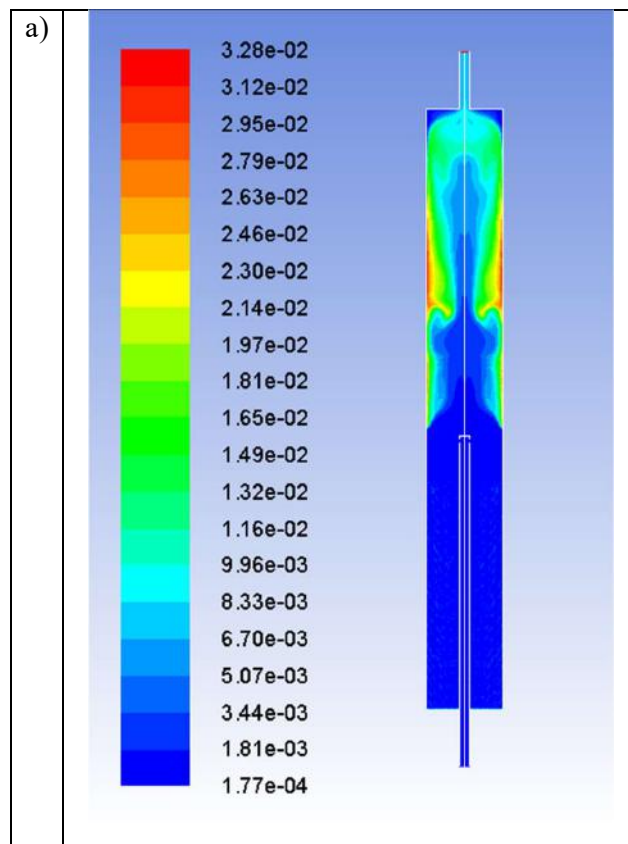
The MPEG-file that displays the animated contour of d_{32} of droplets for the 3rd simulation case is present in the CD of the thesis ([Continuous Simulation Results/Run3](#)). The video shows that the formation of big droplets and their movement inside the vessel happen in disordered bulks ([Figure 4-26-c-d](#)). This is due to the interaction between the momentum of untreated W/O emulsion entering the electrostatic vessel and the formation of big water droplets that tries to overcome the drag force and descend. The creation of big water phases happens in two waves that are attributed to the high electric fields at the two corners of the potential electrode ([Figure 4-21](#)). Therefore, it is expectable to observe variations in the d_{32} of droplets at the outlet of the vessel. The profile of area-weighted average ([ANSYS 2016a](#)) of d_{32} of droplets for the 3rd simulation case at the outlet of the continuous electrostatic vessel is portrayed in [Figure 4-24](#).

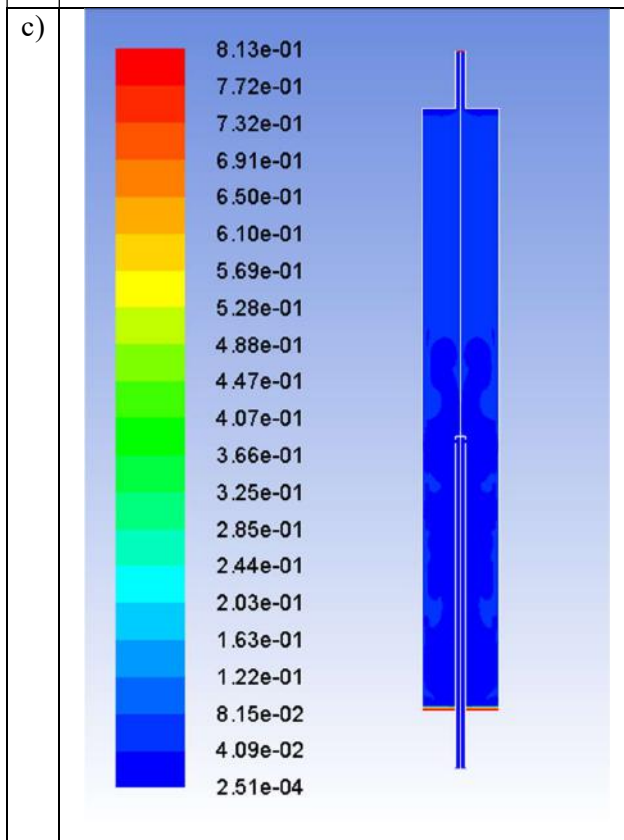
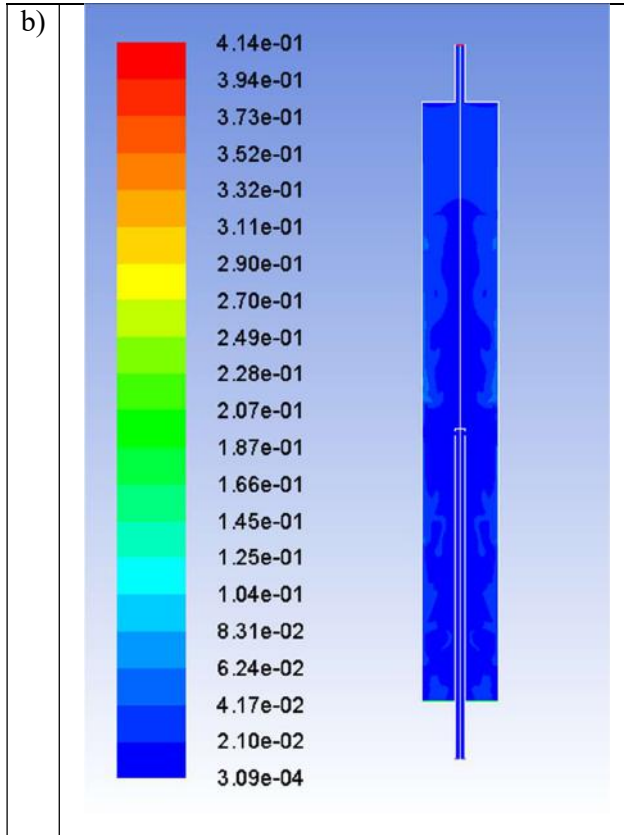


[Figure 4-24](#): Profile of area-weighted average of d_{32} of droplets for the 3rd simulation case at the outlet of the vessel (Timestep = 0.1s)

[Figure 4-24](#) shows the oscillations of d_{32} at the outlet of the vessel. Here, it is not possible to confirm the variations of d_{32} in the figure as in the work Souza [169], the diameter of droplets was not measured at different times. However, the possible error of [Figure 4-24](#) can be attributed to several factors. In this work, a one-dimensional electric field was considered inside the vessel. While in reality, the electric field is three-dimensional. Moreover, in this work, it was considered that the breakage of droplets does not happen. While in practice, at the surface of electrodes where the electric field is high, the droplets could break. Nevertheless, we expect to observe oscillations of the d_{32} of droplets at the outlet of the electrostatic vessel.

The contour of free water volume fraction for the 3rd simulation case at times = 3.75min, 7.5min, 11.25min, and 15min is depicted in Figure 4-25. The highest rate of capture of droplets is at the regions close to electrodes where the electric field and aggregation of droplets are high. Similar to the contour of d_{32} of droplets, Figure 4-25-a shows that the big droplets of free water migrate to the regions close to the wall of the vessel. As the volume fraction of free phase increases, it overcomes the drag force and moves downward while capturing water droplets (Figure 4-25-b). As the free phase reaches the region below the feeder it starts to move toward the center of the vessel where the velocity of oil phase is low.





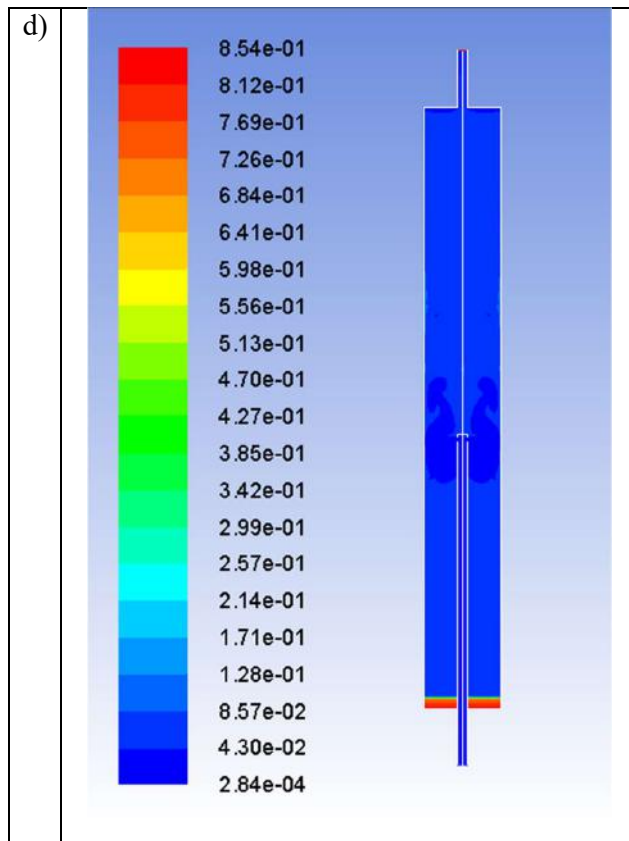
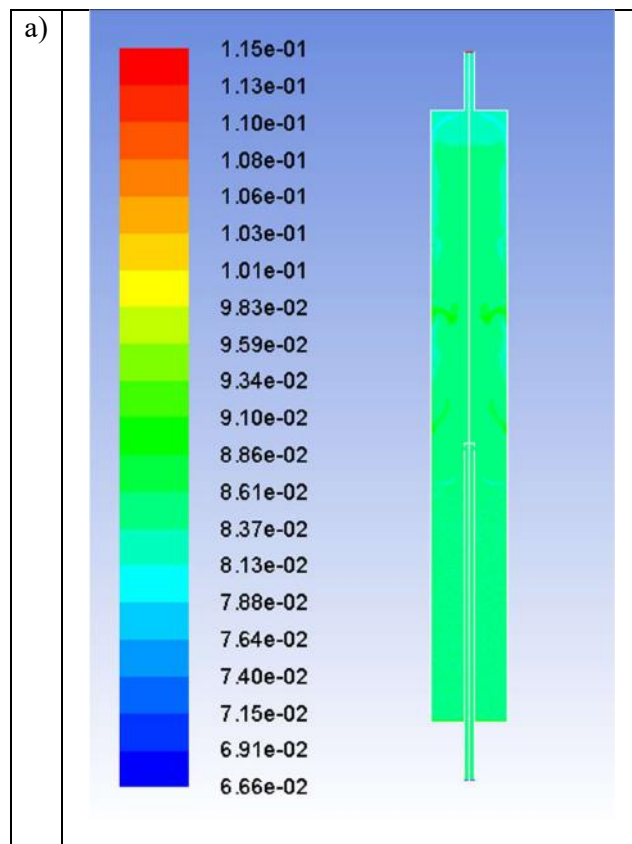


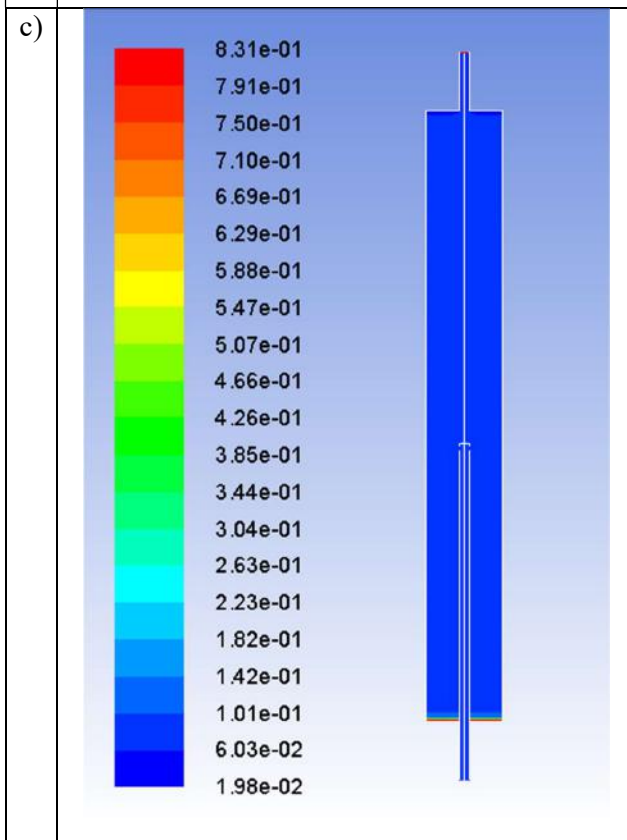
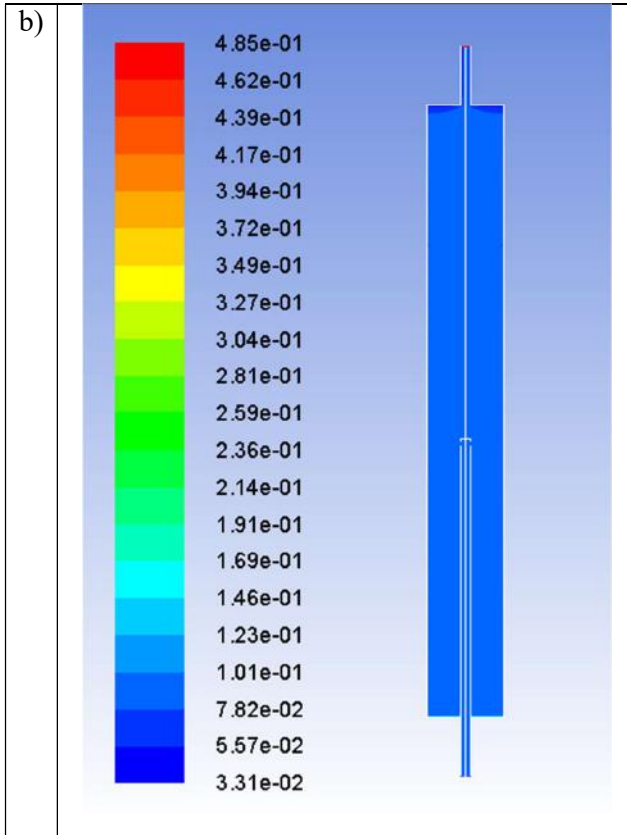
Figure 4-25: Contour of free water volume fraction for the 3rd simulation case at a) time = 3.75min, b) time = 7.5min, c) time = 11.25min, d) time = 15min

The MPEG-file that displays the animated contour of free water volume fraction for the 3rd simulation case is present in the CD of the thesis (Continuous Simulation Results/Run3). As the process continues and the free water reaches the bottom of the vessel, continuous disordered bulks of free phase are created mainly in the regions close to the wall along the height of the vessel (Figure 4-25-c). Similar to the contour of d_{32} , the disordered capture of droplets can be accredited to the time it takes for new waves of free water to be created. The free phase accumulates at the bottom of the vessel where it composes most of the volume fraction of water (Figure 4-25-d).

The contour of water volume fraction for the 3rd simulation case at times = 3.75min, 7.5min, 11.25min, and 15min is portrayed in Figure 4-26. The figure is consistent with the two previous contours (Figure 4-24, Figure 4-25). The MPEG-file that displays the animated contour of water volume fraction for the 3rd simulation case is present in the CD of the thesis (Continuous Simulation Results/Run3). As the process starts, the volume fraction of water at the two corners of the potential electrode where the electric field is high increases. The accumulated water in the regions with high electric field is partially

carried upward by the oil phase while simultaneously moving toward the wall of the vessel and descend (Figure 4-26-a). The special form of the accumulated water contour at the lower corner of the potential electrode in Figure 4-26-a is due to the radial distribution of untreated WO emulsion at the feeder. As the water phases reach to the bottom of the vessel and accumulate, they start to create a continuous disordered bulk of water created inside the vessel (Figure 4-26-b). As the created bulk spreads inside the entire vessel, the rate of capture and coalescence of W/O emulsion increases. Therefore, the volume fraction of water along the entire height of the vessel decreases while accumulating at the bottom of the vessel. (Figure 4-26-c).





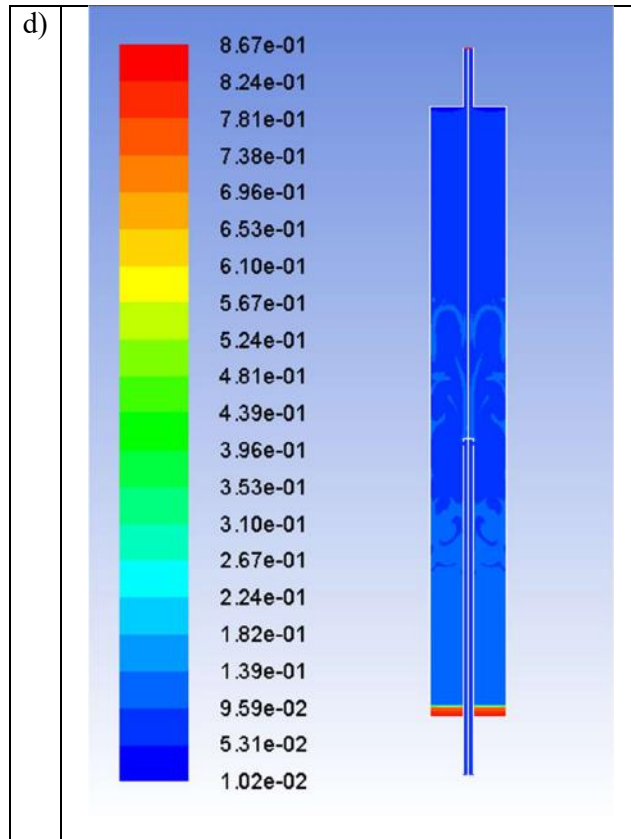


Figure 4-26: Contour of water volume fraction for the 3rd simulation case at a) time = 3.75min, b) time = 7.5min, c) time = 11.25min, d) time = 15min

As the process continues, new disordered water waves are created and move toward the bottom of the vessel (Figure 4-26-d). The profile of area-weighted average (ANSYS 2016a) of water volume fraction for the 3rd simulation case at the bottom of the continuous electrostatic vessel is depicted in Figure 4-27. The sharp increase of water content at the bottom of the vessel is related to the time when the main wave of free water reaches to the bottom of the vessel and a continuous (disordered) bulk of free phase is created along the height of the vessel.

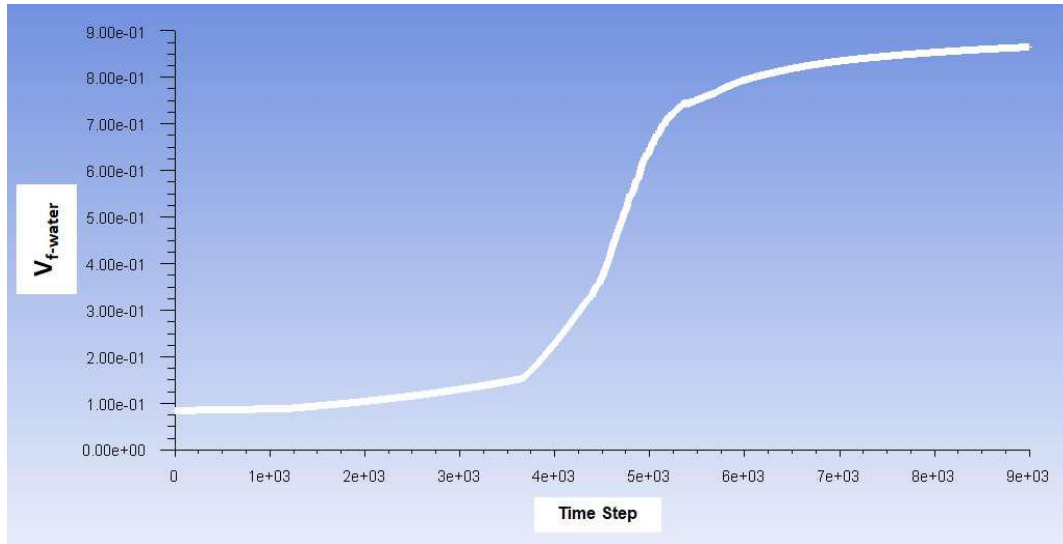


Figure 4-27: Profile of area-weighted average of water volume fraction for the 3rd simulation case at the bottom of the vessel (Timestep = 0.1s)

As discussed in [Section 4.1.6](#), in this work, the water volume fraction at the bottom of the vessel did not pass 87%. This is due to the mathematical form of the [Equation \(3-4\)](#) and can be considered as a shortcoming of the proposed model that cannot switch to VOF multiphase approach if certain criterion is reached ([Section 4.1.6](#)).

The profile of area-weighted average ([ANSYS 2016a](#)) of water volume fraction for the 3rd simulation case at the outlet of the continuous electrostatic vessel is shown in [Figure 4-28](#). The figure shows that as the electrocoalescence proceeds, the volume fraction of water at the outlet of the vessel decreases. This is because of the creation of a disordered continuous bulk of water phases along the whole height of the vessel that enhances the separation. Meanwhile, as aforementioned, there is an interaction between the momentum of the oil phase and the formation of big droplets. Therefore, as seen in [Figure 4-28](#), the profile of the water volume fraction at the outlet of the vessel demonstrates oscillations.

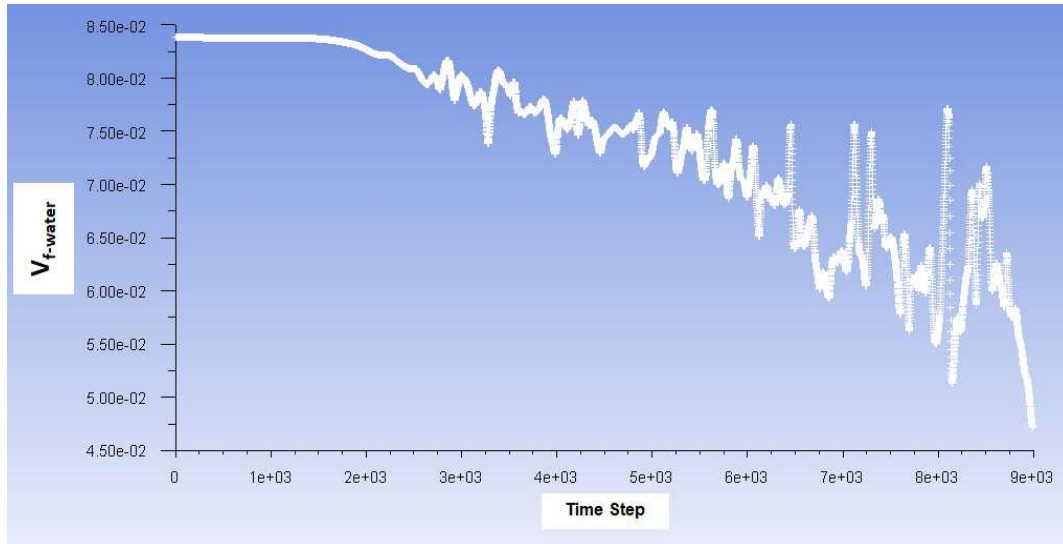


Figure 4-28: Profile of area-weighted average of water volume fraction for the 3rd simulation case at the outlet of the vessel (Timestep = 0.1s)

Here, the possible errors of the simulations are discussed. As explained before, the conceptual error of the simulations is due to the inability of the proposed model to switch between polydisperse and VOF Eulerian models for the secondary phase. The other fundamental error of the simulations can be attributed to the assumptions/simplifications made to develop the proposed model. In this work, the 3D geometry of the electrostatic vessel was simulated by an axisymmetric model. Moreover, the presence of electrodes was not considered. Besides, the possible breakage of droplets on the surface of electrodes where the electric field is high was not examined. The numerical errors of the simulations are due to the time/spatial discretization and the wide range of values (specifically moments) that the Ansys Fluent (R) software should handle. There are two numerical points about the Ansys Fluent (R) software [96] that worth being explained. The dynamic integrator of the software is based on the Euler method. However, in this work, the more advanced Dasslc [167] and ode15s (MathWorks) integrators were employed to solve the batch model and estimate the parameters. Moreover, the QMOM implementation of the software has its own moment realizability check and inversion methods (PD algorithm (Gordon, 1968)) which are different from the ζ_k -Wheeler algorithm [163] employed in the batch modeling.

Nomenclature

| | |
|-----------|-------------------------|
| d | diameter of droplet (m) |
| d_{32} | Sauter-mean |
| K_{agg} | aggregation coefficient |
| K_{cap} | capture coefficient |
| t | time (s) |
| z | special position (m) |

Subscripts and Superscripts

| | |
|-------|--------------------------|
| cap | capture term |
| d | droplet (disperse phase) |

Abbreviations

| | |
|-----------|--|
| $BS \& W$ | basic sediment and water (water content) |
|-----------|--|

Chapter 5 - Conclusions and Suggestions

5.1. Conclusions

The present work aimed to develop aggregation and capture kernels for the electrocoalescence process. The CFD-PBE was used as the principal idea to model/simulate the process. Moreover, a new concept named capture term was introduced to model the creation of the free water phase. For this objective, the project was basically divided into two stages:

1. Development of coalescence and capture kernels for the electrocoalescence process based on batch experiments
2. Simulation the continuous electrocoalescence pilot plant to evaluate the compatibility of the derived coalescence and capture kernels

First, a dynamic PBM based on mass/momentum/balance equations was developed to predict the behavior of batch electrocoalescence. The Eulerian multiphase model and QMOM population balance solution technique were coupled to construct the system of equations. In this work, the ComSol Multiphysics software (COMSOL Inc) was used to determine the distribution of electric field inside the electrostatic vessels. The parameters of the aggregation and capture kernels were estimated for the batch electrocoalescence experiments of non-saline and saline W/O emulsions. The results showed that the proposed model has a decent performance in predicting the behavior of batch electrocoalescence. The modeling displayed that at the beginning of the process, the aggregation between the droplets controls the separation of phases. While as the process continues, the capture of droplets by the free phase becomes the controlling phenomenon. Moreover, the calculations showed that the presences of both aggregation and capture terms are necessary to predict the process. Nevertheless, there were differences between the experimental and calculated values. The deviations were attributed to experimental and modeling errors. The conceptual shortcoming of the model was its incapability to predict the points where the volume fraction of the secondary phase passes the 90%. This is because the polydisperse assumption of the model in which the drag force increases extremely in the regions where the volume fraction of the secondary phase is high. This

is due to the limitation of the model that cannot switch between polydisperse Eulerian and VOF models in case certain criterion is reached.

Second, the continuous electrocoalescence pilot plant was simulated using the Ansys Fluent (R) software [96]. For this aim, the polydisperse Eulerian and QMOM population balance models of the Ansys Fluent (R) software [96] were utilized. Several UDFs were developed to implement the proposed model in the software. The objective was to evaluate the sensibility of simulations to the aggregation/capture parameters and DSD of initial W/O emulsion at the central experimental point of the work of Souza [169]. The results of simulations showed that unlike the batch model, the separation of phases does not increase by the increase of aggregation/capture coefficient and initial average diameter of droplets for all simulation cases. The contour of free phase volume fraction and d_{32} of water droplets exhibited that there exists an interaction between the momentum of untreated W/O emulsion and the formation of big water droplets that tries to overcome the drag force and descend. Moreover, the simulations showed that as the free water reaches the bottom of the vessel, continuous disordered bulks of free phase are created mainly in the regions close to the wall along the height of the vessel. This is the reason why the profile of water volume fraction and d_{32} of droplets at the outlet displayed oscillations. In this work, it was not possible to examine the trustfulness of the simulations as the experimental work of Souza [169] was not performed the same emulsions used in the batch experiments. However, the probable errors of the simulations are accredited to the assumptions/simplifications made to develop the proposed model.

5.2. Suggestions for Future Works

In order to perform a more realistic modeling/simulation of the electrocoalescence process, and obtain better aggregation/capture kernels, some enhancements in the proposed methodology should be considered. The suggestions are:

- Perform the batch experiments in a vessel with horizontal electrodes similar to the study of Khajehesamedini [173] that is closer to the industrial unit;
- Measure the water content at the very bottom and top of the batch vessel to determine the maximum amount of separation;
- Consider the use of improved techniques to measure the water content and droplet size distribution

- Perform 2D or 3D modeling/simulation of the batch electrostatic vessel to consider the radial gradients;
- Perform 3D ComSol simulations to have a better calculation of the electric field;
- Increase the current understanding of the influence of the electric field on the W/O emulsion and the electrocoalescence process;
- Execute 3D CFD to obtain more realistic simulations of the vessel;
- Consider the presence of the electrodes in the 2D/3D model;
- Evaluate the possibility of breakage of droplets during the electrocoalescence;
- Run the CFD simulations on the open-source OpenFOAM software ([OpenCFD Ltd., 2013](#)) to observe/follow the complete algorithms of the calculation;
- Develop an Eulerian-VOF model to represent the free phase which is capable of switching between the two, based on the volume fraction of the free water;
- Couple the calculation of AC electric field to the CFD-PBE calculations in CFD software using UDF;
- Implement the ζ_k -Wheeler algorithm [163] in the Ansys Fluent (R) software [96] using UDF to check the moments realizability.

Bibliography

- [1] H.. Bradley, Petroleum Engineering Handbook, Soc. Pet. Eng. U.S.A., Third Print. (1992) 634–720. http://petrowiki.org/PEH%3AElectrical_Submersible_Pumps.
- [2] Eaton P, US Patent No. 6086750, (2000).
- [3] F.C. Manning, R.E. Thompsom, Oilfield Processing, Crude Oil. Tulsa PennWell Books. 2 (1995) 5.
- [4] J.S. Eow, M. Ghadiri, A.O. Sharif, T.J. Williams, Electrostatic enhancement of coalescence of water droplets in oil: A review of the current understanding, Chem. Eng. J. 84 (2001) 173–192. doi:10.1016/S1385-8947(00)00386-7.
- [5] M. Stewart, E.A. Ken, Surface Production Operations : Design of Oil Handling Systems and Facilities, (2011) 747. doi:10.1017/CBO9781107415324.004.
- [6] G.W. Sams, K.W. Warren, New methods of application of electrostatic fields, Present. AIChE Spring Natl. Meet. Recent Adv. Desalt. News Orleans, Louisiana. (2004).
- [7] R. Varadaraj, C. Brons, Molecular Origins of Crude Oil Interfacial Activity Part 3 : Characterization of the Complex Fluid Rag Layer Formed at Crude Oil – Water Interfaces Molecular Origins of Crude Oil Interfacial Activity Part 3 : Characterization of the Complex Fluid Rag Laye, Energy. (2007) 1–6. doi:10.1021/ef0606299.
- [8] Dennis N. and Perugini J.J, US Patent No. 4992210, (1991).
- [9] E. Fetter Pruneda, E. Rivero, B. Escobedo, F. Javier, G. Vázquez, Optimum Temperature in the Electrostatic Desalting of Maya Crude Oil, Chem. Soc. 49 (2005) 14–19.
- [10] I.S. and B.G. Melheim J.A., Chiesa M., Forces between two water droplets in oil under the influence of an electrical field, Present. 5th Int. Conf. Multiph. Flow, Yokohama, Japan. (2004).
- [11] R. Draxler, J. and Marr, Design Criteria for Electrostatic Demulsifiers, Comput. Chem. Eng. Vol. 30. (1993).
- [12] K. W. Yu and T. K. W. Jones, Interparticle forces in polydisperse electrorheological fluids, Comput. Phys. Community, Vol. 129, Pp. 177–184. (2000).
- [13] J.S. Eow, M. Ghadiri, DropÁ drop coalescence in an electric field : the effects of applied electric field and electrode geometry, 219 (2003) 253–279. doi:10.1016/S0927-7757(03)00051-7.
- [14] P. Atten, Electrohydrodynamics of dispersed drops of conducting liquid: From drops deformation and interaction to emulsion evolution, Int. J. Plasma Environ. Sci. Technol. 7 (2013) 2–12.
- [15] M.T. Urdahl, O., Williams, T. J., Bailey, A. G., Thew, Electrostatic destabilization of water in-oil emulsions under conditions of turbulent flow, Trans. Inst. Chem. Eng. Vol. 74 (A), Pp. 158 – 165. (1996).

- [16] D.R. Burris, Dual Polarity oil dehydration, *Pet. Eng.* Pp. 30 – 41. (1997).
- [17] X. Xu, J. Yang, J. Gao, Effects of demulsifier structure on desalting efficiency of crude oils, *Pet. Sci. Technol.* 24 (2006) 673–688. doi:10.1081/LFT-200041172.
- [18] A. Byers, Charles H. and Amarnath, Understand the potential of electro-separations, *Chem. Eng. Progress*, Pp. 63-69. (1995).
- [19] M. Mohammadi, S. Shahhosseini, M. Bayat, Direct numerical simulation of water droplet coalescence in the oil, *Int. J. Heat Fluid Fl.* 36 (2012) 58–71.
- [20] K. Zeidani, A. Bahadori, New equations predicting the best performance of electrostatic desalter, *Pet. Sci. Technol.* 26 (2008) 40–49. doi:10.1080/10916460600705634.
- [21] K. Ivanitskii, Modeling of deformation and breakup of drops moving in liquid, *Heat Transf. Res.* 29(4 5), Pp. 225 – 234. (1998).
- [22] G.W. Bailes, Philip J., Freestone, D. and Sams, Pulsed DC Fields for Electrostatic Coalescence of Water-in-Oil Emulsions, *Chem. Eng.* 23 October, 34-39. (1997).
- [23] M. Al-Otaibi, A. Elkamel, T. Al-Sahhaf, A.S. Ahmed, Experimental investigation of crude oil desalting and dehydration, *Chem. Eng. Commun.* 190 (2003) 65–82. doi:10.1080/00986440302094.
- [24] M.B. Al-otaibi, A. Elkamel, V. Nassehi, S.A. Abdul-wahab, A Computational Intelligence Based Approach for the Analysis and Optimization of a Crude Oil Desalting and Dehydration Process, (2005).
- [25] R.P. Alves, R.C. Oliveira, How to establish a mathematical model for the electrostatic desalting process based on pilot plant studies, *SPE Annu. Tech. Conf. Exhib.* (2006) 1–5. doi:10.2523/102790-MS.
- [26] R. Lucas, Performance of Heavy Oil Dehydrators, *J. Pet. Technol.* 21 (1969) 1285–1292. doi:10.2118/2173-PA.
- [27] C.H.. Oliveira, R.C.G.; Figueiredo , A.M.P.; Carvalho, Tratamento eletrostático do petróleo blend de Marlim utilizando unidade-piloto, *Relatório Interno CENPES/PETROBRAS S.A.,.* (1995).
- [28] C.H.. Oliveira, R.C.G.; Figueiredo, A.M.P.; Carvalho, Tratamento eletrostático da mistura de petróleo Árabe-leve + RAT em unidade-piloto e comparação com os resultados obtidos na dessalgadora industrial, D-5106 Da REDUC. *Relatório Interno CENPES/PETROBRAS S.A.,.* (1996).
- [29] M.C.. Oliveira, R.C.G.; Oliveira, Levantamento do desempenho do processo de tratamento bielétrico de petróleos, *Relatório Interno CENPES/PETROBRAS S.A.* (2000).
- [30] P. Suemar, E.F. Fonseca, R.C. Coutinho, F. MacHado, R. Fontes, L.C. Ferreira, E.L. Lima, P.A. Melo, J.C. Pinto, M. Nele, Quantitative evaluation of the efficiency of water-in-crude-oil emulsion dehydration by electrocoalescence in pilot-plant and full-scale units, *Ind. Eng. Chem. Res.* 51 (2012) 13423–13437. doi:10.1021/ie202489g.
- [31] R.C.. Fonseca, E.F., Coutinho, Modelagem empírica do tratamento eletrostático de petróleo, *Relatório Interno CENPES/PETROBRAS S.A.* (2005).

- [32] C. Kiparissides, Challenges in particulate polymerization reactor modeling and optimization: A population balance perspective, *J. Process Control.* 16 (2006) 205–224. doi:10.1016/j.jprocont.2005.06.004.
- [33] Y. Peng, T. Liu, H. Gong, X. Zhang, Review of the Dynamics of Coalescence and Demulsification by High-Voltage Pulsed Electric Fields, *Int. J. Chem. Eng.* 2016 (2016). doi:10.1155/2016/2492453.
- [34] M. Chiesa, J.A. Melheim, A. Pedersen, S. Ingebrigtsen, G. Berg, Forces acting on water droplets falling in oil under the influence of an electric field: Numerical predictions versus experimental observations, *Eur. J. Mech. B/Fluids.* 24 (2005) 717–732. doi:10.1016/j.euromechflu.2005.03.005.
- [35] S. Mhatre, S. Deshmukh, R.M. Thaokar, Electrocoalescence of a drop pair, *Phys. Fluids.* 27 (2015). doi:10.1063/1.4931592.
- [36] G.K. Batchelor, *An Introduction to Fluid Dynamics*, Cambridge Univ. Press. New York. (2000) 615.
- [37] J. Hadamard, Mouvement permanent lent d'une sphere liquide et visqueuse dans un liquide visqueux, *C. R. Hebd. Seances Acad. Sci.* 275 (1911) 1735–1738. doi:nicht verfügbar?
- [38] B.S. Hamlin, W.D. Ristenpart, Transient reduction of the drag coefficient of charged droplets via the convective reversal of stagnant caps, *Phys. Fluids.* 24 (2012). doi:10.1063/1.3674301.
- [39] P. Parvasi, A. Khaje Hesamedini, A. Jahanmiri, M.R. Rahimpour, A Novel Modeling and Experimental Study of Crude Oil Desalting using Microwave, *Sep. Sci. Technol.* 49 (2014) 1029–1044. doi:10.1080/01496395.2013.871560.
- [40] E.W. Barega, E. Zondervan, A.B. de Haan, A combined lossy capacitor population balance model (LCPBM) for calculating the influence of frequency on electric field enhanced coalescence in a static-mixer settler setup, *Chem. Eng. Sci.* 104 (2013) 727–741. doi:10.1016/j.ces.2013.10.002.
- [41] J.A. Melheim, M. Chiesa, Simulation of turbulent electrocoalescence, *Chem. Eng. Sci.* 61 (2006) 4540–4549. doi:10.1016/j.ces.2006.02.022.
- [42] M. Chiesa, S. Ingebrigtsen, J.A. Melheim, P. V. Hemmingsen, E.B. Hansen, Hestad, Investigation of the role of viscosity on electrocoalescence of water droplets in oil, *Sep. Purif. Technol.* 50 (2006) 267–277. doi:10.1016/j.seppur.2005.12.003.
- [43] L. min He, D. hai Yang, R. na Gong, T. jie Ye, Y. ling Lü, X. ming Luo, An investigation into the deformation, movement and coalescence characteristics of water-in-oil droplets in an AC electric field, *Pet. Sci.* 10 (2013) 548–561. doi:10.1007/s12182-013-0306-1.
- [44] W.J. Howarth, Coalescence of drops in a turbulent flow field, *Chem. Eng. Sci.* 19 (1964) 33–38. doi:10.1016/0009-2509(64)85003-X.
- [45] Y. Liao, D. Lucas, A literature review on mechanisms and models for the coalescence process of fluid particles, *Chem. Eng. Sci.* 65 (2010) 2851–2864. doi:10.1016/j.ces.2010.02.020.

- [46] D. SCHUSTE, Encyclopedia of Emulsion Technology, Pharm. Unserer Zeit. 13 (1996) 59–60. doi:10.1002/pauz.19840130212.
- [47] K. Stewart, M. A. K., Arnold, Emulsions and oil treating equipment: selection, sizing and troubleshooting, Elsevier, Burlington, USA. (2009).
- [48] P. Ghosh, Coalescence of drops in liquid, Advances in Multiphase Flow and Heat Transfer, Vol. 3, Pp. 84-134. (2012).
- [49] J.. Shinnar, R., Church, Predicting particle size in agitated dispersions, Ind. Eng. Chem. Vol. 52, Pp. 253–256. (1960).
- [50] P. Ghosh, Colloid and interface science, PHI Learning Private Limited, New Delhi. (2009).
- [51] A. Vrij, J.T.H.G. Overbeek, Rupture of thin liquid films due to spontaneous fluctuations in thickness, J. Am. Chem. Soc. 90 (1968) 3074–3078. doi:10.1021/ja01014a015.
- [52] E.E. Isaacs, R.S. Chow, Practical Aspects of Emulsion Stability, Emuls. Fundam. Appl. Pet. Ind. (1992) 51–77. doi:10.1021/ba-1992-0231.ch002.
- [53] T. Frising, C. Noik, C. Dalmazzone, The liquid/liquid sedimentation process: From droplet coalescence to technologically enhanced water/oil emulsion gravity separators: A review, J. Dispers. Sci. Technol. 27 (2006) 1035–1057. doi:10.1080/01932690600767098.
- [54] J. Den Chen, Effects of London-van der Waals and electric double layer forces on the thinning of a dimpled film between a small drop or bubble and a horizontal solid plane, J. Colloid Interface Sci. 98 (1984) 329–341. doi:10.1016/0021-9797(84)90158-9.
- [55] T.G. Owe Berg, G.C. Fernish, T.A. Gaukler, The Mechanism of Coalescence of Liquid Drops, J. Atmos. Sci. 20 (1963) 153–158. doi:10.1175/1520-0469(1963)020<0153:TMOCOL>2.0.CO;2.
- [56] Galvin. C. P, Design principles for electrical coalescers, IChemE Symp. Ser. Vol. 88, Pp. 101–113. (1986) 21–30.
- [57] P. Atten, On electrocoalescence of water droplets in an insulating liquid, Conf. Rec. - IAS Annu. Meet. (IEEE Ind. Appl. Soc. 1992-Janua (1992) 1407–1411. doi:10.1109/IAS.1992.244253.
- [58] G.M. Panchenkov, V.M. Vinogradov, Water-in-oil emulsion in a constant homogeneous electric field, Chem. Technol. Fuels Oils. 6 (1970) 438–441. doi:10.1007/BF00718744.
- [59] G. Taylor, Disintegration of Water Drops in an Electric Field, Proc. R. Soc. A Math. Phys. Eng. Sci. 280 (1964) 383–397. doi:10.1098/rspa.1964.0151.
- [60] J. Latham, I.W. Roxburgh, Disintegration of Pairs of Water Drops in an Electric Field, Proc. R. Soc. A Math. Phys. Eng. Sci. 295 (1966) 84–97. doi:10.1098/rspa.1966.0227.
- [61] Brazier-Smith, Jennings, Latham, An investigation of the behaviour of drops and drop-pairs subjected to strong electrical forces, Proc. R. Soc. Lond. A. Math. Phys. Sci. (1971) 363–376. doi:10.1098/rspa.1971.0174.

- [62] J. Raisin, P. Atten, F. Aitken, J.L. Reboud, Electrically induced coalescence of two facing anchored water drops in oil, 2008 IEEE Int. Conf. Dielectr. Liq. ICDL 2008. (2008). doi:10.1109/ICDL.2008.4622467.
- [63] P. Atten, F. Aitken, Electrocoalescence criterion for two close anchored water drops and estimate for pairs of drops in a field, IEEE Trans. Ind. Appl. 46 (2010) 1578–1585. doi:10.1109/TIA.2010.2050984.
- [64] Waterman. L. C, Electrical coalescers, Chem. Eng. Prog. Vol. 61(10), Pp. 51–57. (1965).
- [65] P. Atten, Critical conditions for electrically induced coalescence of two very close water droplets in oil, 2005 IEEE Int. Conf. Dielectr. Liq. ICDL 2005. (2005).
- [66] P. Atten, L. Lundgaard, G. Berg, A simplified model of electrocoalescence of two close water droplets in oil, J. Electrostat. 64 (2006) 550–554. doi:10.1016/j.elstat.2005.10.009.
- [67] P.R. Brazier-Smith, Stability and Shape of Isolated and Pairs of Water Drops in an Electric Field, Phys. Fluids. 14 (1971) 1. doi:10.1063/1.1693258.
- [68] A. Ervik, S.M. Helleso, S.T. Munkejord, B. Muller, Experimental and computational studies of water drops falling through model oil with surfactant and subjected to an electric field, Proc. 2014 IEEE 18th Int. Conf. Liq. Dielectr. (2014) 1–6. doi:10.1109/ICDL.2014.6893172.
- [69] M. Mousavichoubeh, M. Ghadiri, M. Shariaty-Niassar, Electro-coalescence of an aqueous droplet at an oil-water interface, Chem. Eng. Process. Process Intensif. 50 (2011) 338–344. doi:10.1016/j.cep.2010.09.017.
- [70] K.E.T. Giljarhus, S.T. Munkejord, Numerical investigation of electrostatically enhanced coalescence of two drops in a flow field, Proc. - IEEE Int. Conf. Dielectr. Liq. (2011). doi:10.1109/ICDL.2011.6015441.
- [71] C.A.R. Pearce, The mechanism of the resolution of water-in-oil emulsions by electrical treatment, Br. J. Appl. Phys. 5 (1954) 136–143. doi:10.1088/0508-3443/5/4/304.
- [72] R.S. Allan, S.G. Mason, Particle motions in sheared suspensions. XIV. Coalescence of liquid drops in electric and shear fields, J. Colloid Sci. 17 (1962) 383–408. doi:10.1016/0095-8522(62)90016-8.
- [73] D. Sartor, A Laboratory Investigation of Collision Efficiencies, Coalescence and Electrical Charging of Simulated Cloud Droplets, J. Meteorol. 11 (1954) 91–103. doi:10.1175/1520-0469(1954)011<0091:ALIOCE>2.0.CO;2.
- [74] J.C. Bird, W.D. Ristenpart, A. Belmonte, H.A. Stone, Critical angle for electrically driven coalescence of two conical droplets, Phys. Rev. Lett. 103 (2009). doi:10.1103/PhysRevLett.103.164502.
- [75] P.S.M.. Cunha, Mathematical Modeling of the Crude Oil Electrostatic Dehydration Process, Univ. Fed. Do Rio Janeiro, EQ, RJ, Brazil [Master's thesis], [in Port. (2008).
- [76] M.M. Attarakih, H.J. Bart, N.M. Faqir, Numerical solution of the spatially distributed population balance equation describing the hydrodynamics of

- interacting liquid-liquid dispersions, *Chem. Eng. Sci.* 59 (2004) 2567–2592. doi:10.1016/j.ces.2004.03.005.
- [77] I.R. Sweet, S.S. Gustafson, D. Ramkrishna, Population balance modelling of bubbling fluidized bed reactors-I. well-stirred dense phase, *Chem. Eng. Sci.* 42 (1987). doi:10.1016/0009-2509(87)85064-9.
- [78] N.K. Nere, D. Ramkrishna, Solution of population balance equation with pure aggregation in a fully developed turbulent pipe flow, *Chem. Eng. Sci.* 61 (2006) 96–103. doi:10.1016/j.ces.2004.12.054.
- [79] H.S. Song, D. Ramkrishna, S. Trinh, R.L. Espinoza, H. Wright, Multiplicity and sensitivity analysis of Fischer - Tropsch bubble column slurry reactors: Plug-flow gas and well-mixed slurry model, *Chem. Eng. Sci.* 58 (2003) 2759–2766. doi:10.1016/S0009-2509(03)00125-8.
- [80] E. Sherer, R.E. Hannemann, A.E. Rundell, D. Ramkrishna, Application of stochastic equations of population balances to sterilization processes, *Chem. Eng. Sci.* 64 (2009) 764–774. doi:10.1016/j.ces.2008.05.011.
- [81] C. Borchert, N. Nere, D. Ramkrishna, A. Voigt, K. Sundmacher, On the prediction of crystal shape distributions in a steady-state continuous crystallizer, *Chem. Eng. Sci.* 64 (2009) 686–696. doi:10.1016/j.ces.2008.05.009.
- [82] D. Ramkrishna, *Population Balances: Theory and Applications to Particulate Systems in Engineering*, Acad. Press. New York. (2000).
- [83] J.R. Rogers, Rober H., The effects of van der Waals attractions on cloud droplet growth by coalescence, *Am. Meteorol. Soc.* (1990). doi:10.1175/1520-0469(1990)047<1075:TEOVDW>2.0.CO;2.
- [84] X. Zhang, O.A. Basaran, R.M. Wham, Theoretical prediction of electric field-enhanced coalescence of spherical drops, *AIChE J.* 41 (1995) 1629–1639. doi:10.1002/aic.690410704.
- [85] H.A. Stone, Collective Hydrodynamics of Deformable Drops and Bubbles in Dilute Low Reynolds Number Suspensions, *J. Fluid Mech.* 300 (1995) 231–263. doi:10.1017/S0022112095003673.
- [86] G. Narsimhan, Model for drop coalescence in a locally isotropic turbulent flow field, *J. Colloid Interface Sci.* 272 (2004) 197–209. doi:10.1016/j.jcis.2003.11.057.
- [87] S. Lo, P. Rao, Modelling of droplet breakup and coalescence in an oil-water pipeline, 6th Int. Conf. Multiph. Flow, ICMF (2007) 1–7. <http://cdaes.com/sites/default/files/Presentation/2007-ICMF.pdf>.
- [88] V. Meidanshahi, A. Jahanmiri, M.R. Rahimpour, Modeling and Optimization of Two Stage AC Electrostatic Desalter, *Sep. Sci. Technol.* 47 (2012) 30–42. doi:10.1080/01496395.2011.614316.
- [89] J.F. Mitre, P.L.C. Lage, M.A. Souza, E. Silva, L.F. Barca, A.O.S. Moraes, R.C.C. Coutinho, E.F. Fonseca, Droplet breakage and coalescence models for the flow of water-in-oil emulsions through a valve-like element, *Chem. Eng. Res. Des.* 92 (2014) 2493–2508. doi:10.1016/j.cherd.2014.03.020.
- [90] M. von Smoluchowski, Drei Vorträge über Diffusion, Brownsche

- Molekularbewegung und Koagulation von Kolloidteilchen, *Phys. Z.* 17 (1916) 585.
- [91] V. Meidanshahi, A. Jahanmiri, M.R. Rahimpour, Modeling and Optimization of Two Stage AC Electrostatic Desalter, *Sep. Sci. Technol.* 47 (2012) 30–42. doi:10.1080/01496395.2011.614316.
- [92] E. Aryafard, M. Farsi, M.R. Rahimpour, Modeling and simulation of crude oil desalting in an industrial plant considering mixing valve and electrostatic drum, *Chem. Eng. Process. Process Intensif.* 95 (2015) 383–389. doi:10.1016/j.cep.2015.06.011.
- [93] E. Aryafard, M. Farsi, M.R. Rahimpour, S. Raeissi, Modeling electrostatic separation for dehydration and desalination of crude oil in an industrial two-stage desalting plant, *J. Taiwan Inst. Chem. Eng.* 58 (2016) 141–147. doi:10.1016/j.jtice.2015.06.028.
- [94] C.T. Crowe, *Multiphase Flow Handbook*, CRC Press. 1218 (2006) 1156. doi:10.1016/j.chroma.2011.01.063.
- [95] V. V Ranade, *Computational flow modeling for chemical reactor engineering*, Acad. Press. New York. (2001). <http://books.google.com/books?id=kJcJporv8pQC%5Cnpapers2://publication/uuid/8EEDD678-A223-4D5C-9D65-AB755A6877CE>.
- [96] I. ANSYS, *Ansys Fluent 17.2 Theory Guide*, (2016).
- [97] A. Buffo, D.L. Marchisio, M. Vanni, P. Renze, Simulation of polydisperse multiphase systems using population balances and example application to bubbly flows, *Chem. Eng. Res. Des.* 91 (2013) 1859–1875. doi:10.1016/j.cherd.2013.06.021.
- [98] P.S. Drew Da, *Theory of multicomponent fluids*, 1st Ed. New York Springer. (1998).
- [99] M. Ishii, T. Hibiki, Thermo-fluid dynamics of two-phase flow, *Thermo-Fluid Dyn. Two-Phase Flow.* (2006) 1–462. doi:10.1007/978-0-387-29187-1.
- [100] C.T. Crowe, M. Sommerfeld, Y. Tsuji, *Multiphase Flows with Droplets and Particles*, CRC Press New York. (1998) 191–222. doi:10.1201/b11103-4.
- [101] A. Sokolichin, G. Eigenberger, Gas-liquid flow in bubble columns and loop reactors: Part I. Detailed modelling and numerical simulation, *Chem. Eng. Sci.* 49 (1994) 5735–5746. doi:10.1016/0009-2509(94)00289-4.
- [102] H.A. Jakobsen, B.H. Sannæs, S. Grevskott, H.F. Svendsen, Modeling of Vertical Bubble-Driven Flows, *Ind. Eng. Chem. Res.* 36 (1997) 4052–4074. doi:10.1021/ie970276o.
- [103] D. Pflieger, S. Gomes, N. Gilbert, H.G. Wagner, Hydrodynamic simulations of laboratory scale bubble columns fundamental studies of the Eulerian-Eulerian modelling approach, *Chem. Eng. Sci.* 54 (1999) 5091–5099. doi:10.1016/S0009-2509(99)00261-4.
- [104] V. V Buwa, V. V Ranade, Dynamics of gas-liquid flow in a rectangular bubble column: experiments and single/multi-group CFD simulations, *Chem. Eng. Sci.* 57

(2002) 4715–4736.

- [105] B.H. Hjertager, Multi-fluid CFD analysis of chemical reactors, *Multiph. React. Flows Model. Simul.* (2007) 125–179.
- [106] P. Chen, J. Sanyal, M.P. Duduković, Numerical simulation of bubble columns flows: Effect of different breakup and coalescence closures, *Chem. Eng. Sci.* 60 (2005) 1085–1101. doi:10.1016/j.ces.2004.09.070.
- [107] A. Zucca, D.L. Marchisio, A.A. Barresi, R.O. Fox, Implementation of the population balance equation in CFD codes for modelling soot formation in turbulent flames, *Chem. Eng. Sci.* 61 (2006) 87–95. doi:10.1016/j.ces.2004.11.061.
- [108] L.F.L.R. Silva, R.B. Damian, P.L.C. Lage, Implementation and analysis of numerical solution of the population balance equation in CFD packages, *Comput. Chem. Eng.* 32 (2008) 2933–2945. doi:10.1016/j.compchemeng.2008.03.007.
- [109] M. Petitti, A. Nasuti, D.L. Marchisio, M. Vanni, G. Baldi, N. Mancini, F. Podenzani, Bubble size distribution modeling in stirred gas-liquid reactors with QMOM augmented by a new correction algorithm, *AIChE J.* 56 (2010) 36–53. doi:10.1002/aic.12003.
- [110] M. Petitti, M. Vanni, D.L. Marchisio, A. Buffo, F. Podenzani, Simulation of coalescence, break-up and mass transfer in a gas-liquid stirred tank with CQMOM, *Chem. Eng. J.* 228 (2013) 1182–1194. doi:10.1016/j.cej.2013.05.047.
- [111] A. Passalacqua, R.O. Fox, R. Garg, S. Subramaniam, A fully coupled quadrature-based moment method for dilute to moderately dilute fluid-particle flows, *Chem. Eng. Sci.* 65 (2010) 2267–2283. doi:10.1016/j.ces.2009.09.002.
- [112] L.F.L.R. Silva, P.L.C. Lage, Development and implementation of a polydispersed multiphase flow model in OpenFOAM, *Comput. Chem. Eng.* 35 (2011) 2653–2666. doi:10.1016/j.compchemeng.2011.04.011.
- [113] W.C. Yan, Z.H. Luo, A.Y. Guo, Coupling of CFD with PBM for a pilot-plant tubular loop polymerization reactor, *Chem. Eng. Sci.* 66 (2011) 5148–5163. doi:10.1016/j.ces.2011.07.004.
- [114] A. Buffo, M. Vanni, D.L. Marchisio, Multidimensional population balance model for the simulation of turbulent gas-liquid systems in stirred tank reactors, *Chem. Eng. Sci.* In Press, (2011). doi:10.1016/j.ces.2011.04.042.
- [115] J.C. Lasheras, C. Eastwood, C. Martínez-Bazán, J.L. Montañés, A review of statistical models for the break-up of an immiscible fluid immersed into a fully-developed turbulent flow, *Int. J. Multiph. Flows.* 28 (2002) 247–278.
- [116] Mitre JF, Modelos de Quebra e Coalescência de Gotas para o Escoamento de Emulsões, "[PhD Thesis]. Programa Eng. Química, COPPE/UFRJ; [in Port. (2010).
- [117] D. Meimaroglou, C. Kiparissides, Monte Carlo simulation for the solution of the bi-variate dynamic population balance equation in batch particulate systems, *Chem. Eng. Sci.* 62 (2007) 5295–5299. doi:10.1016/j.ces.2006.11.032.
- [118] R. Irizarry, Fast Monte Carlo methodology for multivariate particulate systems-II:

- τ -PEMC, *Chem. Eng. Sci.* 63 (2008) 111–121. doi:10.1016/j.ces.2007.09.006.
- [119] G. Subramanian, D. Ramkrishna, On the solution of statistical models of cell populations, *Math. Biosci.* 10 (1971) 1–23. doi:10.1016/0025-5564(71)90050-2.
- [120] H.M. Hulburt, T. Akiyama, Liouville equations for agglomeration and dispersion processes, *Ind. Eng. Chem. Fundam.* 8 (1969) 319–324. doi:10.1021/i160030a022.
- [121] C.A. Dorao, H.A. Jakobsen, A least squares method for the solution of population balance problems, 30 (2006) 535–547. doi:10.1016/j.compchemeng.2005.10.012.
- [122] J. Solsvik, H.A. Jakobsen, Evaluation of weighted residual methods for the solution of a population balance model describing bubbly flows: The least-squares, Galerkin, tau, and orthogonal collocation methods, *Ind. Eng. Chem. Res.* 52 (2013) 15988–16013. doi:10.1021/ie402033b.
- [123] J.D. Lister, D.J. Smit, M.J. Hounslow, Adjustable discretized population balance for growth and aggregation, *AIChE J.* 41 (1995) 591–603. doi:10.1002/aic.690410317.
- [124] S. Kumar, D. Ramkrishna, On the solution of population balance equations by discretization—I. A fixed pivot technique, *Chem. Eng. Sci.* 51 (1996) 1311–1332. doi:10.1016/0009-2509(96)88489-2.
- [125] T. Blacha, M. Di Domenico, P. Gerlinger, M. Aigner, Soot predictions in premixed and non-premixed laminar flames using a sectional approach for PAHs and soot, *Combust. Flame.* 159 (2012) 181–193. doi:10.1016/j.combustflame.2011.07.006.
- [126] A. Cuoci, T. Faravelli, S. Ferrario, C. Saggese, J. Camacho, A. Frassoldati, E. Ranzi, H. Wang, Kinetic modeling of particle size distribution of soot in a premixed burner-stabilized stagnation ethylene flame, *Combust. Flame.* 162 (2015) 3356–3369. doi:10.1016/j.combustflame.2015.06.002.
- [127] S.B. Dworkin, Q. Zhang, M.J. Thomson, N.A. Slavinskaya, U. Riedel, Application of an enhanced PAH growth model to soot formation in a laminar coflow ethylene/air diffusion flame, *Combust. Flame.* 158 (2011) 1682–1695. doi:10.1016/j.combustflame.2011.01.013.
- [128] R. McGraw, Description of aerosol dynamics by the quadrature method of moments, *Aerosol Sci. Technol.* 27 (1997) 255–265. doi:10.1080/02786829708965471.
- [129] D.L. Marchisio, R.O. Fox, Solution of Population Balance Equations using the Direct Quadrature Method of Moments, *Aerosol Sci. Technol.* 36 (2005) 43–73.
- [130] J.L. Favero, P.L.C. Lage, The dual-quadrature method of generalized moments using automatic integration packages, *Comput. Chem. Eng.* 38 (2012) 1–10. doi:10.1016/j.compchemeng.2011.11.010.
- [131] Y. Lin, P. Skjetne, A. Carlson, A phase field model for multiphase electrohydrodynamic flow, *Int. J. Multiph. Flow.* 45 (2012) 1–11. doi:10.1016/j.ijmultiphaseflow.2012.04.002.
- [132] T. Wang, J. Wang, Y. Jin, A CFD-PBM coupled model for gas-liquid flows, *AIChE J.* 52 (2006) 125–140. doi:10.1002/aic.10611.
- [133] H.M. Hulburt, S. Katz, Some problems in particle technology. A statistical

- mechanical formulation, *Chem. Eng. Sci.* 19 (1964) 555–574. doi:10.1016/0009-2509(64)85047-8.
- [134] D. L. Marchisio, R. Dennis Vigil, R. O. Fox, Implementation of the quadrature method of moments in CFD codes for aggregation–breakage problems, *Chem. Eng. Sci.* 58 (2003) 3337–3351. doi:10.1016/S0009-2509(03)00211-2.
- [135] B. Selma, R. Bannari, P. Proulx, Simulation of bubbly flows: Comparison between direct quadrature method of moments (DQMOM) and method of classes (CM), *Chem. Eng. Sci.* 65 (2010) 1925–1941. doi:10.1016/j.ces.2009.11.018.
- [136] C. Yuan, R.O. Fox, Conditional Quadrature Method of Moments for Kinetic Equations, *JComp.* (2010) 1–42. papers2://publication/uuid/C97D9988-3D7F-45D2-BB81-75355926FB88.
- [137] J.C. Cheng, R.O. Fox, Kinetic modeling of nanoprecipitation using CFD coupled with a population balance, *Ind. Eng. Chem. Res.* 49 (2010) 10651–10662. doi:10.1021/ie100558n.
- [138] C. Chalons, R.O. Fox, M. Massot, A multi-Gaussian quadrature method of moments for gas-particle flows in a LES framework, *Proc. Summer Progr. 2010 - Cent. Turbul. Res.* (2010) 347–358. http://www.stanford.edu/group/ctr/Summer/SP10/6_05_chalons.pdf papers2://publication/uuid/D6D22AA5-5982-475F-98B8-1AD6F16265F1.
- [139] W.N. Richardson, J. F.; Zaki, Sedimentation and Fluidization: Part 1, *Trans. Inst. Chem. Eng. Vol. 32*, Pp. 35-53. (1954).
- [140] W.J. Souza, K.M.C. Santos, A.A. Cruz, E. Franceschi, C. Dariva, A.F. Santos, C.C. Santana, Effect of Water Content, Temperature and Average Droplet Size on the Settling Velocity of Water-in-Oil Emulsions, *Brazilian J. Chem. Eng.* 32 (2015) 455–464.
- [141] R. Miller, L. Liggieri, Bubble and Drop Interfaces (Progress in Colloid and Interface Science), (2011). <http://www.amazon.com/Interfaces-Progress-Colloid-Interface-Science/dp/9004174958%3FSubscriptionId%3D0JYN1NVW651KCA56C102%26tag%3Dtechie-20%26linkCode%3Dxm2%26camp%3D2025%26creative%3D165953%26creativeASIN%3D9004174958>.
- [142] S. Mhatre, V. Vivacqua, M. Ghadiri, A.M. Abdullah, M.J. Al-Marri, A. Hassanpour, B. Hewakandamby, B. Azzopardi, B. Kermani, Electrostatic phase separation: A review, *Chem. Eng. Res. Des.* 96 (2015) 177–195. doi:10.1016/j.cherd.2015.02.012.
- [143] V. Meidanshahi, Modeling of Electrocoalescence in Electrostatic Desalter, M.Sc. Thesis, Univ. Shiraz, Iran. (2011).
- [144] R. Raghavan, S.S. Marsden, Theoretical Aspects of Emulsification in Porous Media, *Soc. Pet. Eng. J.* 11 (1971) 153–161. doi:10.2118/3089-PA.
- [145] A.. Paiva, Estudo da minimização de erro das medições de concentração de emulsões por titração Karl–Fisher utilizando-se projetos de experimentos, Univ. Fed. Itajubá, RJ, Brazil [Master’sthesis], [in Port. (2004).

- [146] J. Eow, M. Ghadiri, a Sharif, Electrostatic and hydrodynamic separation of aqueous drops in a flowing viscous oil, *Chem. Eng. Process.* 41 (2002) 649–657. doi:10.1016/S0255-2701(01)00183-0.
- [147] R.E.P. Cunha, M. Fortuny, C. Dariva, A.F. Santos, Mathematical Modeling of the Destabilization of Crude Oil Emulsions Using Population Balance Equation, *Ind. Eng. Chem. Res.* 47 (2008) 7094–7103. doi:10.1021/ie800391v.
- [148] C. Noik, C., Jiaqing, C., Dalmazzone, Electrostatic Demulsification on Crude Oil: A State-of-the-art Review. In: *International Oil and Gas Conference and Exhibition*, Vol.1, 5-7 December, Beijing, China, Pp. 410–421. (2006).
- [149] J. Bibette, D.C. Morse, T.A. Witten, D.A. Weitz, Stability criteria for emulsions, *Phys. Rev. Lett.* 69 (1992) 2439–2442. doi:10.1103/PhysRevLett.69.2439.
- [150] T.F. Tadros, *Emulsion Formation and Stability*, *Emuls. Form. Stab.* (2013). doi:10.1002/9783527647941.
- [151] J.L. Favero, L. Fernando, L.R. Silva, P.L.C. Lage, Modeling and simulation of mixing in water-in-oil emulsion flow through a valve-like element using a population balance model, *Comput. Chem. Eng.* 75 (2013) 155–170. doi:10.1016/j.compchemeng.2015.01.017.
- [152] L. Schiller, Z. Naumann, A drag coefficient correlation, *Z.Ver.Deutsch.Ing.* 77 (1933) 318–320. doi:10.1016/j.ijheatmasstransfer.2009.02.006.
- [153] A. Behzadi, R.I. Issa, H. Rusche, Modelling of dispersed bubble and droplet flow at high phase fractions, *Chem. Eng. Sci.* 59 (2004) 759–770. doi:10.1016/j.ces.2003.11.018.
- [154] M. Holger, *Towards the Numerical Simulation of Multi-Scale Two-Phase Flows*, PhD Thesis, Dept. Chem. Eng. Tech. Univ. München. (2011) 322. <https://mediatum.ub.tum.de/doc/1080878/1080878.pdf>.
- [155] P. Bécher, *Emulsion theory and practice*, Reinhold Publ. Corp. New-York. (1961). NON.
- [156] D. Ramkrishna, *Population balances: Theory and applications to particulate systems in engineering*, Acad. Press. New York. (2000).
- [157] W. Rybczynski, *Über die fortschreitende Bewegung einer flüssigen Kugel in einem zähen Medium*, *Bull. Int. l'Academie Des Sci. Cracovie Ser. A.* 1 (1911) 40–46.
- [158] M. Hazewinkel, *Encyclopedia of Mathematics*, 2 (2001) 1–1290.
- [159] S. Kumar, D. Ramkrishna, On the solution of population balance equations by discretization - I. A fixed pivot technique, *Chem. Eng. Sci.* 51 (1996) 1311–1332. doi:10.1016/0009-2509(96)88489-2.
- [160] D.L. Marchisio, J.T. Pikturna, R.O. Fox, R.D. Vigil, A.A. Barresi, Quadrature method of moments for population-balance equations, *AIChE J.* 49 (2003) 1266–1276. doi:10.1002/aic.690490517.
- [161] D.L. Marchisio, R.O. Fox, *Computational Models for Polydisperse Particulate and Multiphase Systems*, *Comput. Model. Polydisperse Part. Multiph. Syst.* (2013). doi:10.1017/cbo9781139016599.

- [162] D.L. Marchisio, R.O. Fox, Solution of population balance equations using the direct quadrature method of moments, *Aerosol Sci.* 36 (2005) 43–73.
- [163] A. Passalacqua, F. Laurent, E. Madadi-Kandjani, J.C. Heylmun, R.O. Fox, An open-source quadrature-based population balance solver for OpenFOAM, *Chem. Eng. Sci.* 176 (2018) 306–318. doi:10.1016/j.ces.2017.10.043.
- [164] T.T. Nguyen, F. Laurent, R.O. Fox, M. Massot, Solution of population balance equations in applications with fine particles: Mathematical modeling and numerical schemes, *J. Comput. Phys.* 325 (2016) 129–156. doi:10.1016/j.jcp.2016.08.017.
- [165] A.L. Rukhin, H. Dette, W.J. Studden, The Theory of Canonical Moments with Applications in Statistics, Probability and Analysis, *J. Am. Stat. Assoc.* 93 (2006) 1525. doi:10.2307/2670071.
- [166] J.C. Wheeler, Modified moments and Gaussian quadratures, *Rocky Mt. J. Math.* 4 (2009) 287–296. doi:10.1216/rmj-1974-4-2-287.
- [167] A.R. Secchi, Differential-Algebraic System Solver in C, [Http://Www.Enq.Ufrgs.Br/Enqlib/Numeric/](http://www.Enq.Ufrgs.Br/Enqlib/Numeric/) (Accessed May 2018). (2012).
- [168] A.O.S. Moraes, J.F. Mitre, P.L.C. Lage, A.R. Secchi, A robust parallel algorithm of the particle swarm optimization method for large dimensional engineering problems, *Appl. Math. Model.* 39 (2014) 4223–4241. doi:10.1016/j.apm.2014.12.034.
- [169] T. Assenheimer, A. Barros, K. Kashefi, J.C. Pinto, F.W. Tavares, M. Nele, Evaluation of Microwave and Conventional Heating for Electrostatic Treatment of a Water-in-Oil Model Emulsion in a Pilot Plant, *Energy and Fuels.* 31 (2017) 6587–6597. doi:10.1021/acs.energyfuels.7b00275.
- [170] T.A. De Souza, Avaliação Da Estabilidade De Emulsões Sob Campo Elétrico Utilizando Microscopia E Planta Piloto, [PhD Thesis]. Esc. Química/UFRJ; [in Port. (2018).
- [171] I. ANSYS, ANSYS Fluent Population Balance Module Manual, (2016).
- [172] X. Xinru, Y. Jingyi, J. Ying, G. Jinsheng, Effects of process conditions on desalting and demetalization of crude oil, *Pet. Sci. Technol.* 24 (2006) 1307–1321. doi:10.1081/LFT-200056651.
- [173] A. Khajehesamedini, A. Sadatshojaie, P. Parvasi, M. Reza Rahimpour, M. Mehdi Naserimojarad, Experimental and theoretical study of crude oil pretreatment using low-frequency ultrasonic waves, *Ultrason. Sonochem.* (2018). doi:10.1016/j.ultsonch.2018.05.032.